

A Near-infrared Variability Survey of Young Planetary-mass Objects

Pengyu Liu,^{1,2,3*} Beth A. Biller,^{1,2} Johanna M. Vos,^{4,5} Niall Whiteford,⁵ Zhoujian Zhang,^{6,†} Michael C. Liu,⁷ Clémence Fontanive,^{8,9} Elena Manjavacas,^{10,11} Thomas Henning,¹² Matthew A. Kenworthy,³ Mariangela Bonavita,^{1,2} Mickaël Bonnefoy,¹³ Emma Bubb,^{1,2} Simon Petrus,^{13,14} and Joshua Schlieder¹⁵

¹*Institute for Astronomy, University of Edinburgh, Royal Observatory, Edinburgh EH9 3HJ, UK*

²*Centre for Exoplanet Science, University of Edinburgh, Edinburgh, UK*

³*Leiden Observatory, Leiden University, PO Box 9513, 2300 RA Leiden, The Netherlands*

⁴*School of Physics, Trinity College Dublin, The University of Dublin, Dublin 2, Ireland*

⁵*Department of Astrophysics, American Museum of Natural History, New York, NY 10024, USA*

⁶*Department of Astronomy & Astrophysics, University of California, Santa Cruz, CA 95064, USA*

⁷*Institute for Astronomy, University of Hawaii at Manoa, Honolulu, HI 96822, USA*

⁸*Département de Physique and Observatoire du Mont-Mégantic, Université de Montréal, C.P. 6128, Succ. Centre-ville, Montréal, H3C 3J7, Québec, Canada*

⁹*Institut Troitier de Recherche sur les exoplanètes, Université de Montréal, Québec, Canada*

¹⁰*AURA for the European Space Agency (ESA), ESA Office, Space Telescope Science Institute, 3700 San Martin Drive, Baltimore, MD 21218 USA*

¹¹*Department of Physics and Astronomy, Johns Hopkins University, Baltimore, MD 21218, USA*

¹²*Max-Planck-Institut für Astronomie, Königstuhl 17, 69117 Heidelberg, Germany*

¹³*Université Grenoble Alpes, CNRS, IPAG, 38000 Grenoble, France*

¹⁴*Núcleo Milenio Formación Planetaria–NPF, Universidad de Valparaíso, Av. Gran Bretaña 1111, Valparaíso, Chile*

¹⁵*Exoplanets and Stellar Astrophysics Laboratory, Code 667, NASA Goddard Space Flight Center, Greenbelt, MD, USA*

Accepted XXX. Received YYY; in original form ZZZ

ABSTRACT

We present a photometric variability survey of young planetary-mass objects using the New Technology Telescope in the J_S and K_S bands. Surface gravity plays an important role in the atmospheric structure of brown dwarfs, as young low gravity L dwarfs have a higher variability rate than field L dwarfs. In this study, we extend variability studies to young T-type planetary-mass objects and investigate the effects of surface gravity on the variability of L and T dwarfs across a large sample. We conduct continuous monitoring for 18 objects with spectral types from L5 to T8 and detect four new variables and two variable candidates. Combining with previous variability surveys of field and young L and T objects, we find that young objects tend to be more variable than field objects within peak-to-peak variability amplitude ranges of 0.5%–10% and period ranges of 1.5–20 hr. For the first time, we constrain the variability rate of young T dwarfs to be 56^{+20}_{-18} % compared to 25^{+8}_{-7} % for field T dwarfs. Both field and young samples have higher variability rates at the L/T transition than outside the L/T transition. The differences in the variability rates between field and young samples are about 1σ and therefore larger sample sizes are needed to confirm and refine the results. Besides the L/T transition, young L dwarfs with strong variability tend to assemble in a narrow spectral type range of L6–L7.5. This work supports the critical role of surface gravity on the atmospheric structure from L to T spectral types.

Key words: brown dwarfs – stars: atmospheres – stars: variables: general

1 INTRODUCTION

The first direct imaging and spectroscopy observations of planetary mass objects outside of the solar system can be dated back more than 20 years ago (Oasa et al. 1999; Lucas & Roche 2000; Zapatero Osorio et al. 2000; Lucas et al. 2001). These objects were discovered in nearby star-forming regions and are the first of a large population of free-floating exoplanets which are now discovered in young stellar associations such as Upper Scorpius and Ophiuchus (Miret-Roig et al. 2022; Bouy et al. 2022). In recent years, dozens of young brown dwarfs with planetary mass have been discovered by spectroscopy or kinematic characterisation in the field or nearby young moving

groups (e.g. Liu et al. 2013; Allers & Liu 2013; Gagné et al. 2015, 2017a, 2018; Liu et al. 2016; Faherty et al. 2016; Schneider et al. 2016, 2017; Zhang et al. 2021). These objects share similar properties with directly-imaged exoplanets, including mass, surface gravity, effective temperature, and spectral type. The study of these ultracool planetary-mass objects provides a unique opportunity to understand the atmospheres of giant exoplanets, as observations of giant exoplanets are often hindered by the brightness of the central stars. In contrast, young planetary-mass brown dwarfs are free-floating analogues to giant exoplanets. This makes them ideal targets for atmospheric characterization of planetary-mass objects, which opens a window to understand the atmospheres of giant exoplanets.

* E-mail: pengyu.liu@ed.ac.uk

† NASA Sagan Fellow

Without a sustainable heat source, brown dwarfs cool as they age. L dwarfs have an effective temperature from ~ 2500 to ~ 1300

K, while T dwarfs have an effective temperature from ~ 1300 to ~ 400 K (Kirkpatrick 2005). As their temperature decreases, their atmospheres undergo drastic changes. From early-L to late-L spectral types, they become fainter and redder in the near-infrared Kirkpatrick (2005). However, from late-L to mid-T spectral types, their near-infrared magnitudes span in a small range, indicating an almost constant effective temperature ($\sim 1400 \pm 200$ K), but their $J - K$ colours dramatically turn blue by ~ 2 mag (Kirkpatrick 2005). This phenomenon is known as the L/T transition (Golimowski et al. 2004; Stephens et al. 2009). Beyond mid-T spectral types, they continue becoming fainter. The prevailing explanation for the change in magnitude and colour at the L/T transition is that refractory materials, such as silicate and iron compounds, condense in the atmosphere of L dwarfs when their effective temperature falls below ~ 2300 K (Tsuji et al. 1996; Lodders 1999; Burrows et al. 2006). This leads to increased opacity due to dust and clouds. When the temperature falls below ~ 1300 K, the cloud grains and particles dissipate, resulting in a clear atmosphere in T dwarfs and a shift towards bluer colours at the L/T transition (Burrows & Sharp 1999; Tsuji & Nakajima 2003; Knapp et al. 2004; Cushing et al. 2008; Marley et al. 2010).

As brown dwarfs rotate, inhomogeneous atmospheric structures may cause variability in their light curves. Brown dwarfs are usually fast-rotators with periods varying from 1–2 h to 1–2 d (e.g. Zapatero Osorio et al. 2004; Metchev et al. 2015; Scholz et al. 2018; Moore et al. 2019). Numerous observations have been conducted to search for atmospheric variability in field L and T brown dwarfs. The first continuous monitoring survey, by Koen et al. (2004), detects low-level variability of less than 0.02 mag in 18 L and T dwarfs observed simultaneously in the JHK_S bands. A similar result is reported in their follow-up survey of ultracool dwarfs, with the exception of one T dwarf which shows a variability of 0.03 mag (Koen et al. 2005). A large survey of L4–T9 dwarfs in the J -band by Radigan et al. (2014) detects variability in 9 out of 57 dwarfs with over 99% confidence. The strongest signals, with peak-to-peak amplitudes over 2%, are all detected at the L/T transition (L9–T3.5), indicating that variability is most common among L/T transition brown dwarfs. Combining two large surveys by Radigan et al. (2014) and Wilson et al. (2014), Radigan (2014) report the observed frequency of strong variability is 24% at the L/T transition compared with 3.2% outside the L/T transition. These results support the theory that inhomogeneous atmospheric structures such as patchy clouds at the L/T transition are the driving sources of the observed variability.

Brown dwarfs contract as they age, and thus low surface gravity is often associated with young brown dwarfs. Surface gravity plays an important role in shaping the atmospheric structures of brown dwarfs, such as affecting dust particle size and non-equilibrium chemistry (Barman et al. 2011a,b; Marley et al. 2012). Morley et al. (2014) raise a possible link between low surface gravity and variability as planetary-mass objects tend to have thicker clouds than high-mass brown dwarfs. Metchev et al. (2015) present a variability survey of 44 L3–L8 dwarfs with the *Spitzer Space Telescope* and confirm that variability is common in L and T dwarfs with 80% of L dwarfs varying more than 0.2% and 36% of T dwarfs varying more than 0.4% in the mid-infrared. They suggest a tentative association between low surface gravity and strong variability based on six L3–L5.5 dwarfs with low gravity. Vos et al. (2019) report the first variability survey of 30 young and low-gravity L dwarfs in the J_S band and find a variability occurrence rate of 30% for low-gravity L0–L8.5 dwarfs, significantly higher than the 11% variability occurrence rate of the field L0–L8.5 dwarfs reported in Radigan et al. (2014); Radigan (2014). Vos et al. (2022) also find higher maximum variability amplitudes in young objects than field dwarfs in *Spitzer* data.

Several young low-surface gravity objects with strong variability have been discovered in recent years. For instance, PSO318.5-22 (Biller et al. 2015; Vos et al. 2019), VHS1256-1257b (Zhou et al. 2020), WISEP J004701.06+680352.1 (Lew et al. 2016), and 2MASS J2244316+204343 (Vos et al. 2019) are detected with peak-to-peak amplitudes $> 5\%$ in the near-infrared, which are young L6–L7.5 objects. Additionally, two strong variable T dwarfs, SIMP J013656.5+093347 (T2.5) and 2MASS J21392676+0220226 (T1.5), were initially classified as field dwarfs but were later confirmed as planetary-mass objects of the 200-Myr-old Carina-Near moving group (Gagné et al. 2017b; Zhang et al. 2021). SIMP J013656.5+093347 is detected with a peak-to-peak amplitude of 8% in the J band with a period of 2.4 hr (Artigau et al. 2009; Radigan et al. 2014). 2MASS J21392676+0220226 has a 26% peak-to-peak amplitude in the J band with a 7.7-hour periodic modulation and night-to-night variations (Radigan et al. 2012).

Although we have a number of young L-type planetary-mass objects, there were few known young T-type objects. Only one of them has been monitored for variability in the near-infrared (Ross 458c, Manjavacas et al. 2019b) and several have been monitored for variability in the mid-infrared (Vos et al. 2022). Identifying young T-type objects is more challenging, as they do not have prominent spectral features associated with surface gravity. Zhang et al. (2021) identify 30 new T0–T9 planetary-mass candidates of nearby young moving groups (YMG) based on their proper motions, parallaxes and available radial velocities, providing a sizeable sample of young T-type objects suited for time-resolved photometric studies. In this work, we present a first near-infrared variability survey of these T-type planetary-mass objects, which also includes several young mid-late L objects without existing variability monitoring, with the aim of estimating their variability rates, as it was performed earlier with young L dwarfs. Combining the results with previous surveys of field and young low-gravity L and T dwarfs, we make a statistical analysis of the variability of field and young objects from L0–T9 and investigate how variability properties depend on the spectral type and surface gravity.

2 SAMPLE

From the new planetary-mass candidate members detected in Zhang et al. (2021), we selected 12 objects with spectral types of T2.5–T8 that are bright enough ($J < \sim 17.5$ mag) for variability monitoring with a ground-based 4-m class telescope in the southern hemisphere. We also included six young L5–L7 dwarf candidate members identified with spectral and kinematic information from Kellogg et al. (2016), Schneider et al. (2016) and Schneider et al. (2017). In total, our sample consists of 18 L5–T8 YMG candidate members with masses $\leq 20 M_J$ and ages ≤ 200 Myr without previous near-infrared variability observations. They are members of the AB Doradus (149^{+51}_{-19} Myr, Bell et al. 2015), Argus (40–50 Myr, Zuckerman 2019), β Pictoris (22 ± 6 Myr, Shkolnik et al. 2017), Carina-Near (200 ± 50 Myr, Zuckerman et al. 2006) and TW Hydrae (TWA, 10 ± 3 Myr, Bell et al. 2015) moving groups. There are two known planetary-mass binaries in our sample, 2MASS J11193254–1137466AB (Best et al. 2017) and 2MASS J1553022+153236AB (Dupuy & Liu 2012), but neither are resolved in our observations. Table 1 lists the key information of these objects.

Table 1. Object information. Spectral type (SpT), magnitude, and membership with BANYAN II or BANYAN Σ (ref 4) probability are from the literature (Ref). The last column is the variability results in this work. Four variables are detected with two potential variable candidates.

Name	SpT	J	H	K	Mag	Binary	Membership	Ref	Variable
WISEA J004403.39+022810.6	L7	16.997±0.187	15.822±0.169	14.876±0.105	2MASS	N	Beta Pic (78%)	1	N
WISEA J020047.29-510521.4	L6	16.414±0.120	14.941±0.069	13.871±0.050	2MASS	N	AB Dor (98%)	1	N
WISEA J022609.16-161000.4	L6	17.334±0.266	15.750±0.142	14.581±0.093	2MASS	N	AB Dor (85%)	1	?
WISEA J114724.10-204021.3	L7	17.637±0.058	15.764±0.106	14.872±0.106	2MASS	N	TWA (96%)	2	Y
2MASS J11193254-1137466	L7	17.474±0.058	15.788±0.034	14.751±0.012	2MASS	Y	TWA (92%)	3	Y
WISE J024124.73-365328.0	T7	16.59±0.04	17.04±0.07	—	MKO	N	Argus (87.7%)	4	N
CFBDS J232304.41-015232.3	T6	17.23±0.03	17.46±0.04	17.30±0.03	MKO	N	Beta Pic (89.1%)	4	Y
WISEPCJ225540.74-311841.8	T8	17.33±0.01	17.66±0.03	17.42±0.05	MKO	N	Beta Pic (98.7%)	4	N
SDSSJ020742.48+000056.2	T4.5	16.73±0.01	16.81±0.04	16.72±0.05	MKO	N	Arg (95.6%)	4	N
WISEPAJ081958.05-033529.0	T4	14.78±0.02	14.60±0.05	14.64±0.05	MKO	N	Beta Pic (86.3%)	4	Y
ULASJ131610.13+031205.5	T3	16.75±0.02	16.13±0.02	15.43±0.02	MKO	N	Carina-Near (91.7%)	4	N
ULASJ081918.58+210310.4	T6	16.95±0.01	17.28±0.04	17.18±0.16	MKO	N	AB Dor (86.3%)	4	N
ULASJ075829.83+222526.7	T6.5	17.62±0.02	17.91±0.02	17.87±0.12	MKO	N	Arg (92.7%)	4	N
PSOJ168.1800-27.2264	T2.5	17.12±0.03	16.75±0.03	16.65±0.06	MKO	N	Arg (83.4%)	4	N
SDSSJ152103.24+013142.7	T3	16.10±0.01	15.68±0.01	15.57±0.02	MKO	N	Arg (82.3%)	4	N
WISE J163645.56-074325.1	T4.5	16.42±0.02	16.28±0.05	16.32±0.05	MKO	N	AB Dor (81.6%)	4	N
2MASS J1553022+153236AB	T7	15.34±0.03	15.76±0.03	15.94±0.03	MKO	Y	Carina-Near (89.6%)	4	?
WISEA J043718.77-550944.0	L5	16.985±0.192	15.583±0.157	14.640±0.098	2MASS	N	Beta Pic (94%)	1	N

References: (1) Schneider et al. (2017); (2) Schneider et al. (2016); (3) Kellogg et al. (2015); (4) Zhang et al. (2021).

3 OBSERVATIONS AND DATA REDUCTION

3.1 Observations

We conducted the first epoch survey of our 18 targets for 17 nights between October 2021 and June 2022 with the infrared spectrograph and imaging camera, Son of ISAAC (SOFI) on the 3.58 m ESO New Technology Telescope (NTT) at the La Silla Observatory (Moorwood et al. 1998). Brown dwarfs tend to have strong variability in the J band (Radigan et al. 2014), so our targets were primarily monitored in the J_S band. For targets that are extremely faint in J but much brighter in K , we observed them in the K_S band. For the two TWA objects with known variability at mid-infrared wavelengths, we obtained interleaved observations in the J_S and K_S band. The J_S band has a center wavelength at $1.24 \mu\text{m}$ with a width of $0.29 \mu\text{m}$, avoiding the water band at $1.4 \mu\text{m}$ in the J band; the K_S band is at $2.16 \mu\text{m}$ with a width of $0.28 \mu\text{m}$, avoiding the atmospheric absorption feature at $1.9 \mu\text{m}$ and elevated thermal background beyond $2.3 \mu\text{m}$ in the K band. The field of view of SOFI is $4'92 \times 4'92$ with a pixel scale of $0''.288$. Each target has continuous observations of 1.5–7.5 hr. The observations were affected by poor seeing in the October 2022 run and by clouds in the June 2022 run. We conducted a second epoch of ten nights between October 2022 and May 2023 to re-observe objects observed in poor conditions and confirm variables detected in the first epoch. Table 2 summarises the observing log.

Our targets were observed at airmass <2 . We used an ABBA nod pattern with three exposures at each position and 12 exposures in a loop. For each exposure, the detector integration time (DIT) is 20 s and the number of DIT (NDIT) is 3 in the J_S band and 10 s and 6 in the K_S band, respectively. For the interleaved observation, every 12 exposures in the J_S band were followed by 12 exposures in the K_S band. The peak intensity of the point spread function (PSF) of the target was kept below 10,000 ADU to prevent non-linearity effects.

3.2 Raw image reduction

We followed the data reduction steps in the SOFI manual to reduce raw images, which is also presented in Vos et al. (2019). 1) Cross

talk removal: a bright source can cause a ghost affecting the row where the source is and also the row in the other half of the detector, referred to as inter-quadrant row cross talk. These can be removed by subtracting 1.4×10^{-5} times the integrated flux of the row. 2) Flat fielding and shade pattern removal: when taking a flat, there is a difference between the shade pattern in the image with the lamp on and lamp off. Therefore, eight special dome flats were taken to do the flat-fielding including removing the residual shade pattern with the lamp on and off. 3) Illumination correction: the illumination of the dome panel is different from that of the sky, so a grid of 16 observations of a standard star was taken and we fitted a 2D surface to the photometry of the 16 positions to correct the difference in illumination between the dome panel and sky. 4) Sky subtraction and dark current correction: we subtracted frames by frames of different nods and closest in time to remove the fast-varying thermal background and also the dark current. We scaled the frame by the median flux ratio between it and the subtracted frame before the subtraction. 5) Bad pixel flagging: bad pixels were identified in the flat frame. The median of the flat frame was obtained after 3 sigma clipping. Pixels with flux deviation larger than 10 sigma from the median value were identified as bad pixels. The bad pixel map provided by ESO, which was created in 2012, was also combined into the final bad pixel map.

3.3 Aperture photometry

We used DAOSTARFINDER from the PHOTUTILS python package to detect sources in an image and fitted a 2D Gaussian model to the detected sources to accurately measure their positions. Then we performed aperture photometry on the detected stars with a series of aperture sizes fixed to all frames. We also took the median after $3\text{-}\sigma$ clip of a concentric annulus as the local background of the star and subtracted it from the aperture measurement. The inner radius of the annulus is 18 pixels and the outer radius of the annulus is 24 pixels. The final aperture size we used is determined in the light curve analysis as described below.

Table 2. Observing log. We measured the median full width at half maximum (FWHM) of all stars in each target’s field of view. We took the median of all frames as a seeing representative value for each target as listed in column FWHM. Column FWHM std is the standard deviation of all frames, representing seeing variations during observations.

Date	Object	Band	DIT×NDIT [s]	FWHM ["]	FWHM std ["]	Elapsed time [hr]
2021-10-20	J0044+0228	J_S	20×3	1.45	0.18	3.75
2021-10-20	J0200-5105	J_S	20×3	1.48	0.32	4.91
2021-10-21	J0241-3653	J_S	20×3	1.59	0.11	3.27
2021-10-21	J2323-0152	J_S	20×3	1.24	0.18	5.58
2021-10-22	J0226-1610	J_S	20×3	1.36	0.15	4.35
2021-10-22	J2255-3118	J_S	20×3	1.12	0.14	4.52
2021-10-23	J0044+0228	J_S	20×3	1.54	0.20	2.04
2021-10-23	J0207+0000	J_S	20×3	1.45	0.17	3.91
2021-10-23	J0241-3653	J_S	20×3	1.30	0.16	3.20
2021-10-24	J2323-0152	J_S	20×3	0.79	0.22	4.11
2021-10-24	J0226-1610	J_S	20×3	1.02	0.13	4.73
2022-02-10	J0819-0335	J_S	20×3	0.89	0.09	4.63
2022-02-10	J1316+0312	J_S	20×3	0.92	0.11	4.37
2022-02-11	J0819+2103	J_S	20×3	1.29	0.14	3.53
2022-02-11	2M1119-1137AB	K_S	10×6	0.88	0.10	4.47
2022-02-12	J0819-0335	J_S	20×3	1.17	0.18	3.13
2022-02-12	2M1119-1137AB	J_S	20×3	1.26	0.17	5.28
2022-02-12	2M1119-1137AB	K_S	10×6	1.11	0.14	5.29
2022-02-13	J0200-5105	J_S	20×3	1.58	0.28	1.92
2022-02-13	W1147-2040	K_S	10×6	1.34	0.13	7.31
2022-02-14	J0437-5509	K_S	10×6	0.96	0.10	2.80
2022-02-14	W1147-2040	J_S	20×3	0.93	0.11	5.80
2022-02-14	W1147-2040	K_S	10×6	0.91	0.10	6.32
2022-02-17	J0758+2225	J_S	20×3	0.94	0.12	3.19
2022-02-18	PSO168-27	J_S	20×3	1.06	0.24	4.10
2022-02-19	PSO168-27	J_S	20×3	0.84	0.16	4.96
2022-06-16	SDSSJ1521+0131	J_S	20×3	1.67	0.26	5.14
2022-06-16	J2323-0152	J_S	20×3	1.41	0.09	1.62
2022-06-17	WISEJ1636-0743	J_S	20×3	0.91	0.16	5.50
2022-06-17	J2323-0152	J_S	20×3	0.90	0.06	1.81
2022-06-18	SDSSJ1521+0131	J_S	20×3	0.71	0.05	2.06
2022-06-18	2M1553+1532	J_S	20×3	0.81	0.15	4.00
2022-06-19	WISEJ1636-0743	J_S	20×3	0.92	0.12	1.90
2022-10-09	J2323-0152	J_S	20×3	1.09	0.17	5.00
2022-10-09	J0200-5105	J_S	20×3	1.36	0.17	3.94
2022-10-10	J2323-0152	J_S	20×3	1.09	0.16	4.48
2022-10-10	J0200-5105	J_S	20×3	0.92	0.09	2.98
2022-11-02	J0226-1610	J_S	20×3	0.72	0.10	3.01
2022-12-03	J0200-5105	J_S	20×3	0.70	0.07	3.96
2022-12-03	J0819-0335	J_S	20×3	0.68	0.09	3.99
2022-12-04	J0226-1610	J_S	20×3	0.75	0.12	3.00
2022-12-04	J0819-0335	J_S	20×3	0.91	0.11	3.25
2023-05-06	W1147-2040	K_S	10×6	1.34	0.23	3.38
2023-05-07	2M1119-1137AB	K_S	10×6	0.81	0.12	4.18
2023-05-07	2M1553+1532	J_S	20×3	1.43	0.11	1.56
2023-05-08	2M1119-1137AB	K_S	10×6	0.98	0.15	4.88
2023-05-08	SDSSJ1521+0131	J_S	20×3	0.98	0.07	1.34
2023-05-09	2M1553+1532	J_S	20×3	1.18	0.23	3.00
2023-05-09	WISEJ1636-0743	J_S	20×3	0.99	0.14	1.87
2023-05-09	W1147-2040	K_S	10×6	0.89	0.20	5.80
2023-05-09	W1147-2040	J_S	20×3	0.94	0.24	5.28
2023-05-10	2M1119-1137AB	K_S	10×6	0.84	0.11	4.92
2023-05-10	2M1553+1532	J_S	20×3	1.10	0.09	3.05
2023-05-10	WISEJ1636-0743	J_S	20×3	0.95	0.08	2.49

3.4 Light curve analysis

The raw light curves contain conspicuous systematics, including the effects of seeing, airmass, atmosphere, and instrument. We selected reference stars in the field of view of the target to calibrate and

remove these systematics. At first, we excluded extremely faint stars and bright stars with flux in the non-linear regime ($> 10,000$ ADU). Second, for each star, the raw light curves of different nods were normalised by their own medians. Then the normalised light curves of different nods were corrected to the same baseline. This step scales

the light curves of different stars to the same level. We then selected a set of well-behaved reference stars to build a calibration light curve for the target. We used the same iteration algorithm from Radigan et al. (2014) and Vos et al. (2019). First, stars affected by bad pixels were discarded. Then for each star, its calibration light curve was created from the median light curve of the other candidate reference stars. We divided the calibration light curve from the light curve of the star to remove the variations caused by systematics. Good reference stars should have no intrinsic variations and have flat light curves after detrending. To exclude the effects of outliers, we calculated the robust standard deviation and robust linear slope of detrended light curves. Stars with sigma and slope $< \sim 1.2$ – 3 times that of the target were retained for the next iteration. These steps were repeated several times until a set of well-behaved reference stars was chosen. We further removed some reference stars that showed variability after the iteration algorithm by visual inspection. We applied this iteration algorithm to light curves of different aperture sizes. For each target, the final aperture we used was the same as or close to the median full width at half maximum (FWHM) of the PSFs of all stars in all frames of the target, which results in the smallest photometric noise. The photometric noise of the detrended light curve, σ_{pt} , was estimated by the robust standard deviation of the subtraction of a light curve shifted by one time bin from the original light curve, divided by $\sqrt{2}$, the same method used in Radigan et al. (2014). This method is sensitive to high-frequency noise but not sensitive to low-frequency noise such as intrinsic astrophysical variability trends in light curves. It performs better than the standard deviation in quantifying the photometric noise and uncertainty of detrended light curves, especially for variable targets.

4 VARIABILITY ANALYSIS

The variability of the targets was detected using a periodogram analysis of their detrended light curves. We used the Lomb-Scargle (LS) periodogram method as the primary analysis tool (Lomb 1976; Scargle 1982). We also used a secondary analysis, the Bayesian Generalized Lomb-Scargle (BGLS) periodogram, to independently verify the peaks in the LS periodogram (Mortier et al. 2015). Manjavacas et al. (2018) find that unlike LS, BGLS is insensitive to gaps in light curves. BGLS calculates the relative probability between peaks rather than the power spectrum calculated by the LS periodogram. The peaks detected in the BGLS periodogram agree with those detected in the LS periodogram of our light curves. We also calculated the LS periodogram of detrended reference light curves, the seeing curve over the observation and the window function of the observation cadence. If the peaks in these periodograms matched those in the target light curve, they were considered false detections due to residual systematic effects. The window function was calculated as a light curve with a flux of 1 without pre-centering or using a floating-mean model in the LS calculation (VanderPlas 2018).

To assess the significance of the peaks in the periodogram, we calculated the 1% false-alarm probability (FAP) level using the Astropy.timeseries Python package. We used the bootstrap option in that routine to calculate the peak level of 1% FAP, which is equivalent to simulating the light curve and calculating the periodogram over 10^3 times. Radigan et al. (2014) and Vos et al. (2019) calculated the 1% FAP level also by randomly permuting reference star light curves 1000 times and the β factor of every light curve which is the peak value in its periodogram divided by the 1% FAP level. They expected to have 1% reference stars with a β factor above 1 but found that more than 1% reference stars peaked above this level. Therefore,

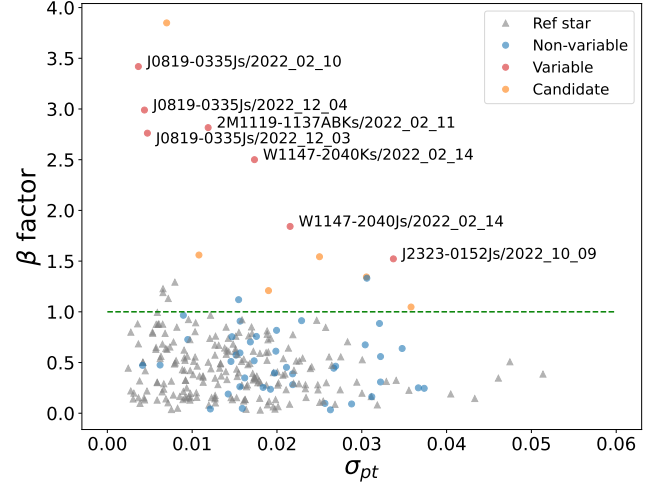


Figure 1. β factor against the photometric error of a detrended light curve, σ_{pt} . The β factor is calculated by the periodogram power peak of every light curve divided by its own 1% FAP level. The four confirmed variable targets (red) fall above $\beta = 1$. 1.8% of reference stars fall above $\beta = 1$, which is very close to the expected value, 1%. Potential variable candidates are orange circles and non-variable targets are blue circles. The reference stars are shown by grey triangles.

they scaled the 1% FAP level by a factor between 1.4 and 3.4. Because we included the light curve uncertainty in the LS periodogram calculation and applied the ‘standard’ normalisation in that routine, the power spectra value should not be compared directly between the target and reference star light curves. We also randomly permuted the target light curve 1000 times and found that the 1% FAP level calculated automatically by the bootstrap routine in Astropy.timeseries is always higher than the 1% FAP level calculated by our version of 1000 random permutations of the target light curve. We adopted the 1% FAP level calculated with Astropy.timeseries. We also calculated the β factor by dividing the periodogram power peak of every light curve by its own 1% FAP level. Four out of 216 reference stars fall above $\beta = 1$ in Fig. 1, which is close to 1%. Eriksson et al. (2019) used the 0.1% FAP level with the ASTROPY routine for the variability detection in their light curves. We also calculated the 0.1% FAP level and found our confirmed detections remain significant when using this level.

If the peak in the target periodogram is above the 1% FAP level and the detrended light curve has a well-behaved appearance upon visual inspection, the target is identified as a variable object; if the peak in the target periodogram is above the 1% FAP level but the detrended light curve is not well-behaved, it is identified as a potential variable candidate; if no peak in the periodogram exceeds the 1% FAP level, the object is identified as non-variable in this survey. While the period of the detected variability can also be estimated from the periodogram, many targets did not have a clearly defined peak in their periodogram, indicating the presence of long-term variability that exceeds the duration of our observations. In these cases, we can only place lower limits on the period.

We also calculated the instrumental magnitude and median absolute deviation (MAD) of the detrended light curve which is similar to the standard deviation but not sensitive to outliers. Although MAD increases generally with fainter stars, we do not find a consistent relationship between the MAD and the instrumental magnitude between different observations. For some observations, their relationship can

Table 3. Detected variables in this work. The amplitude is the peak-to-peak amplitude. Binaries are not resolvable with NTT.

Target	SpT	Band	Amplitude	Period [hr]	Binary
2M1119-1137AB	L7	K_S	$3.2 \pm 0.8\%$	6.9 ± 1.6	Y
W1147-2040	L7	J_S	$4.6 \pm 1.0\%$	11.2 ± 3.8	N
		K_S	$4.8 \pm 0.4\%$	5.5 ± 0.2	
J0819-0335	T4	J_S	$1.8 \pm 0.8\%$	Long	N
J2323-0152	T6	J_S	$\sim 7.6\%$	Long	N

be fitted with a second-order polynomial as the relationship presented [Martín et al. \(2001\)](#). For some observations, there is not a monotonous relationship between MAD and the instrumental magnitude. Figure 2 shows one object 2M1119-1137AB and the selected reference stars and their MAD-magnitude relationship. The same figures for all other observations can be found in Appendix A. Therefore, using the relationship between the standard deviation and the magnitude to do variability analysis as the method used in [Martín et al. \(2001\)](#) is not applicable to our datasets.

5 SENSITIVITY CALCULATION

To estimate our detection sensitivity for each observation, we injected artificial sinusoidal curves into randomly permuted detrended target light curves. For variable light curves, we fitted a low-order polynomial fitting or a sinusoidal curve before the injection to remove its variability. The injected peak-to-peak amplitude ($2 \times$ amplitude of the sinusoidal curve) varies from 0.5% to 10% and the period varies from 1.5 to 20 hours. In each grid, we injected the sinusoidal curves 1000 times and calculated the detection rate. The successful retrieval criterion is that the peak of the injected curves in the periodogram is above the 1% FAP level.

6 RESULTS

We detect four new variables, two variable candidates and twelve non-variables. Table 1 lists the variability detection results of all objects in this work. Table 3 summarises the amplitude and period information of variable objects. The detections are mainly limited by seeing. As shown in Fig. 3, all the positive detections were observed under a seeing $< 1''$. They do not have a strong correlation on the apparent magnitude as we have positive detections from faint to bright targets.

6.1 Significant detections

WISEPAJ081958.05-033529.0: this T4 dwarf is a high-probability member of the β Pictoris young moving group identified by [Zhang et al. \(2021\)](#) with trigonometric parallax, though it needs an RV measurement for confirmation. Assigning an age of ~ 20 Myr to it, it has an estimated mass of $\sim 5.7 M_J$ ([Zhang et al. 2021](#)). We observed it on four nights in the J_S band: 10 Feb 2022 and 12 Feb 2022 in the first epoch and 03 Dec 2022 and 04 Dec 2022 in the second epoch. We detected variability on three nights but not on 12 Feb 2022. The variable light curves are shown in Fig. 4 and the non-variable light curve is in Appendix C. The light curve of 10 Feb 2022 presents an obvious downward slope. We fit a line to it using the least-squares algorithm and find a peak-to-peak variability amplitude (max-min) of $1.2 \pm 0.1\%$ in the 4.63-hour observation. This variability is far above

the 1% FAP level in its periodogram. If it is a periodic signal, the period is longer than the observation length. As our observation does not cover a full rotation, the fitted variability amplitude is a lower limit. We detected no variability on 12 Feb 2022. The light curve of 12 Feb 2022 has a marginal downward slope by visual inspection but it is not detected in its periodogram. The relatively poorer seeing of the second night degrades the detection sensitivity, which can be seen from its sensitivity plot. In fact, the variability of the first night would not be detectable on the second night. It is one of the reasons why there is no variability detection on the second night. Another reason could be that the object has a long rotation period and reached the peak of its light curve on 12 Feb 2022 where relative variability would be lower as compared to the slope between extrema and thus it does not present an apparent relative variability during the three-hour observation.

We fit a second-order polynomial curve to the light curve of 03 Dec 2022 and measure a peak-to-peak amplitude of $1.8 \pm 0.8\%$. If it is a periodic signal, its period is longer than the observation length, 4 hr. Fitting a sinusoidal curve to the light curve of 04 Dec 2022, we measure a peak-to-peak amplitude of $1.2 \pm 0.1\%$ with a period of 2.6 ± 0.1 hr. We suspect that J0819-0335 has a period > 5 hr and the light curve was transitioning from a downward to an upward trend during the observation on 04 Dec 2022. This is why a short-period sinusoidal light curve was observed. Further longer continuous observations are necessary to determine the true period of this young object.

2MASS J11193254-1137466AB: 2M1119-1137AB has extremely red optical and near-infrared colours ([Kellogg et al. 2015](#)). It was first characterised as a low-mass L7 dwarf and a high probability candidate of the TW Hydrae Association (TWA) by [Kellogg et al. \(2015, 2016\)](#). [Best et al. \(2017\)](#) resolve it to be a binary system of two similar $\sim 3.7 M_J$ L7 brown dwarfs with a separation of $0''.14$, adopting the 10 Myr age of TWA. The orbital period of this system is about 90 years. It is a flux reversal binary as one component is slightly brighter in the J band but fainter in the K band. [Schneider et al. \(2018\)](#) report mid-infrared variability with a period of $3.02^{+0.04}_{-0.03}$ hr and semi-amplitudes of $0.230^{+0.036}_{-0.035}\%$ at $3.6 \mu\text{m}$ and $0.453 \pm 0.037\%$ at $4.5 \mu\text{m}$ for this system in *Spitzer* observations. These light curves have also been suggested to show evidence of an exomoon ([Limbach et al. 2021](#)). SOFI was unable to resolve this system. We observed it on two continuous nights in the first epoch: 11 Feb 2022 in the K_S band and 12 Feb 2022 interleaved in the J_S and K_S bands. We detected significant variability on the first night as shown in Fig. 5. We fit a sinusoidal curve to the light curve in the K_S band using the Levenberg-Marquardt least-squares (LM) method and find a peak-to-peak amplitude of $3.2 \pm 0.8\%$ and a period of 6.9 ± 1.6 hr. Our observation does not cover a complete cycle and thus this period needs further confirmation.

This period is longer than the variability period of 3.02 hr at 3.6 and $4.5 \mu\text{m}$ reported by ([Schneider et al. 2018](#)). To fit a sinusoidal curve with a fixed period of 3.02 hr, we need to add a linear term of $0.0047t$ to the sinusoidal curve as shown in Fig. 6, yielding a semi-amplitude of 0.86% for the sinusoidal curve. As 2M1119-1137AB is a binary system, the linear term and sinusoidal term could be attributed to the two components respectively. [Schneider et al. \(2018\)](#) suspect that their measured variability with the period of 3.02 hr possibly comes from one component of the binary, similar to the L7.5+T0.5 binary WISE J104915.57-531906.1AB ([Burgasser et al. 2014](#)). Further observations with larger telescopes such as the very large telescope (VLT) are necessary to resolve the variability of the two components. If confirmed, 2M1119-1137AB would be one of

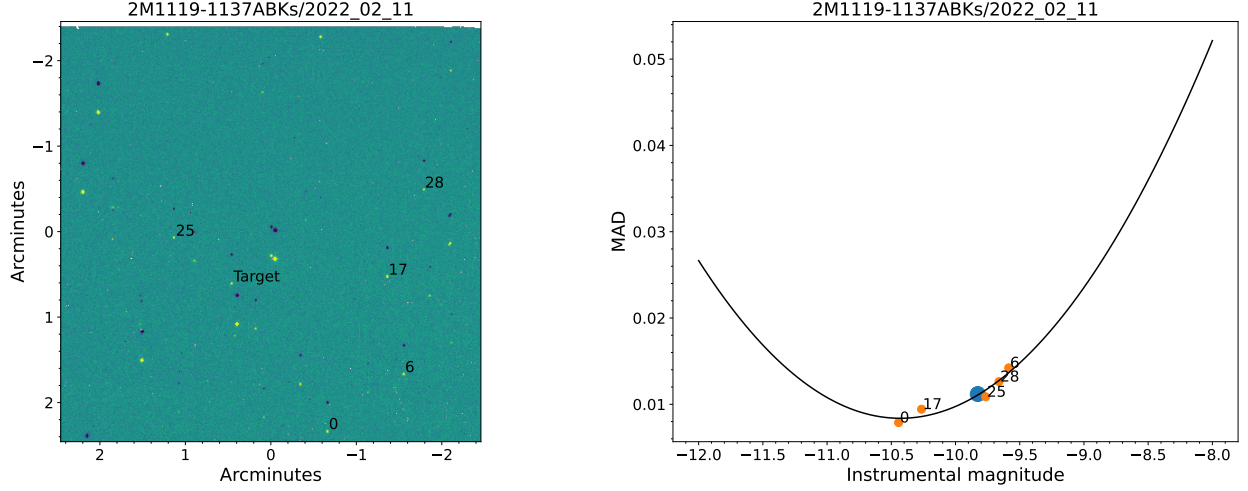


Figure 2. Target 2M1119-1137AB in the K_S band and the selected reference stars of the observation on 11 Feb 2022. Left: the sky subtracted image. It is one nod subtracted from the other nod, which results in these dark sources. The textual label of the reference stars is their original number before the reference star selection. North is left and east is down. Right: the MAD and instrumental magnitude of the reference stars (orange) and target (blue). The black line is a second-order polynomial fitting to the reference stars. This target meets the MAD-magnitude relationship of the reference stars but it is variable.

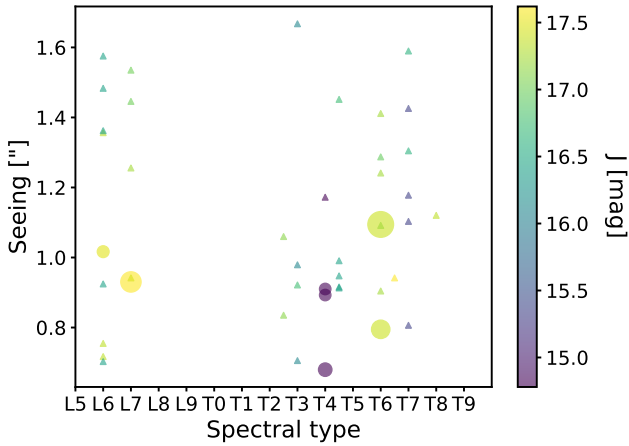


Figure 3. Observation and detection diagram in the J_S band. Circles represent positive detections with the radius proportional to the variability amplitude. Triangles represent non-detection observations. The colour represents the apparent magnitude of the target in the J band. All variable detections were observed under a seeing $< 1''$, while they do not have a strong dependence on the magnitude.

the few young L and T dwarfs with periods $< \sim 3$ hours. As brown dwarfs are expected to rotate faster as they age and contract because of angular momentum conservation (Schneider et al. 2018), young objects with short periods are rare.

The second night was observed under poorer seeing conditions than the previous night and we do not detect any variability. The $\sim 3\%$ variability of the first night could not be reliably detected under the conditions of the second night. We observed it another three times in May 2023 in the K_S band but detected no variability due to poor seeing or clouds. The non-detection results can be found in Appendix C.

WISEA J114724.10-204021.3: W1147-2040 is an L7 dwarf with an extremely red 2MASS $J - K_S$ colour and a mass of 5-13 M_J (Schneider et al. 2016). Its spectrum has obvious evidence of youth.

Schneider et al. (2016) identify it as a high probability member of the TWA using its sky position and proper motion. Schneider et al. (2018) find variability with a period of $19.39^{+0.33}_{-0.28}$ hr by combining its *Spitzer* light curves at $3.6 \mu\text{m}$ and $4.5 \mu\text{m}$. The light curves have a semi-amplitude of $0.798^{+0.081}_{-0.083}\%$ and $1.108^{+0.093}_{-0.094}\%$, respectively. We observed it on two consecutive nights: 13 Feb 2022 and 14 Feb 2022. It was monitored in the K_S band on the first night under relatively poor seeing conditions and we did not detect significant variability. These plots are in Appendix C. The observations on the second night were interleaved in the J_S and K_S bands with seeing about $0''.9$. We detect variability in both bands with significance higher than 99% as shown in Fig. 7. We fit a sinusoidal curve to each light curve using the LM method. We find a peak-to-peak amplitude of $4.6 \pm 1.0\%$ with a period of 11.2 ± 3.8 hr in the J_S band and a peak-to-peak amplitude of $4.8 \pm 0.4\%$ with a period of 5.5 ± 0.2 hr in the K_S band. The K_S band light curve just covers a full period while the J_S band light curve does not. The periods in the J_S band, K_S band, and mid-infrared of this target are quite different. We are cautious about whether these differences are astrophysical since these observations are relatively short compared to their measured periods. We also fit the curves with a sinusoidal curve with the period in the mid-infrared. The fitting in the J_S band is acceptable while the K_S band is poorly-fitted. We did follow-up observations of it on 06 May 2023 in the K_S band and on 09 May 2023 interleaved in the K_S and J_S band. Only the J_S band on the second night presents variability. Its periodogram shows a peak above the 1%FAP level around 6 hr but it coincides with the seeing curve. We consider this night as a possible detection and the light curves are presented in Appendix B. The light curves of 06 May can be found in Appendix C.

CFBDS J232304.41-015232.3: discovered by Albert et al. (2011), this T6 dwarf is identified as a high-probability member of β Pictoris with a mass of $\sim 4.8 M_J$ (Zhang et al. 2021). We observed J2323-0152 on 21 Oct 2021 and 24 Oct 2021 in the first epoch and 09 Oct 2023 and 10 Oct 2022 in the second epoch. We also observed J2323-0152 on 16 Jun 2022 and 17 Jun 2022 less than two hours per night. But these observations were taken under high humidity or cloudy conditions without any variability detection. We detected no variability on 21 Oct 2021 and 10 Oct 2022. These non-variable light

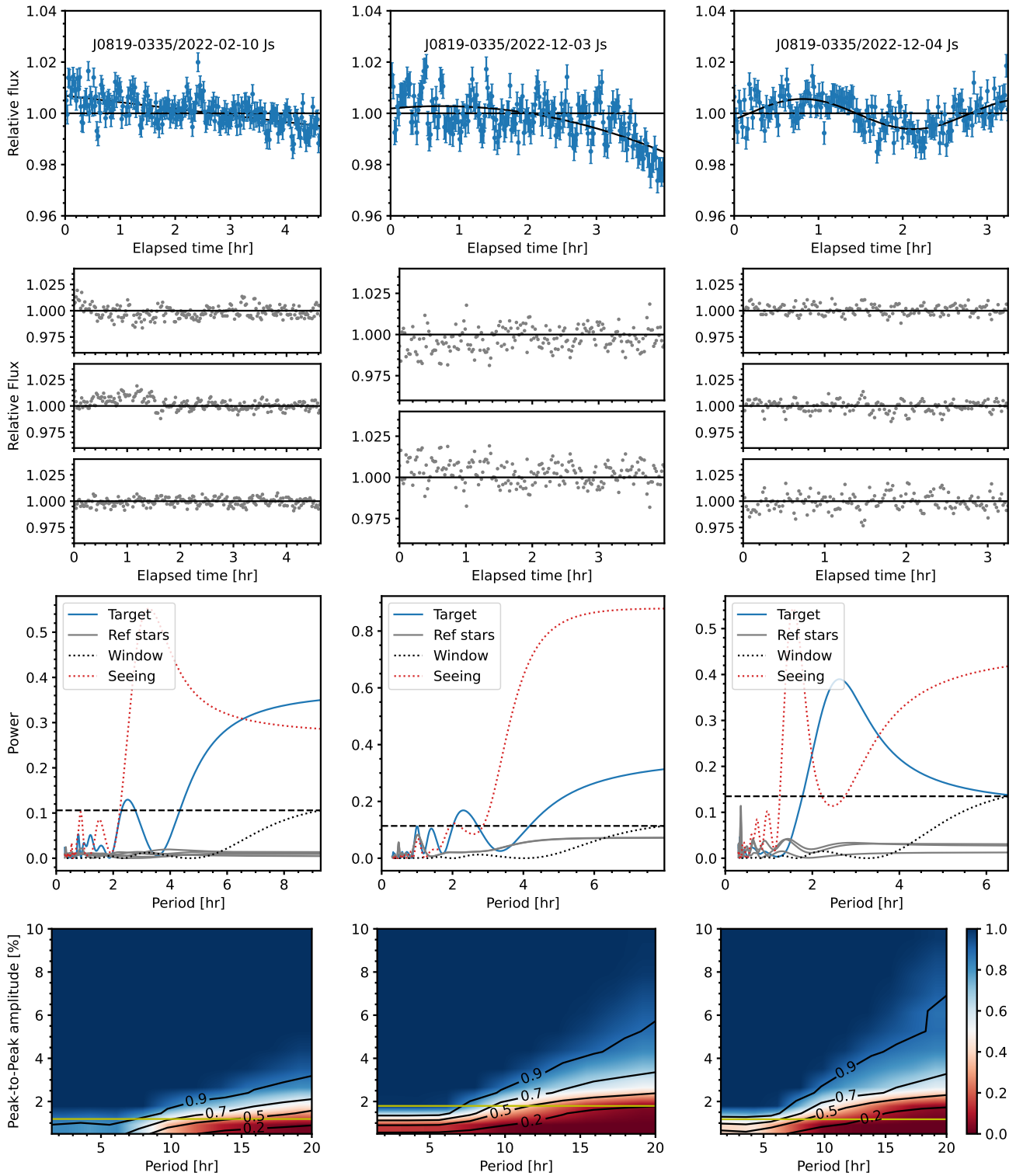


Figure 4. Results of a variable object, J0819-0335. Top row: detrended light curve. Second row: detrended light curve of its reference stars (show up to three stars). Third row: Lomb-Scargle periodogram of the detrended light curve of the target. We also include the periodograms of the detrended light curves of reference stars, seeing curve, and window function. They help to identify unremoved systematic variability in the detrended light curve of the target. Dashed line is the 1% FAP level of the target. Bottom row: sensitivity plot calculated from injected signals. The yellow line shows the measured amplitude. The X-axis and Y-axis are the period and peak-to-peak amplitude of the injected sinusoidal signal, respectively. The signal is injected into the variability-removed light curve of the target. The colour bar is the retrieval rate by our method, ranging from 0 to 1.

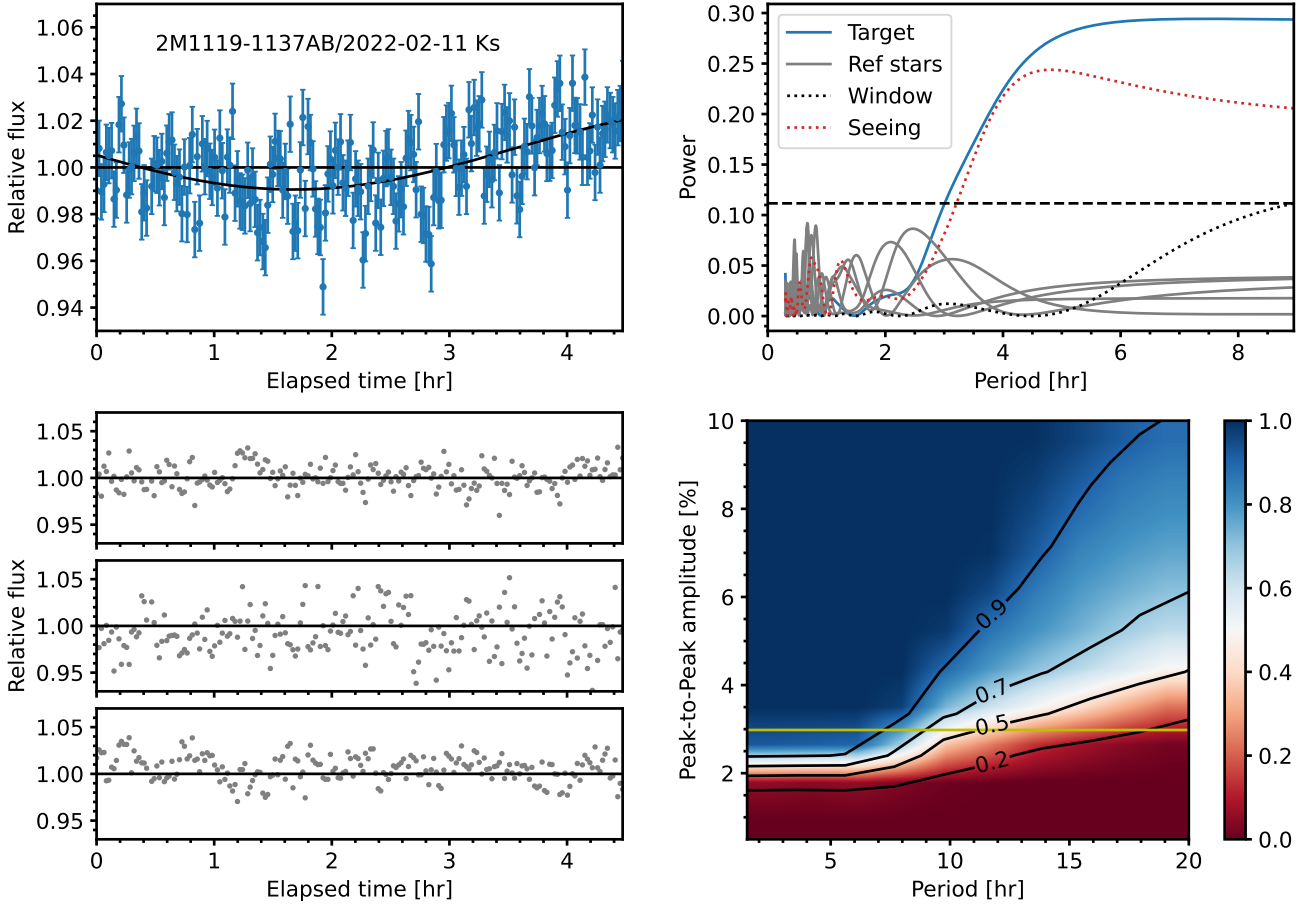


Figure 5. Variable light curve, periodogram and sensitivity plot of 2M1119-1137AB, including detrended light curves and periodograms of its reference stars. The variability is detected in the K_S band.

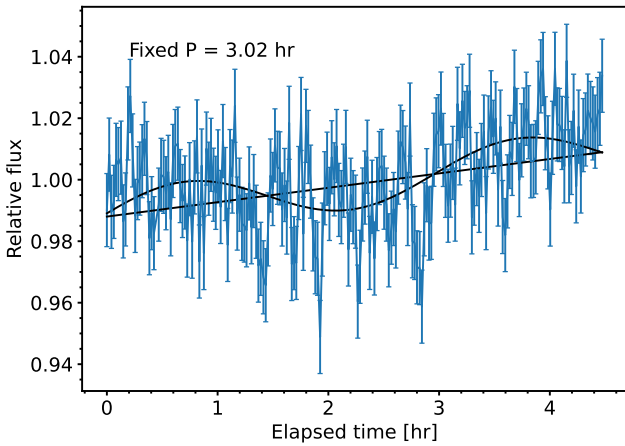


Figure 6. Variable light curve of 2M1119-1147AB, fitted with a linear term and a sinusoidal curve with a fixed period of 3.02 hr, which is its variability period at 3.6 and 4.5 μm . Its K_S -band light curve can be depicted by two variability terms which may come from the two components

curves are shown in Appendix C. We have positive detections on 24 Oct 2021 and 09 Oct 2022. The results are shown in Fig. 8. We find marginal variability just above the 1% FAP level on 24 Oct 2021. The

peak around ~ 2 hr in the periodogram of 24 Oct 2021 is close to the peak of the seeing curve. This peak is likely related to the residual seeing effect since we were only able to pick two good reference stars. There is another long-term variability according to the periodogram. The light curve shows a variable pattern with a decreasing trend and a plateau-shaped enhancement on 09 Oct 2022, which is confirmed to be significant in the periodogram with a reported period of 3.15 hr, but this period is not evident from visual inspection of the light curve. If we assume the variability is caused by this decreasing trend with a plateau-shaped enhancement, the period is longer than the observing length of 5 hr. The max-min amplitude of the light curve of 09 Oct 2022 is $\sim 7.6\%$. We also notice that the light curve of 24 Oct 2021 begins to rise at the end, which is likely another plateau-shaped enhancement. We also fit a linear trend with a plateau-shaped enhancement to this light curve and measure a max-min amplitude of $\sim 3.7\%$. Therefore, J2323-0152 is classified as a variable with a long period.

6.2 Variable candidates

We identify two potentially variable candidates. Although they present variability above the 1% FAP level, we are cautious in our interpretation of these results due to the low quality of the data. Their light curves, periodograms, and sensitivity plots can be found in Appendix B.

2MASS J1553022+153236AB: 2M1553+1532 is a T7 candidate

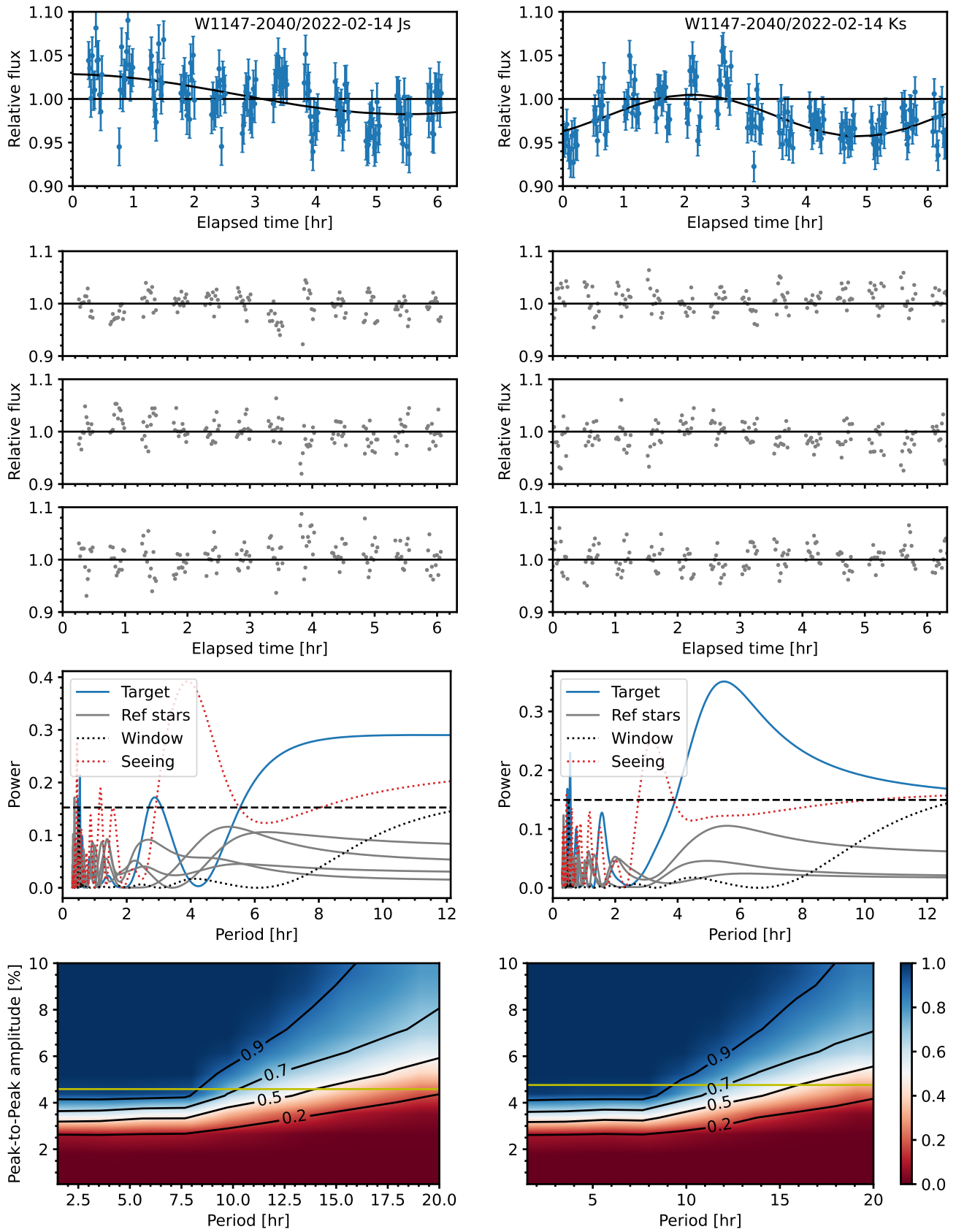


Figure 7. Variable light curves, periodograms, and sensitivity plots of W1147-2040, including detrended light curves and periodograms of its reference stars. The observations were interleaved in the J_S and K_S bands.

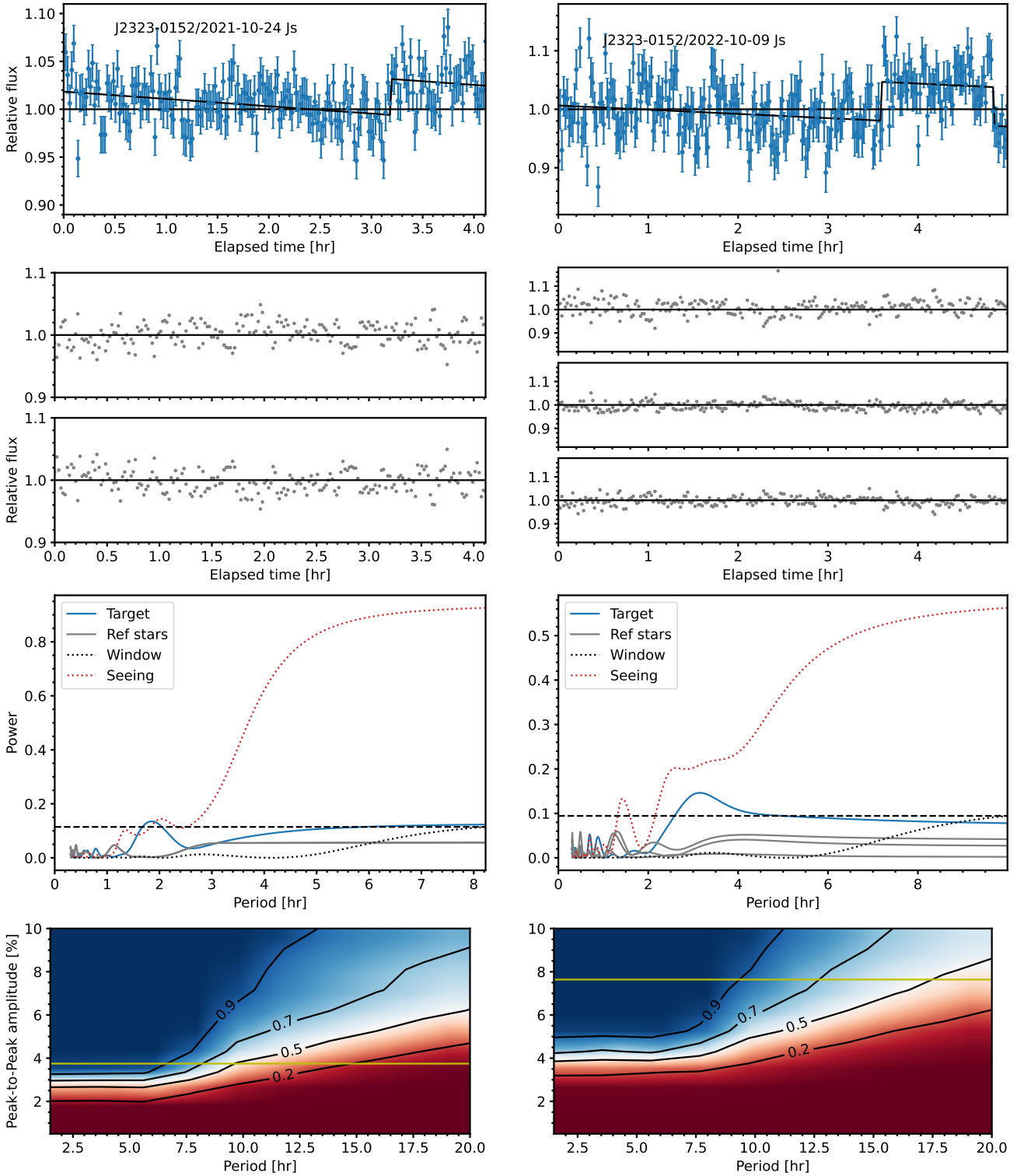


Figure 8. Variable light curves, periodograms, and sensitivity plots of J2323-0152 on 24 Oct 2021 and 09 Oct 2022, including detrended light curves and periodograms of its reference stars.

of the Carina-Near YMG with a probability of 89.6% and an estimated mass of $12 M_J$ according to [Zhang et al. \(2021\)](#) using the trigonometric parallax. It was initially resolved to be a field binary system of two T6.5+T7.5 dwarfs ([Burgasser et al. 2002, 2006](#); [Dupuy & Liu 2012](#)). The separation is about $0''.6$ in the resolved image of

[Dupuy & Liu \(2012\)](#). It was not resolvable with SOFI. We detected long-term variability on 18 Jun 2022 and 09 May 2023. However, its periodogram shows a similar trend as the periodogram of the seeing curve on both nights and we were only able to select two good reference stars on both nights. The variability is suspicious. It might be

a coincidence because the impact of the seeing variations should be removed after detrending with the reference stars as the detrended light curves of the reference stars are flat. We also observed it on 07 May 2023 for 1.56 hr and 10 May 2023 for 3.02 hr but did not detect any variability. Therefore, we consider it a potential variable.

WISEA J022609.16-161000.4: this L6 dwarf is a high-probability member of AB Doradus and has a mass range of 16–28 M_J (Schneider et al. 2017). We observed it on two nights: 22 Oct 2021 and 24 Oct 2021. On the first night, poor weather conditions resulted in the loss of two hours of data and no variability was detected. The weather conditions were much better on the second night. The periodogram detects two peaks above the 1% FAP level. The first peak around 2.3 hr coincides with the peaks of reference stars, raising suspicions of systematic variability. The second peak is actually a plateau towards long periods, showing long-term variability. However, selecting suitable reference stars for this target is challenging as there are few point sources in the field. Only three faint reference stars were chosen and their own detrended light curves are quite noisy, reducing the quality of the calibration curve created with them. We re-observed it on 02 Nov 2022 and 04 Dec 2022. There is a peak at 2.19 hr in the periodogram of 02 Nov 2022 but this variability is not evident in the visual inspection of the light curve. The light curve on 04 Dec 2022 did not show any variability. We consider J0226-1610 a potential variable.

6.3 Non-detections

We do not detect significant variability in eleven targets, including two L dwarfs and nine T dwarfs. Their light curves, periodograms and sensitivity plots are presented in Appendix C. Several noteworthy targets are discussed below.

WISEA J004403.39+022810.6: discovered by Skrzypek et al. (2016), this L7 dwarf is a high-probability member of β Pictoris with a mass of 7–11 M_J (Schneider et al. 2017). We observed it on two nights: 3.75 hr on 20 Oct 2021 and 2.04 hr on 23 Oct 2021. We detect no variability in its light curves.

WISEA J020047.29-510521.4: J0200-5105 is a high-probability member of AB Doradus and is identified as an L6–L9 dwarf with a mass range of 16–28 M_J (Schneider et al. 2017). We observed it on 20 Oct 2021 in the first epoch and did not detect variability above the 1% FAP level. The seeing changed from 1''0 to 2''3 during the observation. Due to the poor seeing conditions, we re-observed it on four nights: 13 Feb 2022, 09 Oct 2022, 10 Oct 2022, and 03 Dec 2022. No variability is detected in the light curves of these observations.

ULASJ075829.83+222526.7: discovered by Burningham et al. (2013), this T6.5 dwarf is a high-probability member of Argus with a mass of approximately 4.8 M_J (Zhang et al. 2021). With a J magnitude of 17.62, it is the faintest target in our survey. It was observed under favourable conditions on 17 Feb 2022 for 3.2 hr. While its light curve appears to exhibit a decreasing trend, this variability was below the 1% FAP level according to the periodogram. Further observations may provide evidence to confirm this variability.

PSOJ168.1800-27.2264: the T2.5 dwarf, discovered by Best et al. (2015), is a likely member of the Argus group identified with photometric parallax (Zhang et al. 2021). It has a mass of $\sim 8 M_J$. We observed it on two consecutive nights: 4.1 hr on 18 Feb 2022 and 5.0 hr on 19 Feb 2022. No significant variability is detected in its light curves.

WISEA J043718.77-550944.0: this L5 dwarf was identified as a high-probability member of β Pictoris by Schneider et al. (2017). However, its predicted distance and surface gravity have conflicting results from different methods, making its youth and membership

status uncertain. Due to a shortage of suitable observation targets in Feb 2022, we observed J0437-5509 on 14 Feb 2022 for 2.8 hours. The periodogram analysis of its light curve does not detect any variability.

7 STATISTICAL ANALYSIS

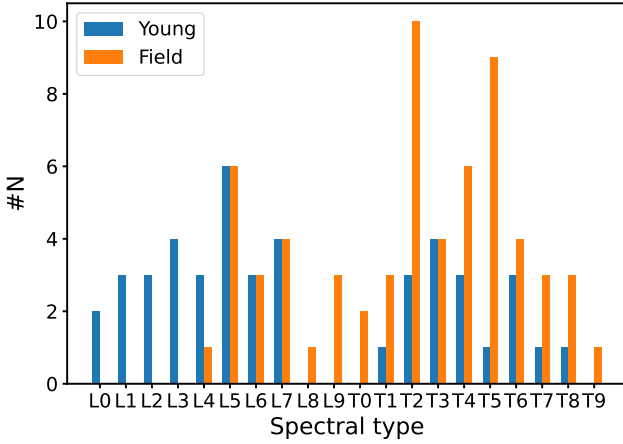
Our sample provides a first investigation of the variability of young planetary-mass T dwarfs. To gain a comprehensive understanding of the variability of both young and field L and T dwarfs at near-infrared wavelengths, we combine our survey with previous studies. These include the variability survey of young L dwarfs from Vos et al. (2019), the variability survey of field L and T dwarfs from Radigan et al. (2014), and the smaller variability survey of field objects at the L/T transition from Eriksson et al. (2019). All of these studies were conducted using ground-based photometric monitoring campaigns in the J band, similar to our own. They also employed similar variability identification criteria, with a variability significance level higher than the 1% FAP level in the LS periodogram (except for 0.1% FAP in Eriksson et al. (2019)). The sensitivity plots of samples from our survey, Vos et al. (2019) and Radigan et al. (2014) are also calculated in a similar way by injecting and detecting the simulated sinusoidal signals in the light curves. We extract the light curves from Eriksson et al. (2019) and calculate their sensitivity plots using the same method. Therefore, it is reasonable to compare them statistically.

We exclude known binary objects in the statistical analysis, as their variability may be due to one or both components or eclipsing binaries. We also exclude objects with uncertain youth, as our goal is to compare variability between young and field objects. The two variables in Radigan et al. (2014), SIMP0136+0933 and 2MASS2139+0220, were originally classified as field T dwarfs but were later found to be members of the Carina-Near YMG (Gagné et al. 2017b; Zhang et al. 2021). We include the two variables in the sample of young objects instead of the field sample. Another variable T dwarf in Eriksson et al. (2019), 2MASS0013-1143, also turned out to be a candidate member of the Argus YMG (Zhang et al. 2021) and is added to the young sample. One variable T2 dwarf in Vos et al. (2019), PSO071, was initially identified as a likely member of β Pictoris by Best et al. (2015), but was later classified as a field dwarf by Best et al. (2020); Marocco et al. (2021). Thus we include it in the field T sample. We consider only significant variability detections as variables in the statistical analysis. Marginal detections or potential variable candidates are considered non-variables. We also exclude two objects that were observed for less than 2 hr in Eriksson et al. (2019). Additionally, one variable from their sample, 2M2239+1617, has variability significance below the 1% FAP level in our periodogram analysis and thus we consider it non-variable. In total, we have 45 (10 variables) young objects consisting of 15 (3) from our survey, 26 (4) from Vos et al. (2019), 2 (2) from Radigan et al. (2014) and 1 (1) from Eriksson et al. (2019), and 63 (10 variables) field objects including 55 (7) from Radigan et al. (2014), 7 (2) from Eriksson et al. (2019) and 1 (1) from Vos et al. (2019). Table 4 lists the numbers of L and T brown dwarfs included in the statistical analysis. Figure 9 shows the spectral distribution. Young objects span from L0 to T8 and field objects span from L4 to T9. The averaged sensitivity maps of this survey, Vos et al. (2019), and Radigan et al. (2014) are shown in Fig. 10. Our objects are fainter than objects in Vos et al. (2019) and were observed under poorer conditions, while field dwarfs in Radigan et al. (2014) are much brighter than young objects. Therefore, it is easier for Radigan et al. (2014) to detect weaker variability.

Figure 11 illustrates the relationship between spectral type and

Table 4. Brown dwarfs included in the statistical analysis.

Type	Variable	Non-Variable	Total
Young L	5	23	28
Young T	5	12	17
Young L and T	10	35	45
Field L	1	17	18
Field T	9	36	45
Field L and T	10	53	63


Figure 9. Spectral distribution of brown dwarfs included in the statistical analysis.

2MASS $J - K_S$ colour of variable objects from the four surveys. The field sequence objects are taken from the UltracoolSheet¹ (Best et al. 2020), a catalogue of over 3,000 ultracool dwarfs and directly-imaged exoplanets. Some young T dwarfs in our sample have only MKO magnitudes and we convert their MKO $J - K$ colour to the 2MASS photometric system using the transformation equation². Strong variables with peak-to-peak amplitude $> 2\%$ are concentrated within a narrow range, with strong young variables assembling in L7–T6 and strong field variables gathering from T1 to T3, a narrower distribution compared to strong young variables.

7.1 Statistical formalism

Although we can estimate the variability rate of brown dwarfs by the ratio of the number of variables to the total number, this is biased by the detection sensitivity which can vary significantly between different observations. To include the effect of detection sensitivity, we adopted the statistical formalism used in Vos et al. (2019) and Vos et al. (2022), which is a Bayesian method based on Lafrenière et al. (2007) and Bonavita et al. (2013). f is the variability frequency with amplitude and rotation period in the interval $[a_{min}, a_{max}] \cap [r_{min}, r_{max}]$. If we number the observations of N objects by $j = 1 \dots N$, p_j is the probability that such variability would be detected in observation j . In the sensitivity map calculated for each observation, $g(r, a)$ is the detection rate of the injected sinusoidal signals in each

grid. p_j is the integral of $g(r, a)$ over the considered amplitude and period ranges of the injected signals normalised by the area of the map:

$$p_j = \frac{\int_{a_{min}}^{a_{max}} \int_{r_{min}}^{r_{max}} g(a, r) da dr}{\int_{a_{min}}^{a_{max}} \int_{r_{min}}^{r_{max}} 1 da dr} \quad (1)$$

In our case, $0.005 \leq a \leq 0.1$ and $1.5 \leq r \leq 20 \text{ hr}$ as we inject these signals to calculate the sensitivity map. We choose the amplitude and period boundaries to keep the sensitivity map consistent with the maps of Vos et al. (2019) and Radigan et al. (2014). Though our average sensitivity rate is smaller than 0.2 when the amplitude is smaller than 2% in Fig. 10, we are able to detect amplitude as low as 0.5% when the observation conditions are good and the targets are bright such as the observations of J0819-0335 in Fig. 4. The lower boundary of the period is the shortest observation length and the upper boundary is an arbitrarily long period.

The probability of detecting one object to be variable is therefore fp_j and non-variable is $1 - fp_j$. The detection made in observation j is d_j : $d_j = 1$ for positive detection and $d_j = 0$ for non-detection. The probability of observing detections in N observations for a given f is:

$$L(d_j|f) = \prod_{j=1}^N (1 - fp_j)^{(1-d_j)} (fp_j)^{d_j} \quad (2)$$

According to Bayes's theorem, the posterior distribution (the probability density of f for a given d_j) is:

$$p(f|d_j) = \frac{L(d_j|f)p(f)}{\int_0^1 L(d_j|f)p(f) df} \quad (3)$$

The likelihood function is the previously calculated $L(d_j|f)$. Since we know little about the prior distribution of the variability occurrence rate f , we used the non-informative Jeffreys prior (Vos et al. 2022):

$$J(f) = \sqrt{\sum_j \frac{p_j}{f(1 - fp_j)}} \quad (4)$$

We calculate $p(f|d_j)$, the probability density function (PDF) of the variability occurrence rate of brown dwarfs using the above equations. We also calculate the 68% and 95% confidence intervals of f with the maximum likelihood following the method used in Kraft et al. (1991) and Vos et al. (2022). If both upper and lower boundaries exist, the confidence interval of credibility α in $[f_{min}, f_{max}]$ is given by:

$$\alpha = \int_{f_{min}}^{f_{max}} p(f|d_j) df; \quad p(f_{min}|d_j) = p(f_{max}|d_j) \quad (5)$$

If only one side boundary can be calculated, the upper or lower boundary is given by:

$$\alpha = \int_{f_{min}}^1 p(f|d_j) df; \quad \text{or } \alpha = \int_0^{f_{max}} p(f|d_j) df \quad (6)$$

7.2 Variability occurrence rates of field and young L and T dwarfs

We calculate the sensitivity map for each observation in our survey. For objects observed multiple times, we use the most sensitive sensitivity map or the one with a positive detection. We obtained sensitivity maps of the objects from Vos et al. (2019). For field objects from Radigan et al. (2014), we are only able to obtain sensitivity

¹ <http://bit.ly/UltracoolSheet>

² https://www.ipac.caltech.edu/2mass/releases/allsky/doc/sec6_4b.html

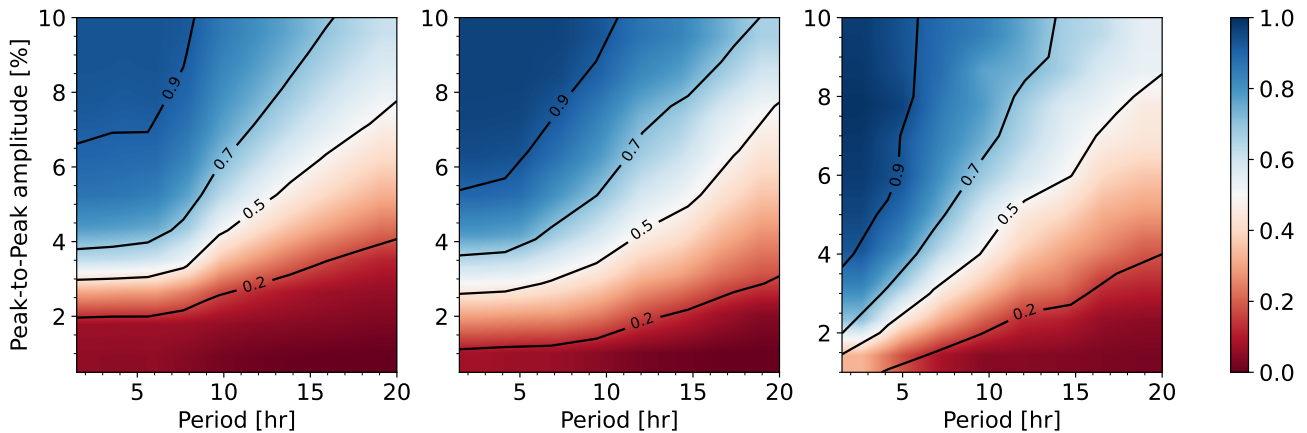


Figure 10. Average sensitivity maps of this survey, Vos2019, and Radigan2014a for objects included in the statistical analysis. The colour represents the retrieval rate. Our objects are fainter than objects in Vos2019 and we also have poorer seeing. Field dwarfs in Radigan2014a are bright and thus they are more sensitive to weak variability.

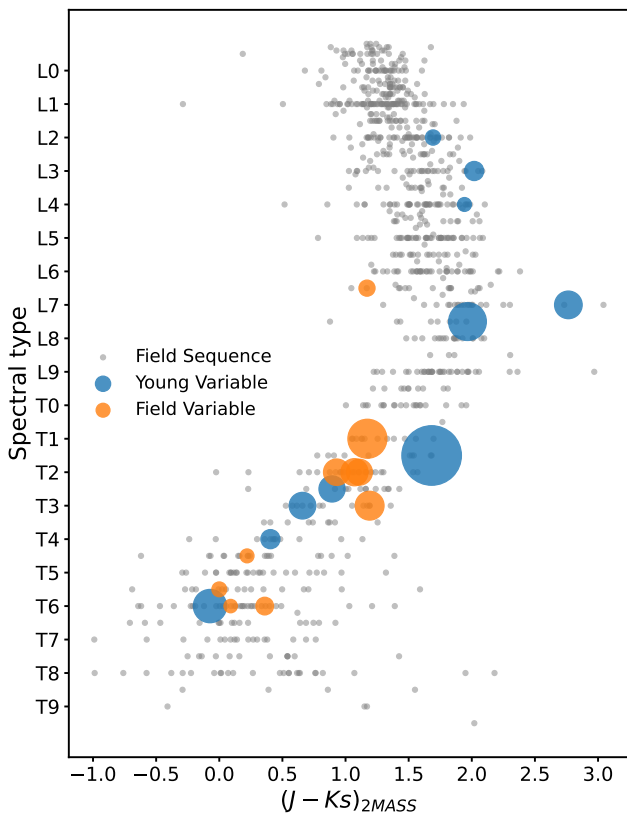


Figure 11. Spectral type against $(J - K_S)_{2MASS}$ colour of variable objects from the four surveys. The grey dots are the field sequence from The UltracoolSheet. The dots in blue and orange represent the variables from the four surveys, with their size proportional to the variability amplitudes.

maps for part of the sample via private communication. For the rest of the objects that have light curves presented in Radigan et al. (2014), we extract these curves and calculate their sensitivity maps using our routine. These give us sensitivity maps of 23 field objects with a good representation of L and T spectral types. We use the average sensitivity map for the corresponding spectral type interval when

calculating f for field objects as a function of spectral type. This is a reasonable approach since Radigan et al. (2014) demonstrate that their survey sensitivity does not vary significantly with spectral type. For objects from Eriksson et al. (2019), we extract the light curves and calculate sensitivity maps for each object.

First, we calculate the total variability rates in the field and young samples with a variability amplitude between 0.5% and 10% and a period between 1.5 and 20 hours. The field sample has a variability rate of $25^{+8}_{-7}\%$ and the young sample has a variability rate of $37^{+11}_{-9}\%$ as shown in Fig. 12. Young L and T objects tend to be more variable than field objects in ground-based near-infrared observations but the difference is not significant as the rates overlap within 1σ . We also calculate the variability rate for L (L0–L9.5) and T (T0–T9.5) spectral types separately as compared in Fig. 13. The field L dwarfs have a variability rate of $6^{+13}_{-5}\%$ while the young L dwarfs have a variability rate of $27^{+13}_{-10}\%$, which is consistent with the previous result reported by Vos et al. (2019). But since the difference in rate is within 1σ , this trend is not significant. We find that young T dwarfs are also more variable than field T dwarfs with a variability rate of $56^{+20}_{-18}\%$ compared with $25^{+8}_{-7}\%$. Though the difference is larger than 1σ , we are cautious about it as the young T sample is small.

In both field and young samples, T dwarfs have a tendency to be more likely to be variable than L dwarfs. We suspect that this may be biased by the L/T transition, which is from L9 to T3.5 and covers more T spectral types than L types. Hence we also calculate the variability rate of field and young dwarfs with spectral types later than L9 and earlier than T3.5. Field T4–T9.5 dwarfs have a variability rate of $17^{+9}_{-7}\%$ which is higher than the rate of $7^{+15}_{-6}\%$ for field L0–L8.5 dwarfs. Young T4–T9.5 dwarfs are also still more likely to be variable than young L0–L8.5 dwarfs, with a variability rate of $44^{+18}_{-22}\%$ and $27^{+13}_{-10}\%$ separately. But these rates overlap significantly within 1σ , therefore whether T dwarfs are more likely to be variable than L dwarfs needs larger samples to refine. Nevertheless, the comparable variability rates of T dwarfs to L dwarfs suggest that clouds are also common in mid-late T spectral types. After the condensation of silicate clouds at the L/T transition, clouds composed of other species can form in the atmospheres of T dwarfs, such as sulfide clouds (Morley et al. 2012). The relatively higher rates in young samples suggest that low surface gravity is more favourable to cloud formation. Our work is from a statistical view. Characterisation of individual objects, such as time-resolved spectroscopy observations

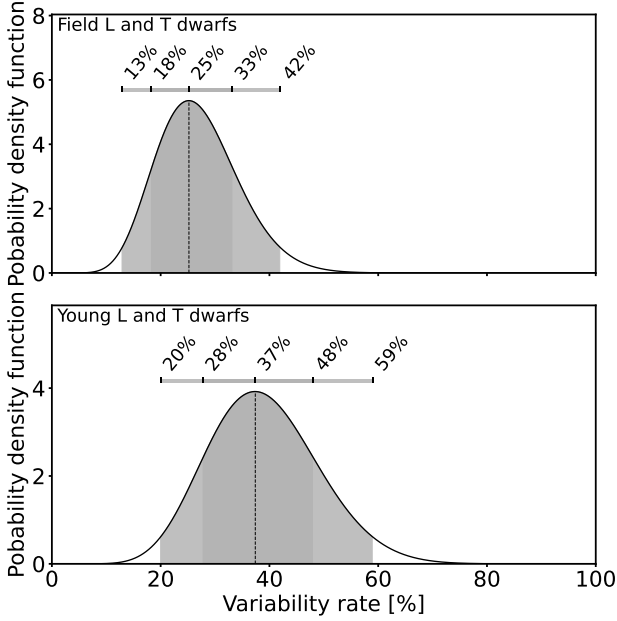


Figure 12. Probability density function of variability rate of the field and young samples. The dark grey area shows the 68% confidence interval and the light grey area shows the 95% confidence interval.

and atmospheric simulations can help study the impact of surface gravity in detail (e.g. Marley et al. 2012; Manjavacas et al. 2014; Filippazzo et al. 2015; Vos et al. 2023).

7.3 Variability occurrence rates at and outside the L/T transition

We also investigate how the variability occurrence rate varies at and outside the L/T transition for field and young samples with a variability amplitude between 0.5% and 10% and a period between 1.5 and 20 hours. While there is no clear definition of the spectral type range of the L/T transition, we adopted the spectral type range of L9–T3.5 used in Radigan et al. (2014) for a fair comparison with their results. This definition is also used in Vos et al. (2022) for their analysis of young object variability at mid-infrared wavelengths. As presented in Fig. 14, for field objects, the variability rate at the L/T transition is higher than that outside the L/T transition, with a value of 36^{+15}_{-13} % and 18^{+9}_{-7} %, respectively. Radigan et al. (2014) also report that strong variables (peak-to-peak amplitudes $> 2\%$) are more frequent at the L/T transition than outside of the L/T transition. This contradicts the variability observations at mid-infrared wavelengths by *Spitzer*. Metchev et al. (2015) report that they did not observe a variability enhancement or stronger amplitudes at the L/T transition, though their sample consists of field and young objects. Vos et al. (2022) separate field and young objects and they find a higher variability rate for field L0–L8.5 dwarfs than field dwarfs at the L/T transition. This indicates that the variability of field dwarfs in the near-infrared and mid-infrared may originate from different sources since different wavelengths probe different heights in atmospheres. *J* band detects a deeper and higher-pressure region, ~ 10 bar, while mid-infrared wavelengths probe lower-pressure layers, ~ 1 bar (Vos et al. 2022). It could also be due to the sensitivity difference between

Table 5. Variability rates of field and young objects in the near-infrared (NIR) and mid-infrared (MIR). The NIR results are from this work for amplitudes of 0.5%–10% and periods of 1.5–20 hr. The MIR results are from Vos2022 for amplitudes of 0.05%–3% and periods of 0.5–40 hr.

Type	L0–L8.5	L9–T3.5	T4–T9.5
Field NIR	7^{+15}_{-6} %	36^{+15}_{-13} %	17^{+9}_{-7} %
Young NIR	27^{+13}_{-10} %	64^{+23}_{-22} %	44^{+28}_{-22} %
Field MIR	83–100%	41^{+23}_{-19} %	18^{+32}_{-15} %
Young MIR	81–100%	85–100%	44–100%

the ground-based observations which detect variability over 1% and the space observations which achieve subpercent sensitivity.

For young objects, we find that variables are also more likely to be located at the L/T transition than outside it, with a variability rate of 64^{+23}_{-22} % and 31^{+12}_{-9} % separately. The large uncertainty of the variability rate at the L/T transition is due to the small sample size. There are only three variables out of eight objects at the L/T transition compared with seven variables out of 37 outside the L/T transition in the young sample. Again, the variability rates of objects at the L/T transition and outside the L/T transitions overlap slightly within 1σ for both field and young samples. This tentative enhancement indicates that the L/T transition has an impact on the near-infrared variability properties of field brown dwarfs and planetary-mass objects.

If we compare variability rates of the three spectral ranges, L0–L8.5, L9–T3.5, and T4–T9.5, we find that the rate is the highest at the L/T transition, then T4–T9.5 and the lowest at L0–L8.5. This trend is the same for field and young objects in the near-infrared. Vos et al. (2022) find that the variability rate is high for young objects from L to T but it drops from L to T for field objects in the mid-infrared for amplitudes of 0.05%–3% and periods of 0.5–40 hr. Table 5 provides the statistical variability rate of field and young objects from this work and Vos et al. (2022). The variability rates of objects with spectral types later than L8.5 are consistent with each other in the near-infrared and mid-infrared for both field and young samples. For L dwarfs (L0–L8.5), there is a big discrepancy in the variability rates between the near-infrared and mid-infrared for both field and young samples. The L dwarfs have a higher variability rate in the mid-infrared but we are cautious about this discrepancy because the mid-infrared observations are from *Spitzer*. These space observations have a much higher sensitivity and much longer observation time than ground-based observations. They could detect weak variables with long periods, thus resulting in higher detection rates.

8 A CENSUS OF VARIABLE OBJECTS

Besides the four surveys discussed in the previous section, there are a few variable brown dwarfs monitored in other surveys or small sample observations (e.g. Buenzli et al. 2014; Metchev et al. 2015; Yang et al. 2015, 2016; Manjavacas et al. 2019a). To gain a comprehensive understanding of the variability in L and T objects, it is necessary to have a census of known variables. Vos et al. (2020) summarise a list of known variables from the literature and we update that list with newly discovered variables and new results from existing variables. They are presented in Table 6. Variability is common in L and T dwarfs from near-infrared to mid-infrared. Since our survey is conducted in the near-infrared, we focus our variability census in the *J* band including ground-based *J* band observations and HST/WFC3/NIR observations using filters in 800–1700 nm.

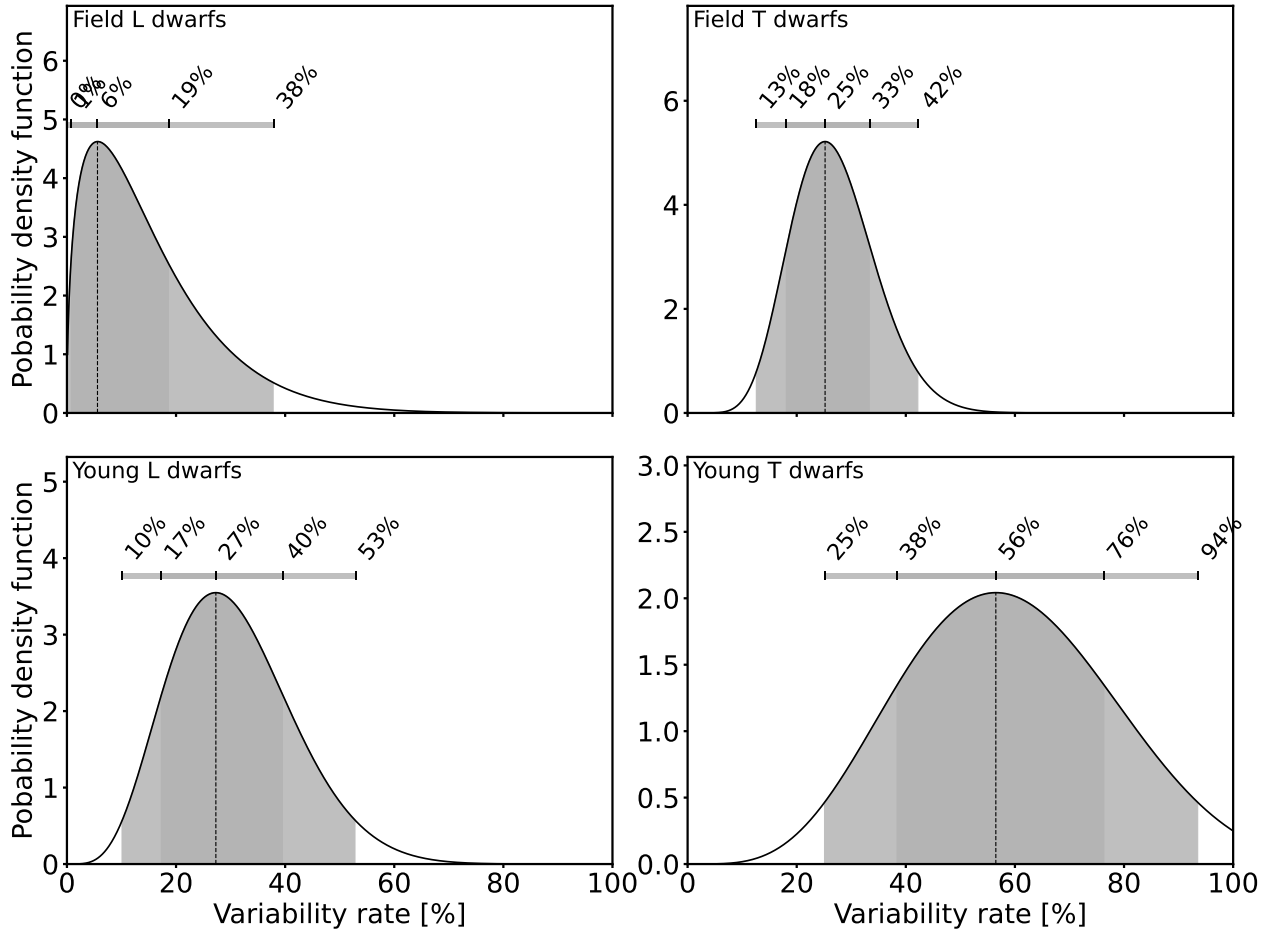


Figure 13. Probability density function of variability rate in the field and young samples for L and T spectral types, respectively. The dark grey area shows the 68% confidence interval and the light grey area shows the 95% confidence interval.

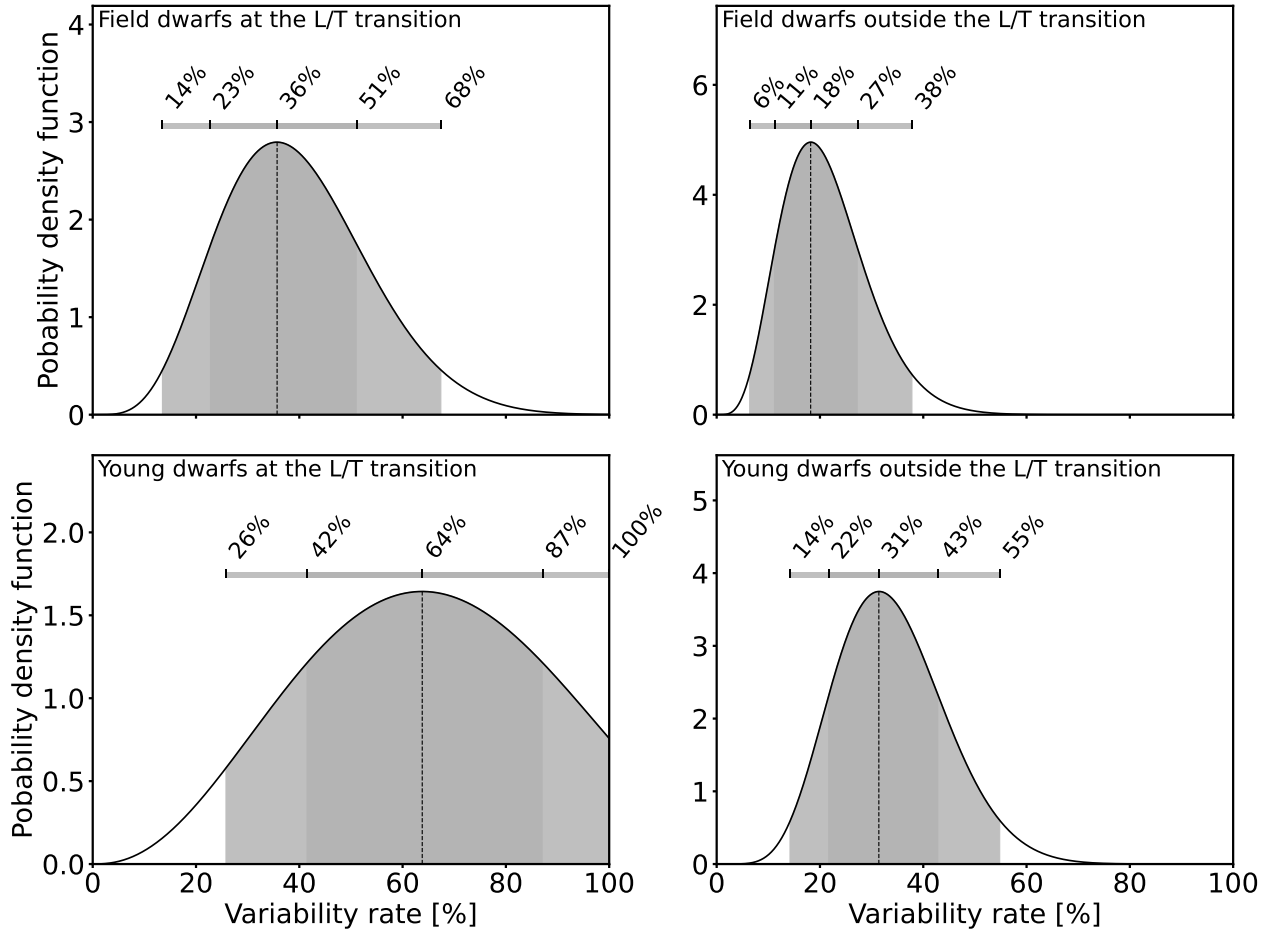


Figure 14. Probability density function of variability rate at the L/T transition and outside the L/T transition for field and young samples. The dark grey area shows the 68% confidence interval and the light grey area shows the 95% confidence interval.

Table 6. Variable brown dwarf detections in the literature. $A_{Jground}$: J band peak-to-peak amplitude measured from ground observations; $A_{WFC3NIR}$: peak-to-peak amplitude measured in the IR channel of HST/Wide Field Camera 3 (WFC3); $A_{3.6}$ and $A_{4.5}$: peak-to-peak amplitude measured in the 3.6 μm and 4.5 μm channels of *Spitzer*.

Target	SpT	$A_{Jground}$ [%]	$A_{WFC3NIR}$ [%]	$A_{3.6}$ [%]	$A_{4.5}$ [%]	Period [hr]	Youth	Companion	Age [Myr]	$v \sin i$ [km s^{-1}]	Variability	ref
2MASS J00011217+1535355	L4	-	-	0.69 ± 0.04	-	15.75 ± 0.37	1	0	120 ± 30	-	1	
2MASS J00132229-1143006	T3 (T3.5+T4.5)	4.6 ± 0.2	-	-	-	-	1	0	45 ± 5	-	2	
2MASSW J0030300-145033	L7	-	-	1.52 ± 0.06	-	4.22 ± 0.02	1	0	45 ± 5	-	1	
2MASS J00310928+5749364	L9	-	-	0.35 ± 0.03	-	1.64 ± 0.01	1	0	200 ± 50	-	1	
LSPM J0036+1821	L3.5	1.22 ± 0.04	-	0.47 ± 0.05	0.19 ± 0.04	2.7 ± 0.3	0	0	1000	36.0 ± 0.2	3, 4	
2MASS J00452143+1634446	L2	1.0 ± 0.1	-	0.18 ± 0.04	0.16 ± 0.04	2.4 ± 0.1	1	0	45 ± 5	$31.76^{+0.22}_{-0.25}$	5, 25	
2MASS J00470038+6803543	L6	-	8.0	1.07 ± 0.04	-	16.4 ± 0.2	1	0	130 ± 20	9.8 ± 0.3	6, 7	
2MASS J00501994-3322402	T7	-	-	<0.59	1.07 ± 0.11	1.55 ± 0.02	0	0	1000	-	3	
2MASSI J0103320+193536	L6	-	-	0.56 ± 0.03	0.87 ± 0.09	2.7 ± 0.1	1	0	300 ± 200	$40.0^{+3.7}_{-4.7}$	3	
2MASS J01075242+0041563	L8	-	-	1.27 ± 0.13	1.0 ± 0.2	5.0 ± 2	0	0	1000	19.4 ± 0.8	3	
GU PSC B	T3.5	4.0	-	-	-	-	1	0	130 ± 20	-	8	
SIMP J013656.57+093347.3	T2.5	5.0	4.5	1.5 ± 0.2	-	2.414 ± 0.078	1	0	200 ± 50	50.9 ± 0.8	9, 10	
2MASS J01383648-0322181	T3	5.5 ± 1.2	-	-	-	-	0	0	1000	-	2	
2MASS J01531463-6744181	L2	-	-	0.48 ± 0.07	-	17.63 ± 1.13	1	0	45 ± 4	-	1	
2MASSW J0310599+164816	L8	-	-	-	-	-	0	0	1000	-	11	
2MASSI J0342162-681732	L4	-	-	0.73 ± 0.07	-	14.73 ± 0.51	1	0	45 ± 4	-	1	
2MASS J03480772-6022270	T7	-	-	-	1.5 ± 0.1	1.08 ± 0.004	0	0	1000	-	12	
2MASS J03492367+0635078	L5	-	-	0.53 ± 0.09	-	14.62 ± 1.08	1	0	45 ± 4	-	1	
2MASS J03552337+1133437	L5	-	-	0.26 ± 0.02	-	9.53 ± 0.19	1	0	130 ± 20	-	1	
2MASS J04070752+1546457	L3.5	-	-	0.36 ± 0.1	-	1.23 ± 0.01	0	0	1000	-	12	
SDSS J042348.57-041403.5	T0	0.8 ± 0.08	-	-	-	2.0 ± 0.4	0	0	1000	68.0 ± 0.9	13	
PSO J071.8769-12.2713	T2	4.5 ± 0.6	-	0.93	-	-	0	0	1000	-	1, 5	
2MASS J05012406-0010452	L3	2.0 ± 1.0	-	0.36 ± 0.04	0.24 ± 0.04	15.7 ± 0.2	1	0	300 ± 200	$9.57^{+0.67}_{-0.58}$	5, 25	
2MASS J05065012+5236338	T4.5	-	-	0.58 ± 0.1	-	13.77 ± 0.82	0	0	2000	-	1	
2MASS J05591914-1404488	T4.5	0.7 ± 0.5	-	-	-	10.0 ± 3	0	0	1000	-	10	
2MASS J06244595-4521548	L6.5	-	1.5	-	-	-	0	0	1000	-	11	
2MASS J06420559+4101599	L9	-	-	2.16 ± 0.16	-	10.11 ± 0.07	1	0	42 ± 6	-	1	
2M0718-6415	T5	-	-	2.14 ± 0.21	-	1.08 ± 0.01	1	0	23 ± 3	-	1	
SDSS J075840.33+324723.4	T2(T0+T3.5)	4.8 ± 0.2	-	-	-	4.9 ± 0.2	0	0	1000	-	10	
2MASS J08095903+4434216	L6	-	-	0.77 ± 0.06	-	1.365 ± 0.004	1	0	300 ± 200	-	1	
DENIS J081730.0-615520	T6	0.6 ± 0.1	-	-	-	2.8 ± 0.2	0	0	1000	-	10	
2MASSI J0825196+211552	L7.5	>1	-	0.81 ± 0.08	1.4 ± 0.3	7.6 ± 5	0	0	1000	-	3	
WISE J085510.83-071442.5	Y0+	-	-	4.0 ± 1.0	4.0 ± 1.0	12.5 ± 3.5	0	0	1000	-	14	
LP261-75B	L6	-	2.4 ± 0.14	-	-	4.78 ± 0.98	0	0	300 ± 50	-	15	
SDSS J104335.08+121314.1	L9	-	-	1.54 ± 0.15	1.2 ± 0.2	3.8 ± 0.2	0	0	1000	-	3	
2MASS J10475385+2124234	T6.5	-	-	-	1.04 ± 0.07	1.741 ± 0.007	0	0	1000	-	16	
WISE 1049B	L7.5+T0.5	-	11.0	-	-	4.87 ± 0.01	0	1	1000	21.6 ± 0.2	17, 18	
SDSS J105213.51+442255.7	T0.5	2.2 ± 0.5	-	-	-	3.0 ± 0.5	0	0	1000	-	17	
DENIS-P J1058.7-1548	L3	0.843 ± 0.098	-	0.39 ± 0.04	<0.3	4.1 ± 0.2	0	0	1000	37.5 ± 2.5	3	
2MASS J11193254-1137466AB	L7	-	-	0.46 ± 0.036	0.96 ± 0.037	3.02 ± 0.04	1	1	10 ± 3	-	19, 20	
2MASS J11263991-5003550	L4.5	1.2 ± 0.1	-	0.21 ± 0.04	0.29 ± 0.15	3.2 ± 0.3	0	0	1000	$22.8^{+1.6}_{-2.4}$	3, 10	
WISEA J114724.10-204021.3	L7	4.6 ± 1.0	-	1.596 ± 0.08	2.216 ± 0.09	19.39 ± 0.3	1	0	10 ± 3	-	19, 20	
2M1207b	L6	-	1.36	-	-	10.7 ± 1	1	0	10 ± 3	-	21	
2MASS J12195156+3128497	L8	-	4.8	0.55 ± 0.13	-	1.14 ± 0.03	0	0	1000	-	11, 12	
VHS1256-1257AB b	L7	>10	38	-	5.76 ± 0.04	22.04 ± 0.05	1	0	225 ± 75	$13.5^{+3.6}_{-4.1}$	22, 23, 24	

Table 6 – *continued* Variable brown dwarfs detections in the literature. $A_{Jground}$: J band peak-to-peak amplitude measured from ground observations; $A_{WFC3NIR}$: peak-to-peak amplitude measured in the IR channel of HST/Wide Field Camera 3 (WFC3); $A_{3.6}$ and $A_{4.5}$: peak-to-peak amplitude measured in the $3.6\ \mu\text{m}$ and $4.5\ \mu\text{m}$ channels of *Spitzer*.

Target	SpT	$A_{Jground}$ [%]	$A_{WFC3NIR}$ [%]	$A_{3.6}$ [%]	$A_{4.5}$ [%]	Period [hr]	Youth	Companion	Age [Myr]	$v_{\text{ sini}}$ [km s^{-1}]	Variability ref
Ross 458C	T8	-	2.62 ± 0.02	<1.37	<0.72	6.75 ± 1.58	1	0	125 ± 75	-	3
2MASS J13243559+6358284	T2.5	-	-	3.05 ± 0.15	3.0 ± 0.3	13.0 ± 1	1	0	130 ± 20	-	3
WISE J140518.39+553421.3	Y0.5	-	-	3.6 ± 0.4	3.54 ± 0.09	8.2 ± 0.3	0	0	1000	-	26
2MASS J14252798-3650229	L4	0.7 ± 0.3	-	<0.16	<0.18	-	1	0	130 ± 20	$33.08^{+0.53}_{-0.49}$	25, 25
2MASSW J1507476-162738	L5	-	0.7	0.53 ± 0.11	0.45 ± 0.09	2.5 ± 0.1	0	0	1000	19.1 ± 0.5	3, 9
SDSS J151114.66+060742.9	L5.5+T5.0	-	-	0.67 ± 0.07	<0.49	11.0 ± 2	0	1	1000	-	3
SDSS J151643.01+305344.4	T0.5	-	-	2.4 ± 0.2	1.3 ± 0.7	6.7 ± 5	0	0	1000	-	3
2MASS J16154255+4953211	L4	-	-	0.9 ± 0.2	<0.39	24.0 ± 5	1	0	300 ± 200	$9.5^{+1.3}_{-1.2}$	3
2MASS J16291840+0335371	T2	4.3 ± 2.4	-	-	-	6.9 ± 2.4	0	0	1000	$19.7^{+0.7}_{-0.8}$	10
2MASSW J1632291+190441	L8	-	-	0.42 ± 0.08	0.5 ± 0.3	3.9 ± 0.2	0	0	1000	-	3
2MASS J16471580+5632057	L7	-	-	0.468 ± 0.06	-	9.234 ± 0.25	1	0	300 ± 200	-	1
2MASSI J1721039+334415	L3	-	-	0.33 ± 0.07	<0.29	2.6 ± 0.1	0	0	1000	21.5 ± 0.3	3
WISEP J173835.52+273258.9	Y0	-	-	-	3.0 ± 0.1	6.0 ± 0.1	0	0	1000	-	27
2MASS J17410280-4642218	L7	-	-	0.35 ± 0.03	-	15.0 ± 0.71	1	0	130 ± 20	-	1
2MASS J17502484-0016151	L5	>1	-	-	-	-	0	0	1000	-	11
2MASS J17503293+1759042	T3.5	>1	-	-	-	-	0	0	1000	-	11
2MASS J17534518-6559559	L4	-	-	<0.25	-	-	0	0	1000	-	3
2MASS J18212815+1414010	L4.5	-	2.5	0.54 ± 0.05	0.71 ± 0.14	4.2 ± 0.1	0	0	1000	30.7 ± 0.2	3, 9
2MASS J18283572-4849046	T5.5	0.9 ± 0.1	-	-	-	5.0 ± 0.6	0	0	1000	-	10
2MASS J20025073-0521524	L5	1.7 ± 0.2	-	0.28	-	-	1	0	300 ± 200	-	1
PSO 318.5-22	L7.5	10.0 ± 1.3	-	-	3.4 ± 0.08	8.61 ± 0.06	1	0	22 ± 6	$17.5^{+2.3}_{-2.8}$	5, 28, 29,
HD 203030B	L7.5	-	1.1 ± 0.3	-	-	7.5 ± 0.6	1	0	90 ± 60	-	30
2MASS J21392676+0220226	T1.5	26	27	11.0 ± 1.0	10.0 ± 1.0	7.618 ± 0.18	1	0	200 ± 50	18.7 ± 0.3	9, 11, 31
HN PegB	T2.5	-	1.2	0.77 ± 0.15	1.1 ± 0.5	15.4 ± 0.5	1	0	237 ± 33	-	3
2MASS J21481628+4003593	L6	-	-	1.33 ± 0.07	1.03 ± 0.1	19.0 ± 4	0	1	300 ± 200	$9.2^{+0.4}_{-0.3}$	3
2MASS J22062520+3301144	T1.5	-	-	1.2 ± 0.13	-	15.91 ± 0.62	1	0	45 ± 5	-	1
2MASSW J2208136+292121	L3	-	-	0.69 ± 0.07	0.54 ± 0.11	3.5 ± 0.2	1	0	22 ± 6	$40.6^{+1.3}_{-1.4}$	3
2MASS J22153705+2110554	T1 (T0+T2)	10.7 ± 0.4	-	-	-	5.2 ± 0.5	0	0	1000	-	2
2MASS J22282889-4310262	T6	1.6 ± 0.3	5.3	4.6 ± 0.2	1.51 ± 0.15	1.41 ± 0.01	0	0	1000	-	3, 10, 32
2MASS J2244316+204343	L6	5.5 ± 0.6	-	0.8 ± 0.2	-	11.0 ± 2	1	0	130 ± 20	$14.3^{+1.4}_{-1.5}$	5, 7, 33
WISEPAJ081958.05-033529.0	T4	2.0 ± 0.7	-	-	2.0 ± 0.7	-	1	0	22 ± 6	-	20
2MASSIJ1553022+153236	T7	1.1 ± 0.2	-	-	-	-	1	1	200 ± 50	-	20
CFBDS J232304.41-015232.3	T6	7.6	-	-	-	-	1	0	22 ± 6	-	20

Variability references: (1) Vos et al. (2022); (2) Eriksson et al. (2019); (3) Metchev et al. (2015); (4) Croll et al. (2016); (5) Vos et al. (2019); (6) Lew et al. (2016); (7) Vos et al. (2018); (8) Naud et al. (2017); (9) Yang et al. (2016); (10) Radigan et al. (2014); (11) Buenzli et al. (2014); (12) Tannock et al. (2021); (13) Clarke et al. (2008); (14) Esplin et al. (2016); (15) Manjavacas et al. (2018); (16) Allers et al. (2020); (17) Girardin et al. (2013); (18) Buenzli et al. (2015); (19) Schneider et al. (2018); (20) This work; (21) Zhou et al. (2016); (22) Zhou et al. (2020); (23) Zhou et al. (2022); (24) Bowler et al. (2020); (25) Vos et al. (2020); (26) Cushing et al. (2016); (27) Leggett et al. (2016); (28) Allers et al. (2016); (29) Biller et al. (2018); (30) Miles-Páez et al. (2019); (31) Apai et al. (2017); (32) Buenzli et al. (2012); (33) Morales-Calderón et al. (2006)

The spectral type distribution of known variables in the J band is illustrated in Fig. 15. Variability is observed across a wide range of spectral types in field brown dwarfs and an even wider range in young objects. Field objects exhibit variability from L3 to T6, with a weak peak around T2–T2.5. Meanwhile, young variable objects have a range of spectral types from L2 to T8, with a peak at L6–L7.5. Figure. 16 shows the maximum peak-to-peak amplitudes of these objects versus their spectral types. Strong field variables with an amplitude $> \sim 2\%$ tend to assemble from L8 to T3, with three exceptions having spectral types L4.5, L6, and T6, respectively. The strongest field variable is a T1 object, 2MASS J2215+2110, with an amplitude of $10.7 \pm 0.4\%$ measured by Eriksson et al. (2019). Strong young variables tend to assemble in L6–T3.5, though the latest spectral type of strong young variables can be T8. The two strongest variables in Fig. 16 are young objects. The L7 young object, VHS 1256-1257b, has a recorded largest variability amplitude of 38% in the J band measured by Zhou et al. (2022). The second-strongest young variable is a T1.5 object, 2MASS J2139+0220, with an amplitude of 26% in the J band measured by Radigan et al. (2012).

While young objects also show strong variability at the L/T transition as field objects, young objects have even stronger variability in the spectral range of L6–L7.5. In this narrow spectral range, there are at least five of the known strongest variables, including the one with the known maximum variability. They are VHS 1256-1257b (L7) with an amplitude of 38% (Zhou et al. 2022), PSO 318.5-22 (L7.5) with an amplitude of 10% (Vos et al. 2019), 2MASS J00470038+6803543 (L6) with an amplitude of 8% (Lew et al. 2016), 2MASS J2244316+204343 (L6) with an amplitude of 5.5% (Vos et al. 2019) and WISEA J114724.10-204021.3 (L7) with an amplitude of 4.6% (this work). These objects have extremely red $J - K$ colours, indicating that they have thicker clouds than field dwarfs. If we posit the patchy clouds scenario with thick and thin cloud patches (Marley et al. 2010; Apai et al. 2013), a break-up in thicker clouds could result in higher contrast and thus stronger variability in light curves. Filippazzo et al. (2015) find that low gravity L dwarfs have a cooler T_{eff} than field L dwarfs of the same spectral type, with a difference of up to 300 K. This implies that the start of cloud condensation in young L dwarfs may occur at an earlier spectral type than field L dwarfs if we assume that the cloud condensation occurs at a certain T_{eff} . However, Marley et al. (2012) suggest that the L/T transition of low gravity objects occurs at a lower T_{eff} range than that of field dwarfs. Therefore, what drives the extreme variability of young L dwarfs in this spectral range is still unclear and needs more observations and atmospheric models to study.

9 COLOUR OF YOUNG L AND T OBJECTS

The sample of young L dwarfs are redder in the near-infrared compared to their field counterparts, as noted in previous studies (e.g. Liu et al. 2016; Faherty et al. 2016), while the young T dwarfs do not have this reddening trend. This agrees with the prevailing scenario that young L dwarfs tend to have thicker clouds than field L dwarfs, and these silicate clouds condense below the photosphere in T dwarfs. We compare the 2MASS $J - K_S$ colour of all the known young T dwarfs and suspect that later T types gradually become bluer than their field dwarf counterparts from T4 to T7 in Fig. 17. With $J - K$ MKO colours versus spectral types, Zhang et al. (2021) also mention that earlier T are redder than their field dwarf counterparts but this trend vanishes in later spectral types. We fit a line to young L and T dwarfs respectively and calculate the root mean square distance (rms) of the young and field samples to the fitting. Young L

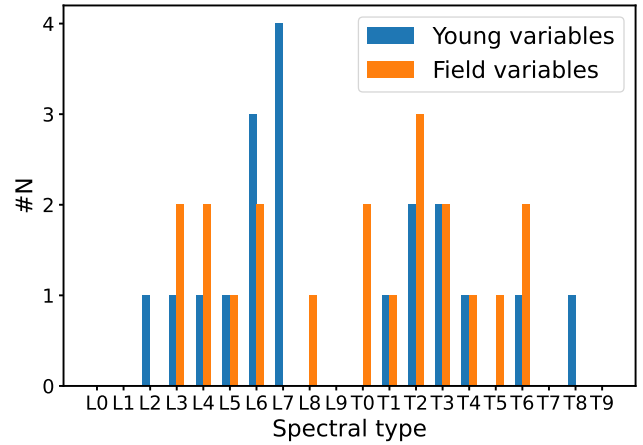


Figure 15. Spectral type distribution of known young and field variables in the J band from the literature.

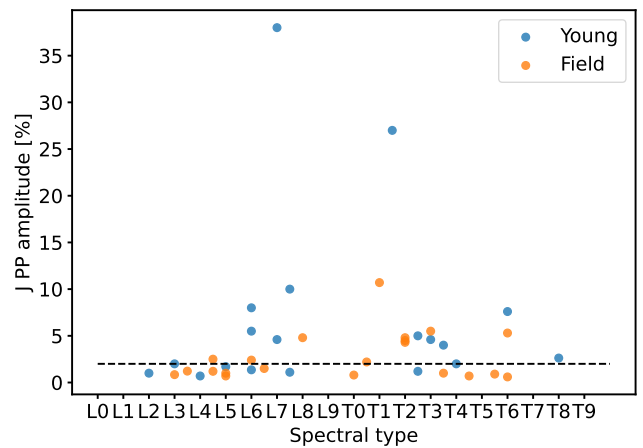


Figure 16. Peak-to-peak amplitude in the J band versus spectral type of known young and field variables from the literature. Variables with amplitudes $> \sim 2\%$ are strong variables and are above the dashed line. Young strong variables span from L6 to T3.5, while field strong variables span in a narrower range, from L8 to T3. Furthermore, young objects have the strongest amplitudes.

dwarfs have a rms of 1.40 while field L dwarfs have a rms of 3.00. Young T dwarfs have a rms of 1.11 while field T dwarfs have a rms of 2.04. Since the difference in T spectral types is not as significant as it is in L spectral types for field and young dwarfs, we are cautious about this slight bluing trend in T spectral types as it could be biased by the small number of objects known to date. Future detections of more young objects in this range are needed to confirm it. The colours of young objects from T1.5 to T4 fall within a similar range as their field counterparts. The absence of young objects between L8 and T1 hinders the understanding of how the colour of young objects changes at this critical spectral range, for example, where the young objects reach their reddest point.

It is worth noticing that the colour of variable brown dwarfs is also related to their inclination angle. Vos et al. (2017) find a positive correlation between the inclination angle and the $J - K_S$ colour of variable brown dwarfs, which suggests that there are thicker or larger-

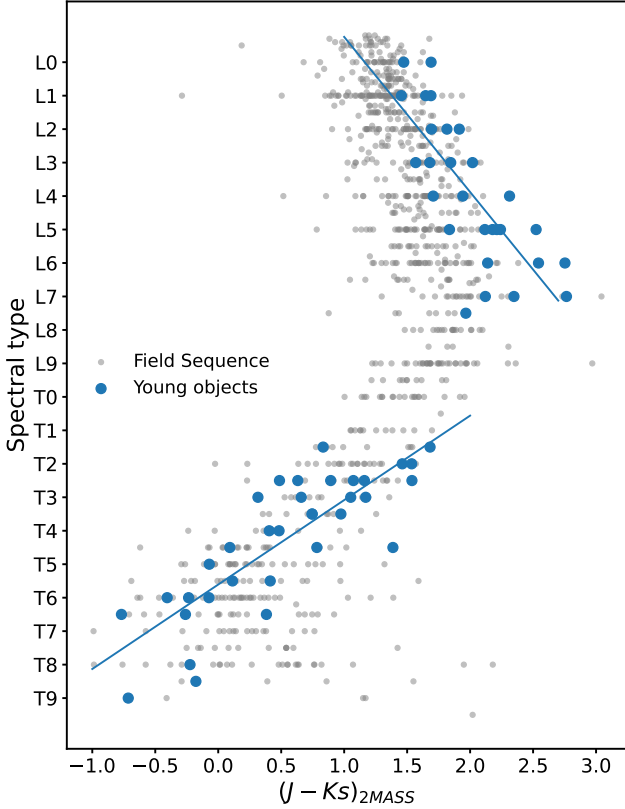


Figure 17. Spectral type and colour plot of young objects. The young L dwarfs have redder colour than the field dwarfs, while young T dwarfs do not have this reddening trend and even become slightly bluer from T4 to T7. Blue lines are a linear fit to young L and T dwarfs, respectively.

grained clouds at the equator than at the poles. Suarez et al. (2023) support this by finding a positive correlation between the inclination angle and silicate absorption index. To measure the inclination angle, we need to measure the $v\sin i$ from the high-resolution spectra of our objects. However since our objects are mainly young T-type planetary mass objects, most of them are fainter than 16.5 magnitudes in the J band, which makes it difficult to obtain high S/N spectroscopic observations under reasonable integration time with telescopes such as VLT. Future telescopes such as E-ELT can achieve $v\sin i$ measurements of these objects with high S/N, which can also place an upper limit on the rotation period of our objects. Combined with the period from variability observations which is the lower limit for objects detected with long-term variability, the rotation period of the variable objects and their inclination angle can be constrained.

10 CONCLUSIONS

We report a near-infrared survey for photometric variability in young planetary-mass objects, including the largest sample of young T dwarfs monitored to date. We conduct continuous J_S - or K_S -band monitoring of 18 objects, with observation time ranging from 1.5 to 7.5 hours per object. One variable 2M1119-1137AB is an unresolved binary. We detected variability in four variables with significance higher than 99%, as well as two variable candidates. The shortest period found among the other three variables is 5.5 ± 0.2 hours, consistent with the trend that young objects have longer rotation periods

than field objects, which is due to angular momentum conservation during contraction (Schneider et al. 2018).

We combine our survey with three previous J -band photometric variability surveys of field L and T objects and young low gravity L objects, comprising a total number of 108 objects. From the statistical calculation, we find that young dwarfs have a tendency to be more variable than field dwarfs within peak-to-peak variability amplitude ranges of 0.5%–10% and period ranges of 1.5–20 hr. The variability rate of young L dwarfs is $27^{+13}_{-10}\%$ compared to $6^{+13}_{-5}\%$ for field L dwarfs, consistent with the previous result reported by Vos et al. (2019). We constrain the near-infrared variability rate of young T dwarfs for the first time. Young T dwarfs have a variability rate of $56^{+20}_{-18}\%$ compared to $25^{+8}_{-7}\%$ for field T dwarfs. Both young L and T samples tend to be more variable than their field dwarf counterparts, which are of $\sim 1\sigma$ difference. Moreover, both young and field samples also tend to be more variable at the L/T transition than objects outside the L/T transition, suggesting the strong impact of the L/T transition on atmospheric structures. The variability rate of field objects is $36^{+15}_{-13}\%$ at the L/T transition compared to $18^{+9}_{-7}\%$ outside the L/T transition. The variability rate of young objects is $64^{+23}_{-22}\%$ at the L/T transition compared to $31^{+12}_{-9}\%$ outside the L/T transition. Besides the L/T transition, our analysis of known variables in the J band in the literature finds that young low gravity L dwarfs with high variability amplitudes tend to congregate in a narrow spectral range of L6–L7.5, while field L dwarfs do not have this trend.

This study once again demonstrates that young dwarfs and field dwarfs are likely distinct groups with differing variability properties at least in terms of strong variability ($> \sim 1\%$), with surface gravity playing a crucial role in the variability of brown dwarfs for both L-type and T-type dwarfs. Future multi-wavelength time-resolved observations with JWST, along with atmospheric modelling, will enable a deep understanding of how gravity impacts atmospheric structures of L and T dwarfs, and will also be critical for understanding the atmospheres of directly imaged exoplanets, which are similar to young low gravity dwarfs.

ACKNOWLEDGEMENTS

Based on observations collected at the European Organisation for Astronomical Research in the Southern Hemisphere under ESO programmes 108.2256, 109.22XF, 110.23Y0, and 111.24LQ. B.B acknowledges funding by the UK Science and Technology Facilities Council (STFC) grant no. ST/M001229/1. J. M. V. acknowledges support from a Royal Society - Science Foundation Ireland University Research Fellowship (URF\1\221932). This research made use of ASTROPY, a community-developed core PYTHON package for Astronomy (Astropy Collaboration et al. 2013, 2018), SCIPY (Virtanen et al. 2020), NUMPY (Harris et al. 2020) and MATPLOTLIB, a Python library for publication quality graphics (Hunter 2007).

DATA AVAILABILITY

The raw data of our observations can be accessed via ESO Science Archive Facility.

REFERENCES

Albert L., Artigau É., Delorme P., Reyrol C., Forveille T., Delfosse X., Willott C. J., 2011, *AJ*, **141**, 203

- Allers K. N., Liu M. C., 2013, *ApJ*, **772**, 79
- Allers K. N., Gallimore J. F., Liu M. C., Dupuy T. J., 2016, *ApJ*, **819**, 133
- Allers K. N., Vos J. M., Biller B. A., Williams P. K. G., 2020, *Science*, **368**, 169
- Apai D., Radigan J., Buenzli E., Burrows A., Reid I. N., Jayawardhana R., 2013, *ApJ*, **768**, 121
- Apai D., et al., 2017, *Science*, **357**, 683
- Artigau É., Bouchard S., Doyon R., Lafrenière D., 2009, *ApJ*, **701**, 1534
- Astropy Collaboration et al., 2013, *A&A*, **558**, A33
- Astropy Collaboration et al., 2018, *AJ*, **156**, 123
- Barman T. S., Macintosh B., Konopacky Q. M., Marois C., 2011a, *ApJ*, **733**, 65
- Barman T. S., Macintosh B., Konopacky Q. M., Marois C., 2011b, *ApJ*, **735**, L39
- Bell C. P. M., Mamajek E. E., Naylor T., 2015, *MNRAS*, **454**, 593
- Best W. M. J., et al., 2015, *ApJ*, **814**, 118
- Best W. M. J., Liu M. C., Dupuy T. J., Magnier E. A., 2017, *ApJ*, **843**, L4
- Best W. M. J., Liu M. C., Magnier E. A., Dupuy T. J., 2020, *AJ*, **159**, 257
- Biller B. A., et al., 2015, *ApJ*, **813**, L23
- Biller B. A., et al., 2018, *AJ*, **155**, 95
- Bonavita M., de Mooij E. J. W., Jayawardhana R., 2013, *PASP*, **125**, 849
- Bouy H., et al., 2022, *A&A*, **664**, A111
- Bowler B. P., Blunt S. C., Nielsen E. L., 2020, *AJ*, **159**, 63
- Buenzli E., et al., 2012, *ApJ*, **760**, L31
- Buenzli E., Apai D., Radigan J., Reid I. N., Flateau D., 2014, *ApJ*, **782**, 77
- Buenzli E., Saumon D., Marley M. S., Apai D., Radigan J., Bedin L. R., Reid I. N., Morley C. V., 2015, *ApJ*, **798**, 127
- Burgasser A. J., Kirkpatrick J. D., Brown M. E., 2002, in *American Astronomical Society Meeting Abstracts #200*. p. 11.05
- Burgasser A. J., Kirkpatrick J. D., Cruz K. L., Reid I. N., Leggett S. K., Liebert J., Burrows A., Brown M. E., 2006, *ApJS*, **166**, 585
- Burgasser A. J., et al., 2014, *ApJ*, **785**, 48
- Burningham B., et al., 2013, *MNRAS*, **433**, 457
- Burrows A., Sharp C. M., 1999, *ApJ*, **512**, 843
- Burrows A., Sudarsky D., Hubeny I., 2006, *ApJ*, **640**, 1063
- Clarke F. J., Hodgkin S. T., Oppenheimer B. R., Robertson J., Haubois X., 2008, *MNRAS*, **386**, 2009
- Croll B., Muirhead P. S., Lichtman J., Han E., Dalba P. A., Radigan J., 2016, *arXiv e-prints*, p. [arXiv:1609.03587](https://arxiv.org/abs/1609.03587)
- Cushing M. C., et al., 2008, *ApJ*, **678**, 1372
- Cushing M. C., et al., 2016, *ApJ*, **823**, 152
- Dupuy T. J., Liu M. C., 2012, *ApJS*, **201**, 19
- Eriksson S. C., Janson M., Calissendorff P., 2019, *A&A*, **629**, A145
- Esplin T. L., Luhman K. L., Cushing M. C., Hardegree-Ullman K. K., Trucks J. L., Burgasser A. J., Schneider A. C., 2016, *ApJ*, **832**, 58
- Faherty J. K., et al., 2016, *ApJS*, **225**, 10
- Filippazzo J. C., Rice E. L., Faherty J., Cruz K. L., Van Gordon M. M.,Looper D. L., 2015, *ApJ*, **810**, 158
- Gagné J., et al., 2015, *ApJS*, **219**, 33
- Gagné J., et al., 2017a, *ApJS*, **228**, 18
- Gagné J., et al., 2017b, *ApJ*, **841**, L1
- Gagné J., Allers K. N., Theissen C. A., Faherty J. K., Bardalez Gagliuffi D., Artigau É., 2018, *ApJ*, **854**, L27
- Girardin F., Artigau É., Doyon R., 2013, *ApJ*, **767**, 61
- Golimowski D. A., et al., 2004, *AJ*, **127**, 3516
- Harris C. R., et al., 2020, *Nature*, **585**, 357
- Hunter J. D., 2007, *Computing In Science & Engineering*, **9**, 90
- Kellogg K., Metchev S., Geißler K., Hicks S., Kirkpatrick J. D., Kurtev R., 2015, *AJ*, **150**, 182
- Kellogg K., Metchev S., Gagné J., Faherty J., 2016, *ApJ*, **821**, L15
- Kirkpatrick J. D., 2005, *ARA&A*, **43**, 195
- Knapp G. R., et al., 2004, *AJ*, **127**, 3553
- Koen C., Matsunaga N., Menzies J., 2004, *MNRAS*, **354**, 466
- Koen C., Tanabé T., Tamura M., Kusakabe N., 2005, *MNRAS*, **362**, 727
- Kraft R. P., Burrows D. N., Nousek J. A., 1991, *ApJ*, **374**, 344
- Lafrenière D., et al., 2007, *ApJ*, **670**, 1367
- Leggett S. K., et al., 2016, *ApJ*, **830**, 141
- Lew B. W. P., et al., 2016, *ApJ*, **829**, L32
- Limbach M. A., Vos J. M., Winn J. N., Heller R., Mason J. C., Schneider A. C., Dai F., 2021, *ApJ*, **918**, L25
- Liu M. C., et al., 2013, *ApJ*, **777**, L20
- Liu M. C., Dupuy T. J., Allers K. N., 2016, *ApJ*, **833**, 96
- Lodders K., 1999, *ApJ*, **519**, 793
- Lomb N. R., 1976, *Ap&SS*, **39**, 447
- Lucas P. W., Roche P. F., 2000, *MNRAS*, **314**, 858
- Lucas P. W., Roche P. F., Allard F., Hauschildt P. H., 2001, *MNRAS*, **326**, 695
- Manjavacas E., et al., 2014, *A&A*, **564**, A55
- Manjavacas E., et al., 2018, *AJ*, **155**, 11
- Manjavacas E., et al., 2019a, *AJ*, **157**, 101
- Manjavacas E., et al., 2019b, *ApJ*, **875**, L15
- Marley M. S., Saumon D., Goldblatt C., 2010, *ApJ*, **723**, L117
- Marley M. S., Saumon D., Cushing M., Ackerman A. S., Fortney J. J., Freedman R., 2012, *ApJ*, **754**, 135
- Marocco F., et al., 2021, *ApJS*, **253**, 8
- Martín E. L., Zapatero Osorio M. R., Lehto H. J., 2001, *ApJ*, **557**, 822
- Metchev S. A., et al., 2015, *ApJ*, **799**, 154
- Miles-Pérez P. A., et al., 2019, *ApJ*, **883**, 181
- Miret-Roig N., et al., 2022, *Nature Astronomy*, **6**, 89
- Moore K., Scholz A., Jayawardhana R., 2019, *ApJ*, **872**, 159
- Moorwood A., Cuby J. G., Lidman C., 1998, *The Messenger*, **91**, 9
- Morales-Calderón M., et al., 2006, *ApJ*, **653**, 1454
- Morley C. V., Fortney J. J., Marley M. S., Visscher C., Saumon D., Leggett S. K., 2012, *ApJ*, **756**, 172
- Morley C. V., Marley M. S., Fortney J. J., Lupu R., 2014, *ApJ*, **789**, L14
- Mortier A., Faria J. P., Correia C. M., Santerne A., Santos N. C., 2015, *BGLS: A Bayesian formalism for the generalised Lomb-Scargle periodogram* (ascl:1504.020)
- Naud M.-E., Artigau É., Rowe J. F., Doyon R., Malo L., Albert L., Gagné J., Bouchard S., 2017, *AJ*, **154**, 138
- Oasa Y., Tamura M., Sugitani K., 1999, *ApJ*, **526**, 336
- Radigan J., 2014, *ApJ*, **797**, 120
- Radigan J., Jayawardhana R., Lafrenière D., Artigau É., Marley M., Saumon D., 2012, *ApJ*, **750**, 105
- Radigan J., Lafrenière D., Jayawardhana R., Artigau E., 2014, *ApJ*, **793**, 75
- Scargle J. D., 1982, *ApJ*, **263**, 835
- Schneider A. C., Windsor J., Cushing M. C., Kirkpatrick J. D., Wright E. L., 2016, *ApJ*, **822**, L1
- Schneider A. C., Windsor J., Cushing M. C., Kirkpatrick J. D., Shkolnik E. L., 2017, *AJ*, **153**, 196
- Schneider A. C., Hardegree-Ullman K. K., Cushing M. C., Kirkpatrick J. D., Shkolnik E. L., 2018, *AJ*, **155**, 238
- Scholz A., Moore K., Jayawardhana R., Aigrain S., Peterson D., Stelzer B., 2018, *ApJ*, **859**, 153
- Shkolnik E. L., Allers K. N., Kraus A. L., Liu M. C., Flagg L., 2017, *AJ*, **154**, 69
- Skrzypczek N., Warren S. J., Faherty J. K., 2016, *A&A*, **589**, A49
- Stephens D. C., et al., 2009, *ApJ*, **702**, 154
- Suarez G., Vos J. M., Metchev S., Faherty J. K., Cruz K., 2023, *arXiv e-prints*, p. [arXiv:2308.02093](https://arxiv.org/abs/2308.02093)
- Tannock M. E., et al., 2021, *AJ*, **161**, 224
- Tsuji T., Nakajima T., 2003, *ApJ*, **585**, L151
- Tsuji T., Ohnaka K., Aoki W., Nakajima T., 1996, *A&A*, **308**, L29
- VanderPlas J. T., 2018, *ApJS*, **236**, 16
- Virtanen P., et al., 2020, *Nature Methods*, **17**, 261
- Vos J. M., Allers K. N., Biller B. A., 2017, *ApJ*, **842**, 78
- Vos J. M., Allers K. N., Biller B. A., Liu M. C., Dupuy T. J., Gallimore J. F., Adenuga I. J., Best W. M. J., 2018, *MNRAS*, **474**, 1041
- Vos J. M., et al., 2019, *MNRAS*, **483**, 480
- Vos J. M., et al., 2020, *AJ*, **160**, 38
- Vos J. M., Faherty J. K., Gagné J., Marley M., Metchev S., Gizis J., Rice E. L., Cruz K., 2022, *ApJ*, **924**, 68
- Vos J. M., et al., 2023, *ApJ*, **944**, 138
- Wilson P. A., Rajan A., Patience J., 2014, *A&A*, **566**, A111
- Yang H., et al., 2015, *ApJ*, **798**, L13
- Yang H., et al., 2016, *ApJ*, **826**, 8

- Zapatero Osorio M. R., Béjar V. J. S., Martín E. L., Rebolo R., Barrado y Navascués D., Bailer-Jones C. A. L., Mundt R., 2000, *Science*, **290**, 103
- Zapatero Osorio M. R., Caballero J., Martín E. L., Béjar V. J. S., Rebolo R., 2004, *Ap&SS*, **292**, 673
- Zhang Z., Liu M. C., Best W. M. J., Dupuy T. J., Siverd R. J., 2021, *ApJ*, **911**, 7
- Zhou Y., Apai D., Schneider G. H., Marley M. S., Showman A. P., 2016, *ApJ*, **818**, 176
- Zhou Y., Bowler B. P., Morley C. V., Apai D., Kataria T., Bryan M. L., Benneke B., 2020, *AJ*, **160**, 77
- Zhou Y., Bowler B. P., Apai D., Kataria T., Morley C. V., Bryan M. L., Skemer A. J., Benneke B., 2022, *AJ*, **164**, 239
- Zuckerman B., 2019, *ApJ*, **870**, 27
- Zuckerman B., Bessell M. S., Song I., Kim S., 2006, *ApJ*, **649**, L115

APPENDIX A: REFERENCE STARS AND MAD-MAGNITUDE PLOTS

We show the target and selected reference stars of all observations, including the MAD and instrumental magnitude relationship plots. If not specified, observations are in the J_S band.

APPENDIX B: POTENTIALLY VARIABLE LIGHT CURVES

Potentially variable light curves, periodograms, and sensitivity plots.

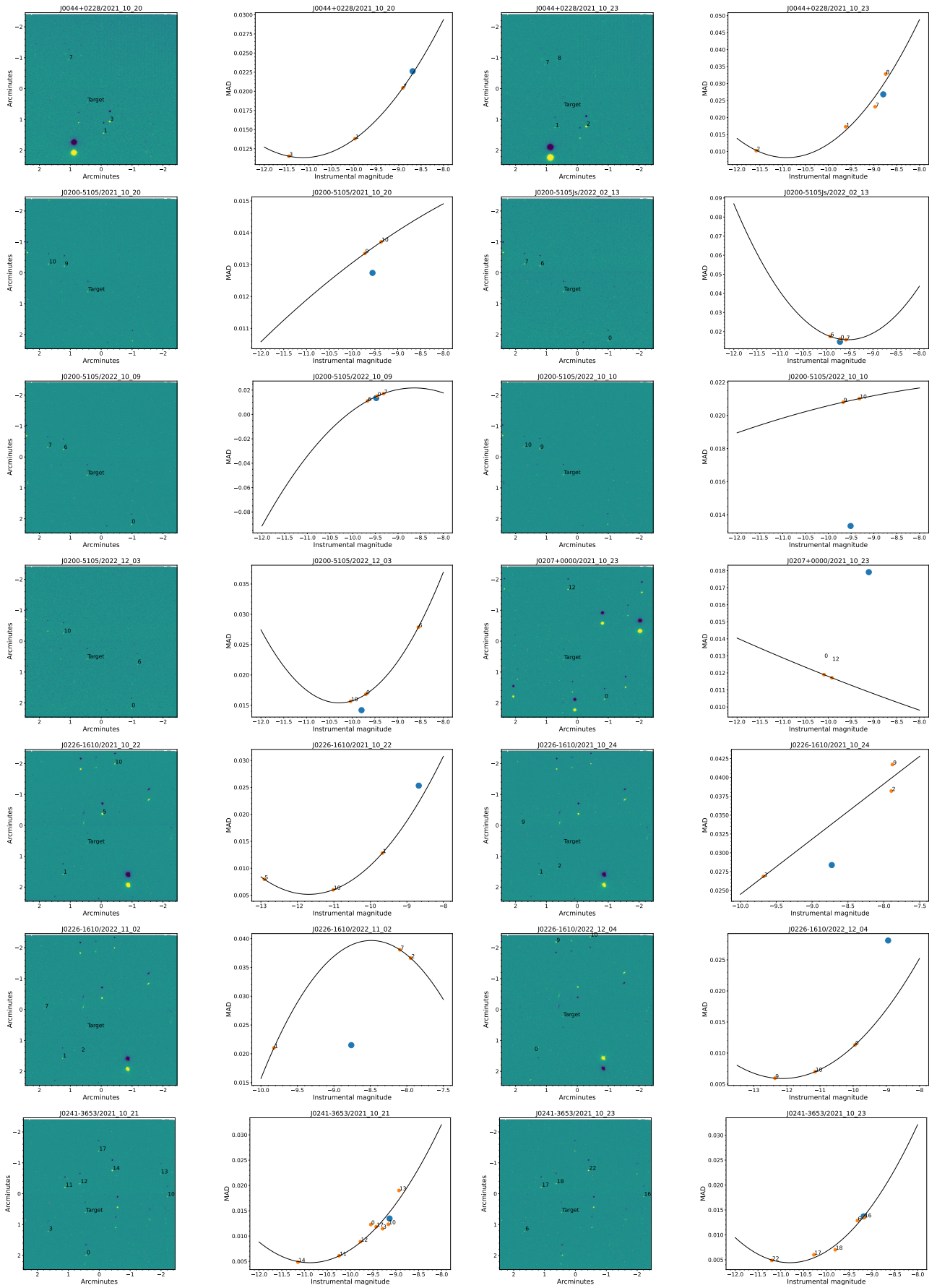


Figure A1. Targets and their selected reference stars. North is left and east is down.

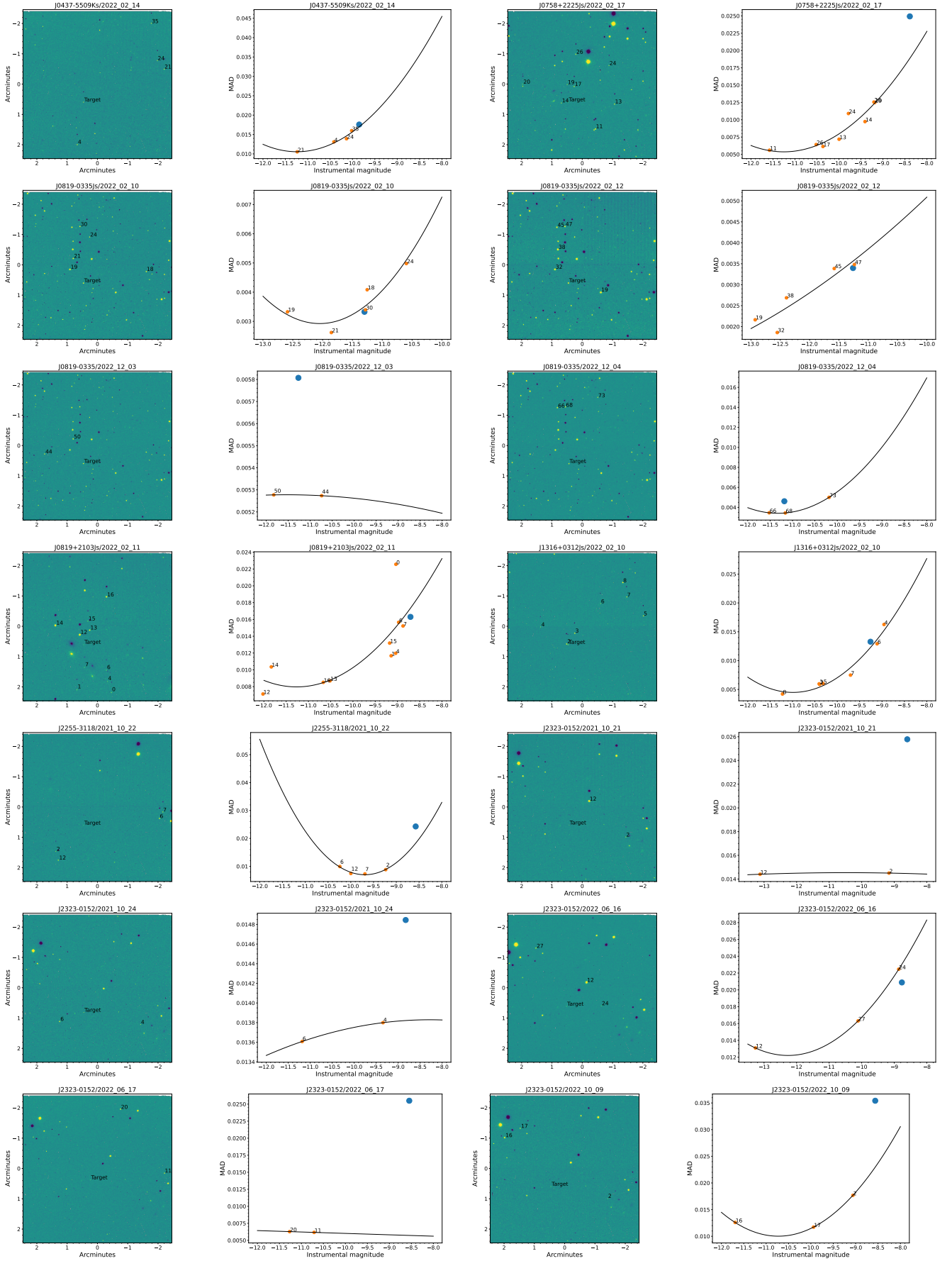


Figure A1 – continued Targets and their selected reference stars.

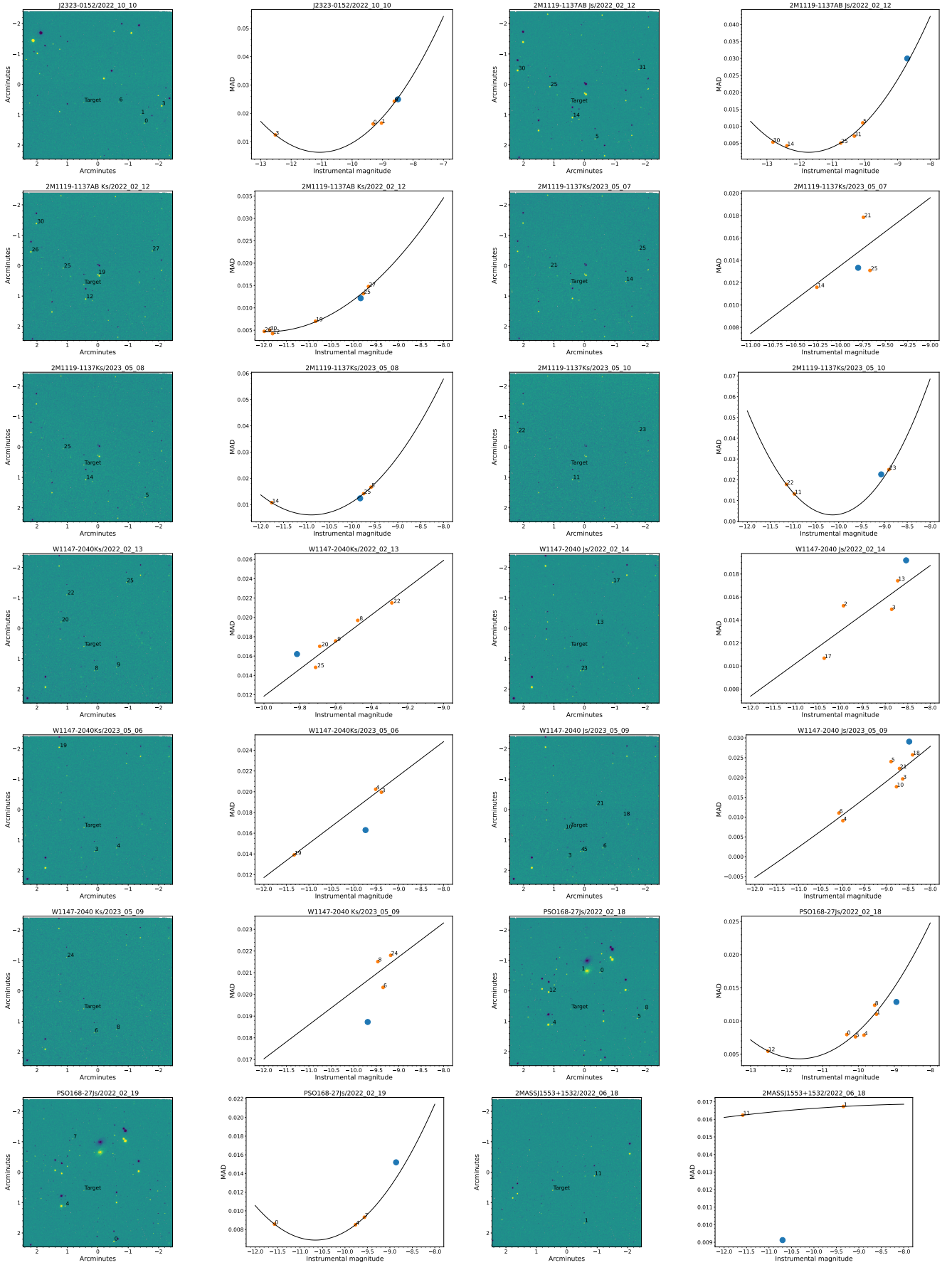


Figure A1 – *continued* Targets and their selected reference stars.

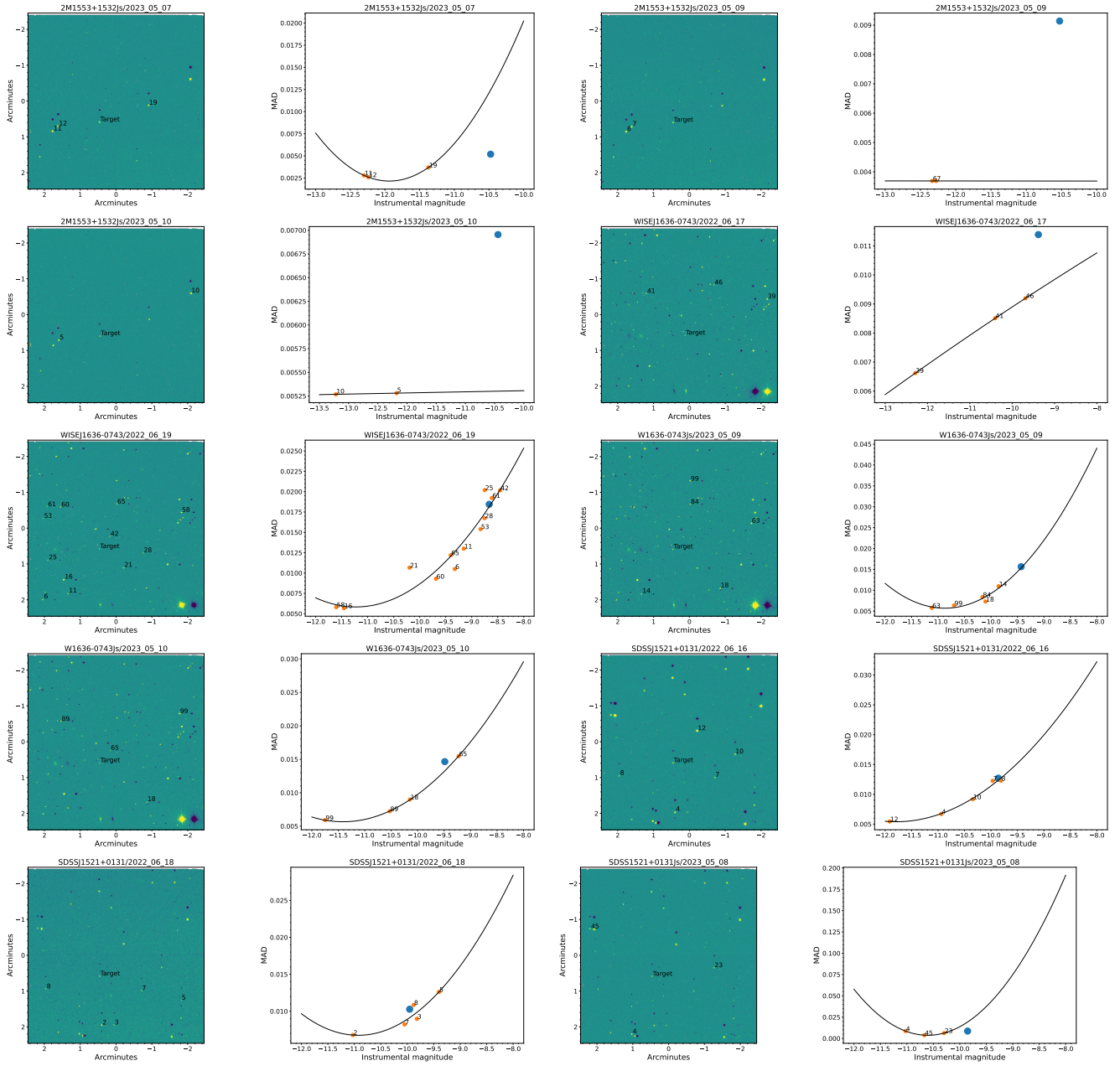


Figure A1 – continued Targets and their selected reference stars.

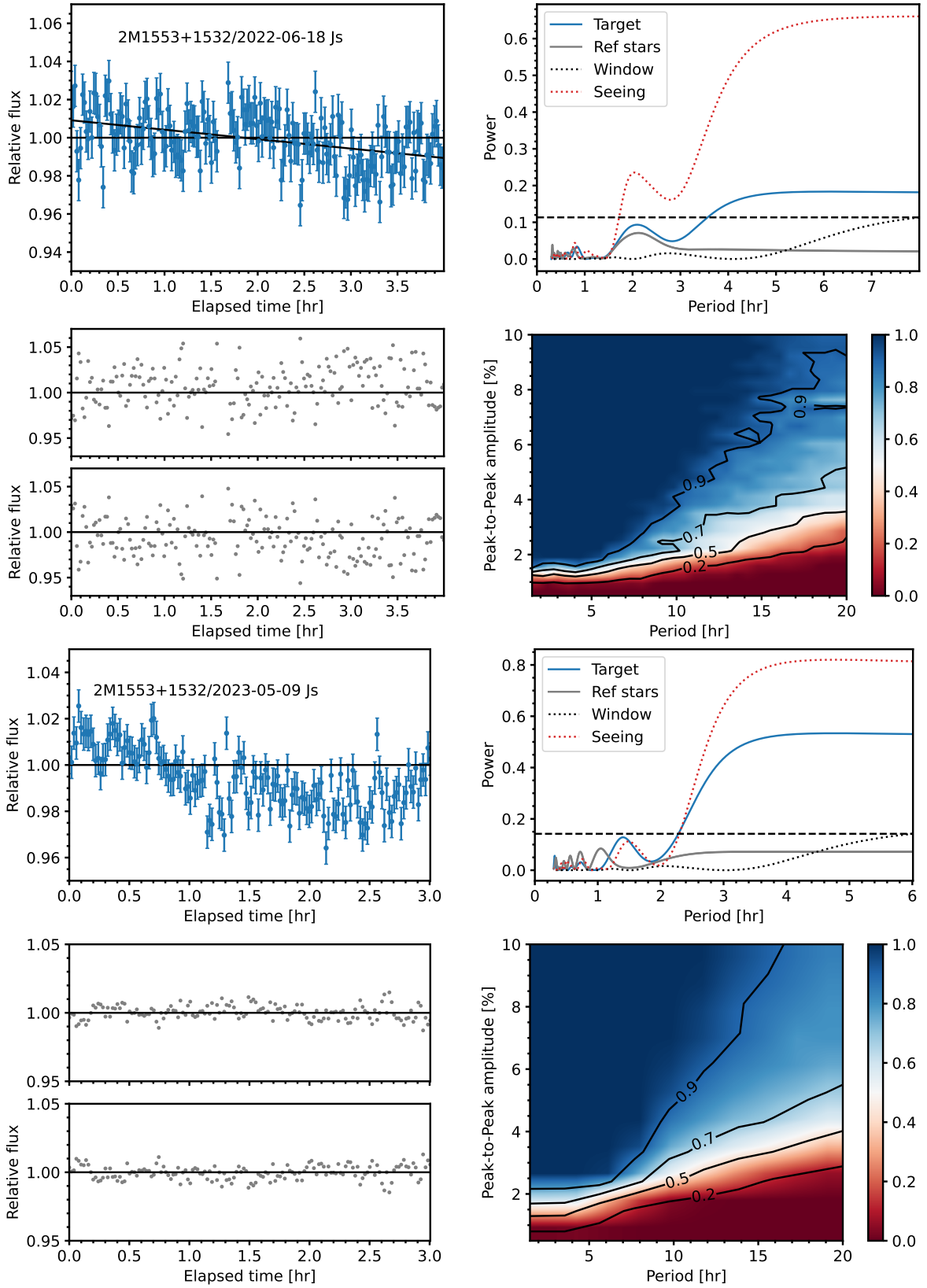


Figure B1. Potentially variable light curves, periodograms, and sensitivity plots of 2M1553+1532, including the detrended light curves and periodograms of the reference stars. While 2M1553+1532 clearly shows a variability above the 1% FAP level in the periodogram of both nights, it overlaps with the periodogram of the seeing curve, making it a suspicious variable.

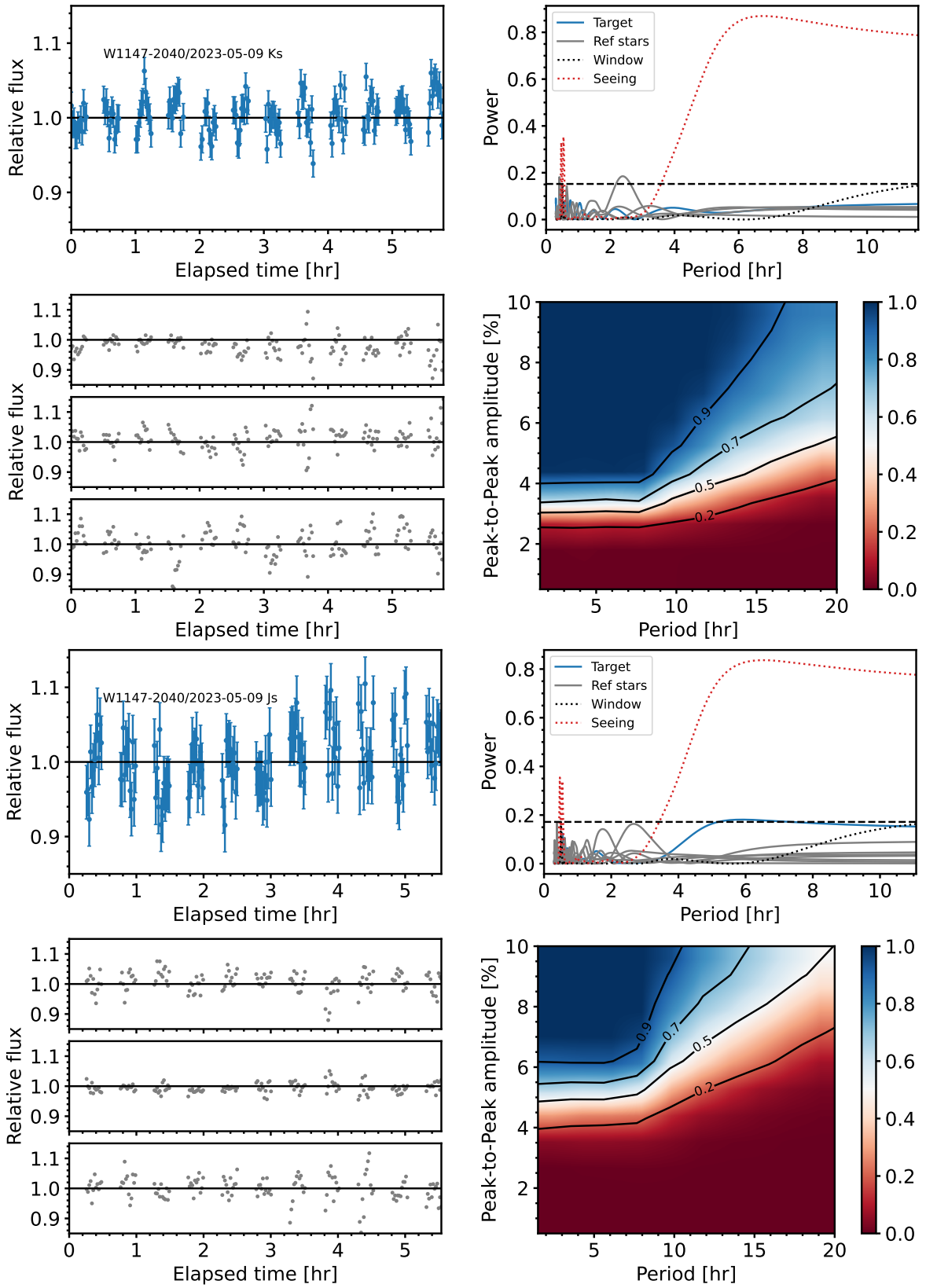


Figure B2. Interleaved K_S - and J_S -band light curves, periodograms, and sensitivity plots of W1147-2040 on 2023-05-09, including detrended light curves and periodograms of their reference stars. W1147-2040 shows potential variation in the J_S band which is probably correlated with the seeing.

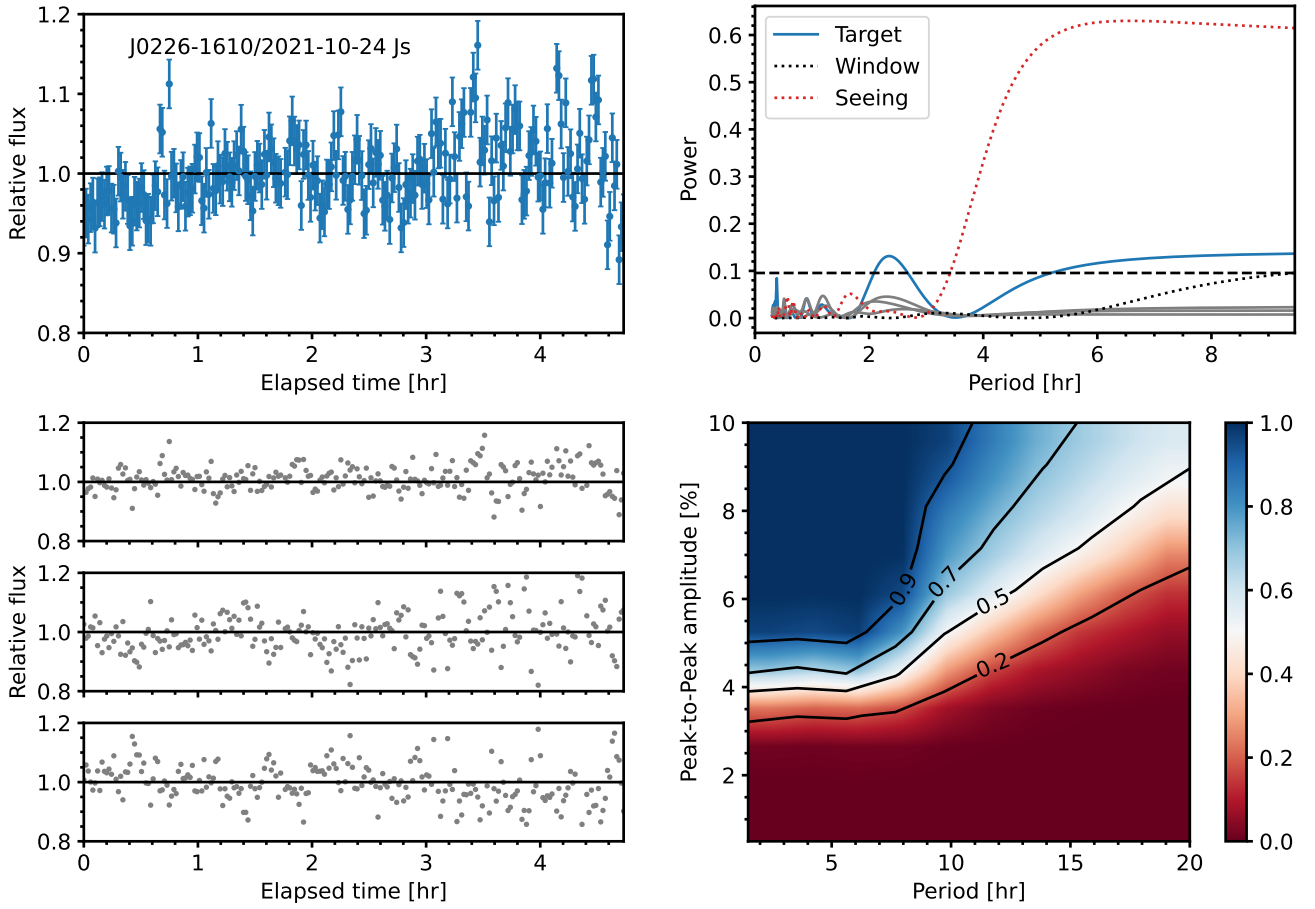


Figure B3. Potentially variable light curve, periodogram, and sensitivity plot of J0226-1610, including detrended light curves and periodograms of its reference stars. While it shows variability slightly above the 1% FAP level in the periodogram, we are cautious about the variability due to large scatter in the detrended light curves of the reference stars

APPENDIX C: NON-VARIABLE LIGHT CURVES

Non-variable light curves, periodograms and sensitivity plots.

This paper has been typeset from a $\text{\TeX}/\text{\LaTeX}$ file prepared by the author.

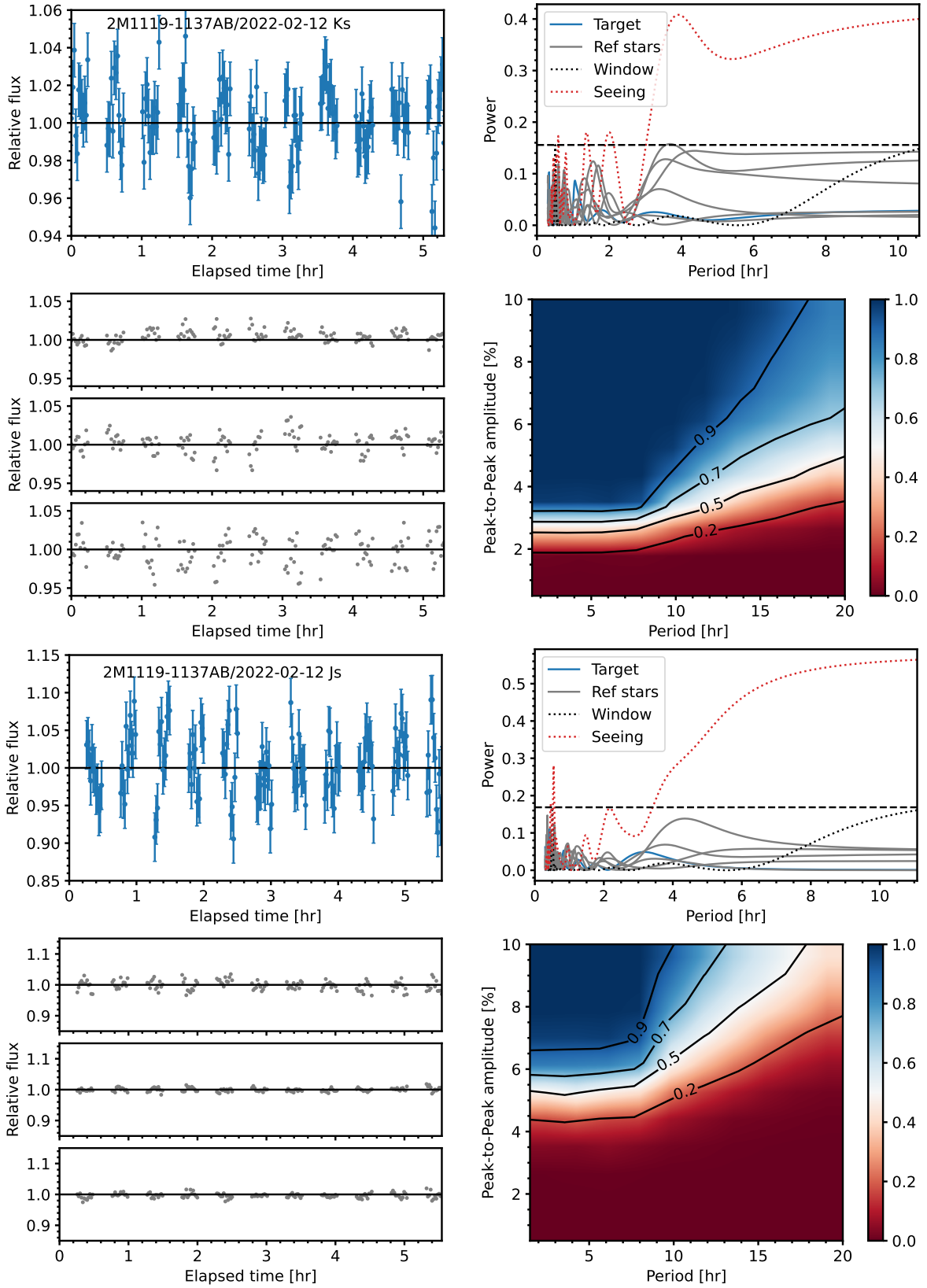


Figure C1. Interleaved J_S - and K_S -band non-variable light curves, periodograms, and sensitivity plots of a variable object 2M1119-1137AB, including detrended light curves and periodograms of its reference stars.

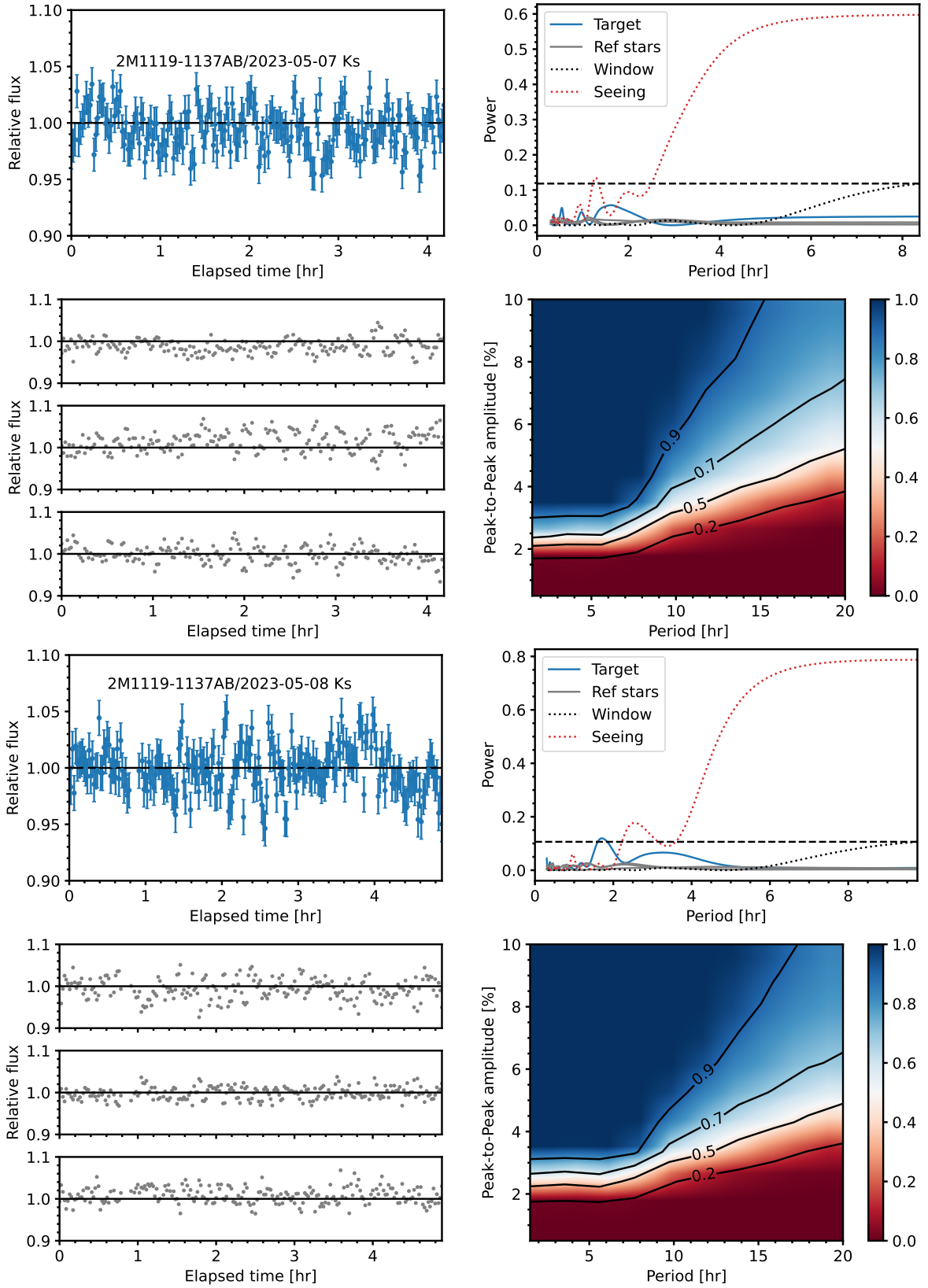


Figure C2. K_S -band non-variable light curves, periodograms, and sensitivity plots of a variable object 2M1119-1137AB, including detrended light curves and periodograms of its reference stars.

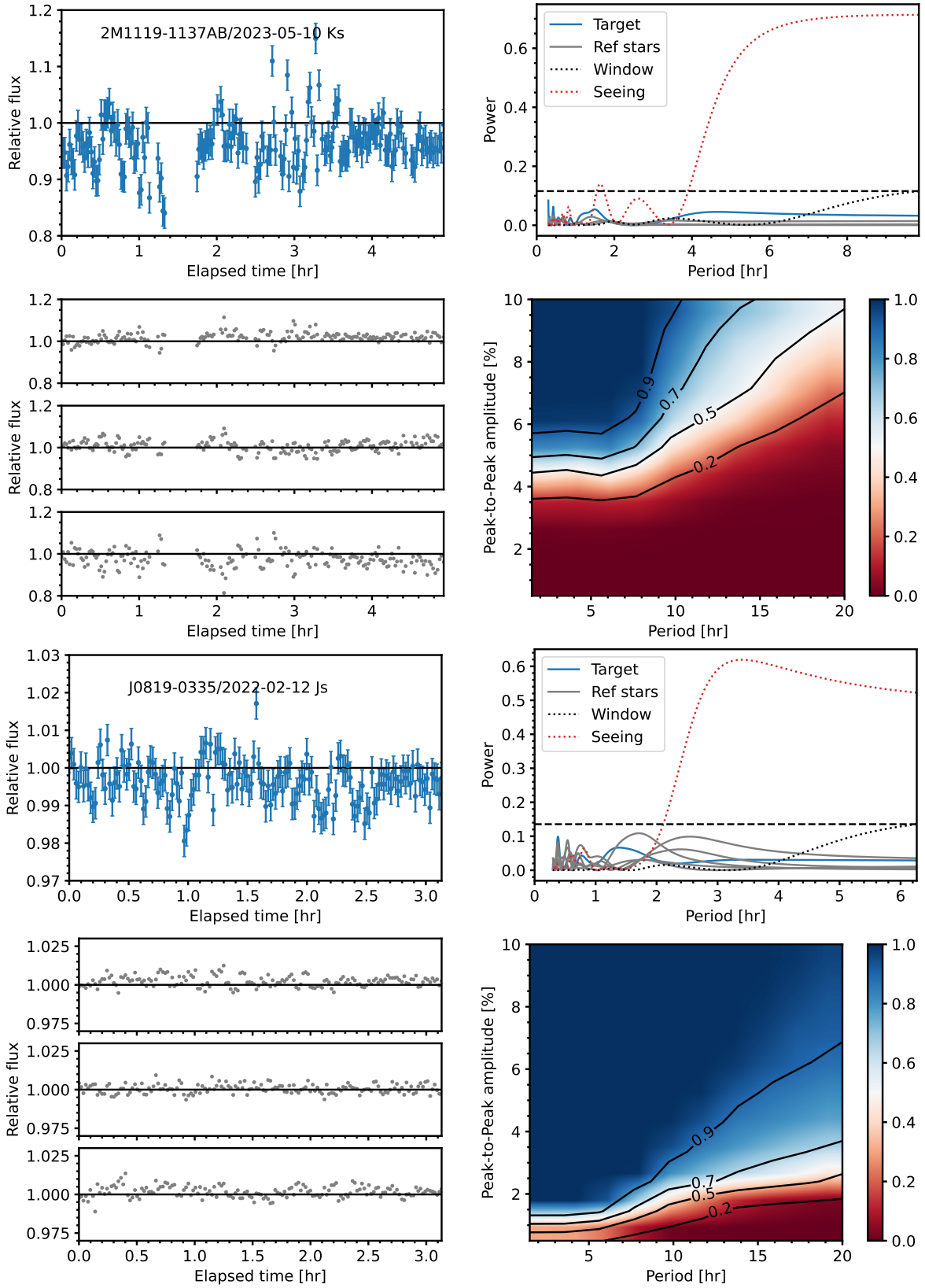


Figure C3. Non-variable light curves, periodograms, and sensitivity plots of two variable objects 2M1119-1137AB and J0819-0335, including detrended light curves and periodograms of their reference stars

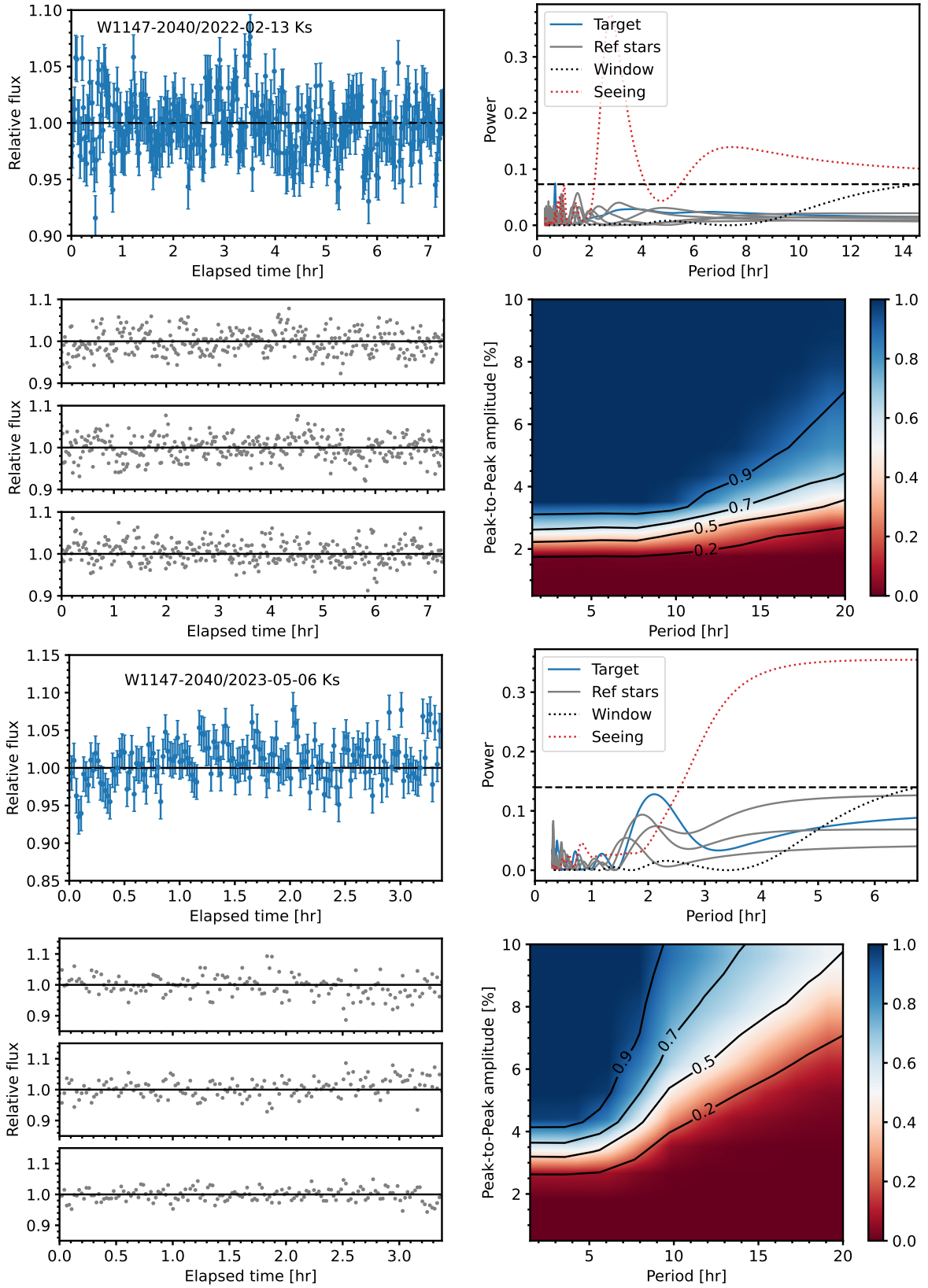


Figure C4. Non-variable light curves, periodograms, and sensitivity plots of a variable object W1147-2040, including detrended light curves and periodograms of its reference stars

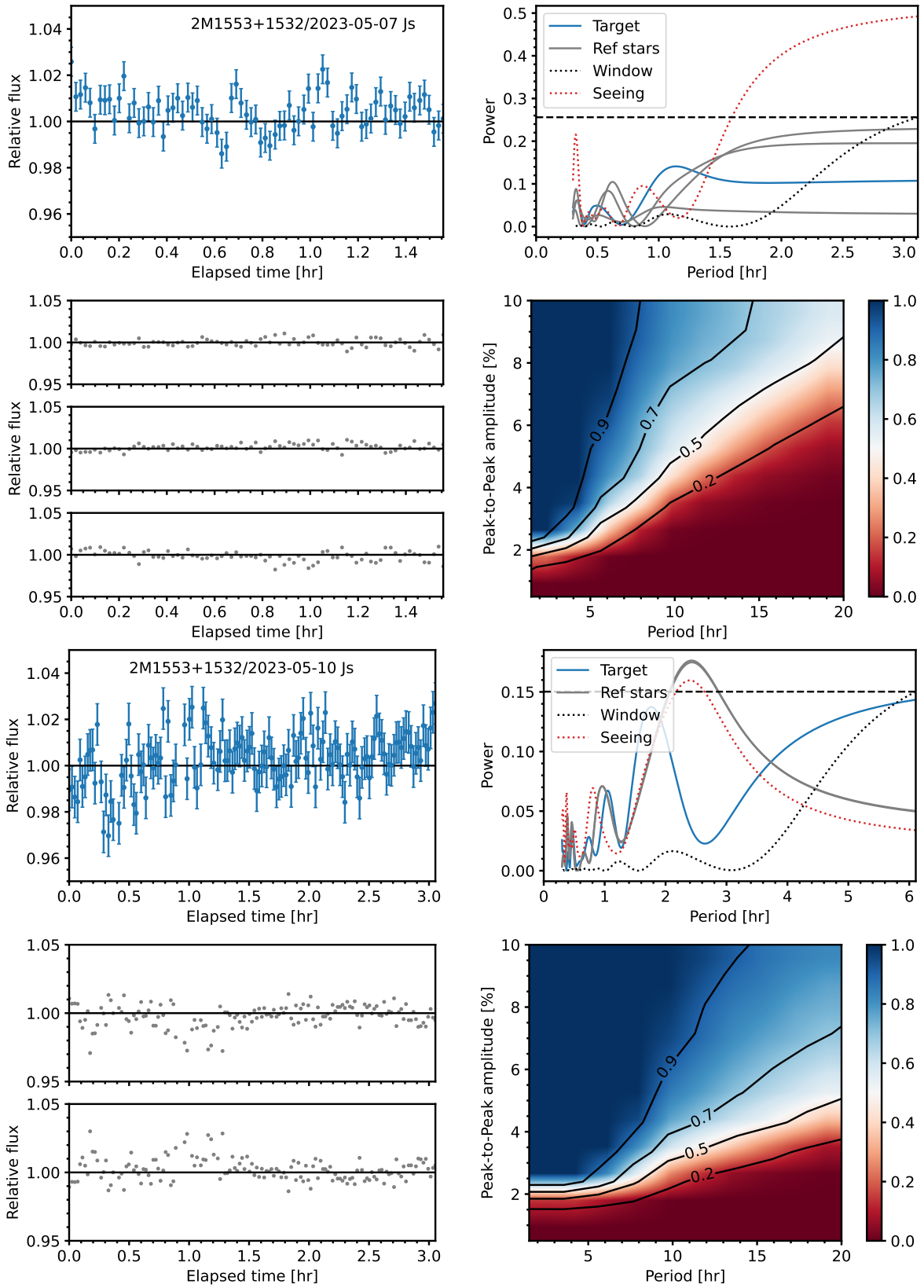


Figure C5. Non-variable light curves, periodograms, and sensitivity plots of a variable object 2M1552+1532, including detrended light curves and periodograms of its reference stars

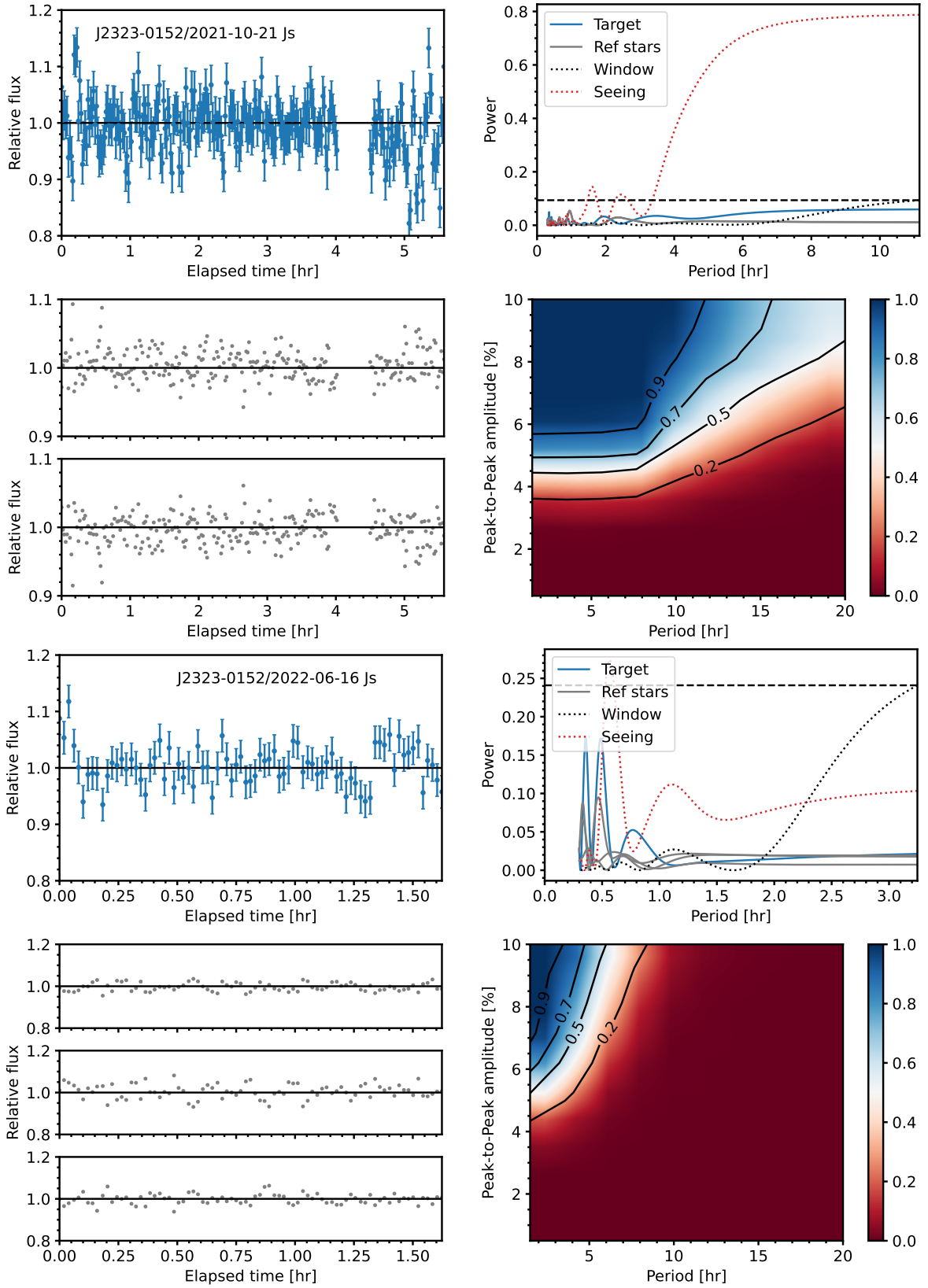


Figure C6. Non-variable light curves, periodograms, and sensitivity plots of a variable object J2323-0152, including detrended light curves and periodograms of its reference stars.

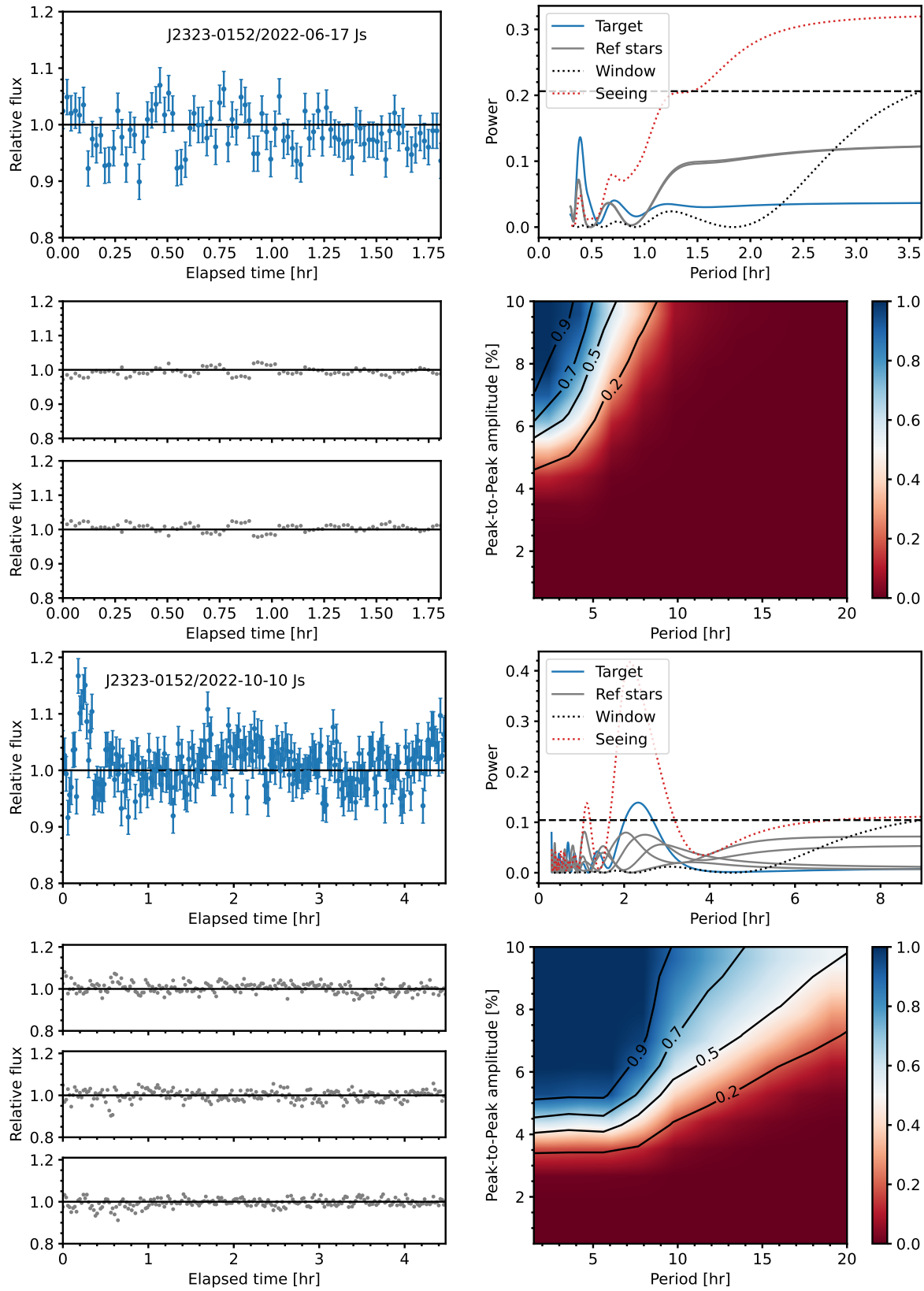


Figure C6 – *continued* Non-variable light curves, periodograms, and sensitivity plots of a variable object J2323-0152, including detrended light curves and periodograms of its reference stars.

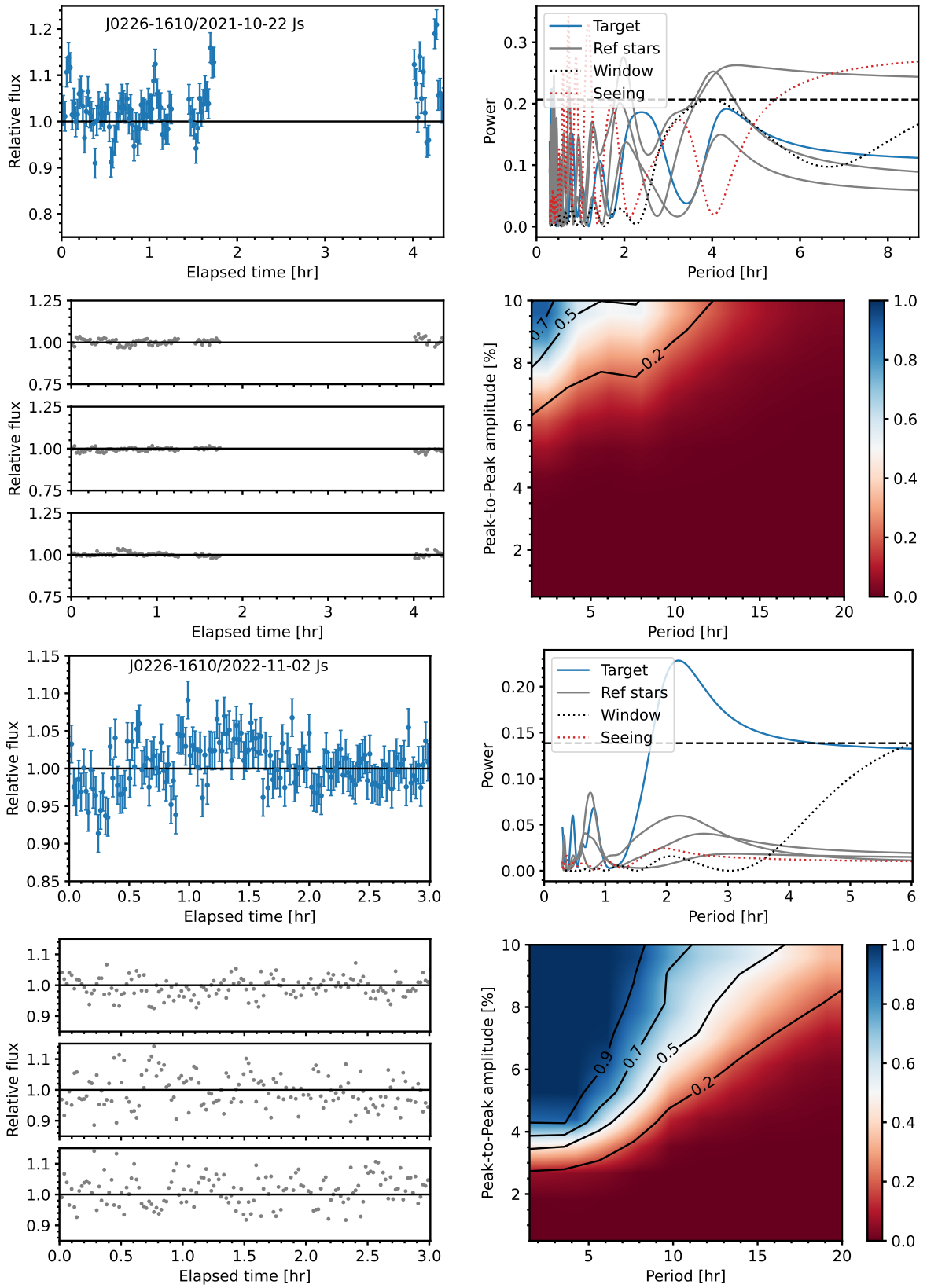


Figure C7. Non-variable light curves, periodograms, and sensitivity plots of a variable candidate J0200-1610, including detrended light curves and periodograms of its reference stars.

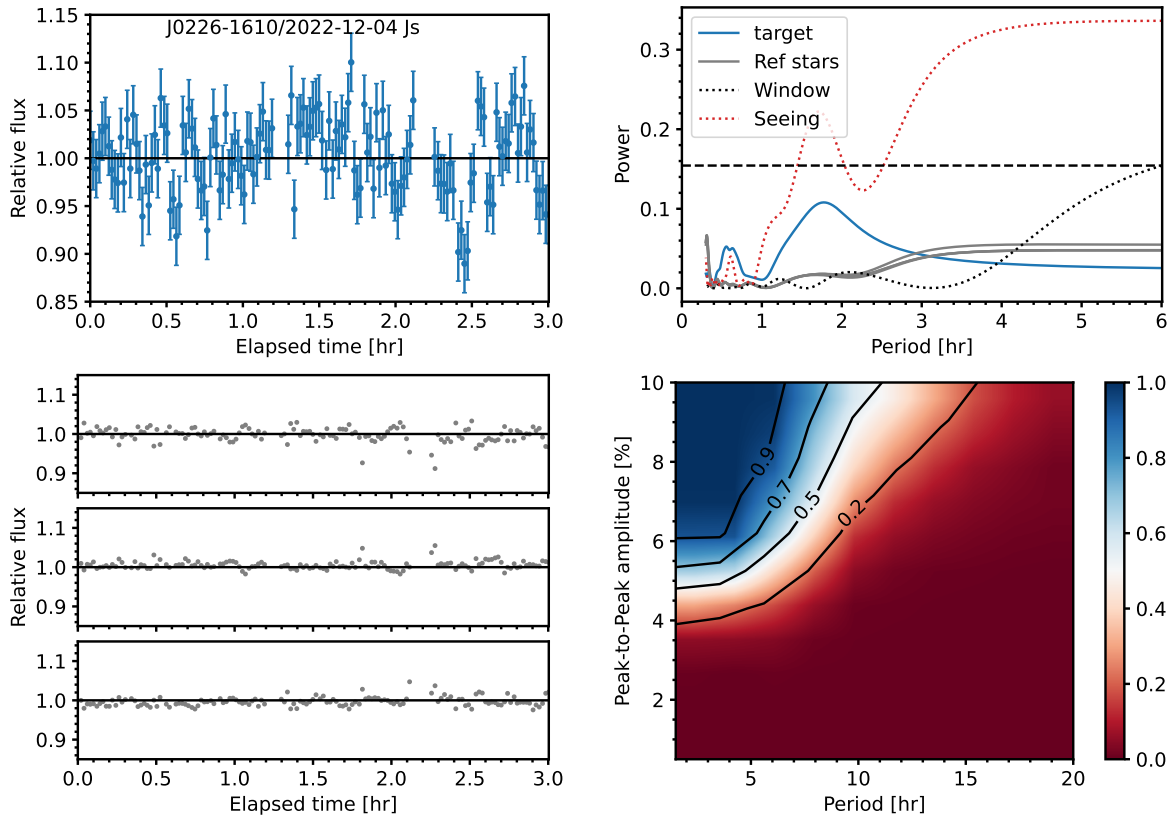


Figure C7 – *continued* Non-variable light curves, periodograms, and sensitivity plots of a potentially variable candidate J0200-1610, including detrended light curves and periodograms of its reference stars.

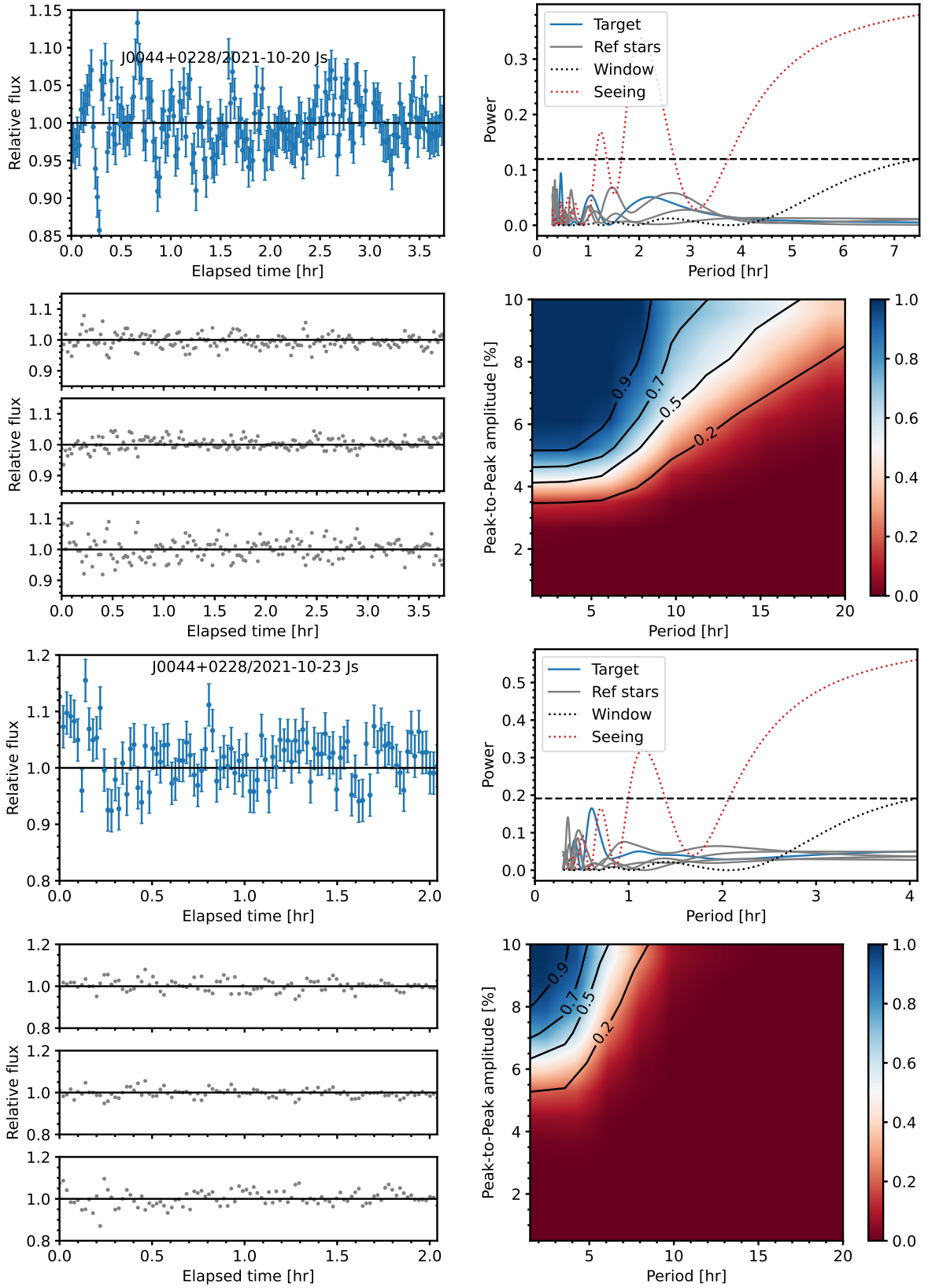


Figure C8. Light curves, periodograms, and sensitivity plots of a non-variable object J0044+0228, including detrended light curves and periodograms of its reference stars.

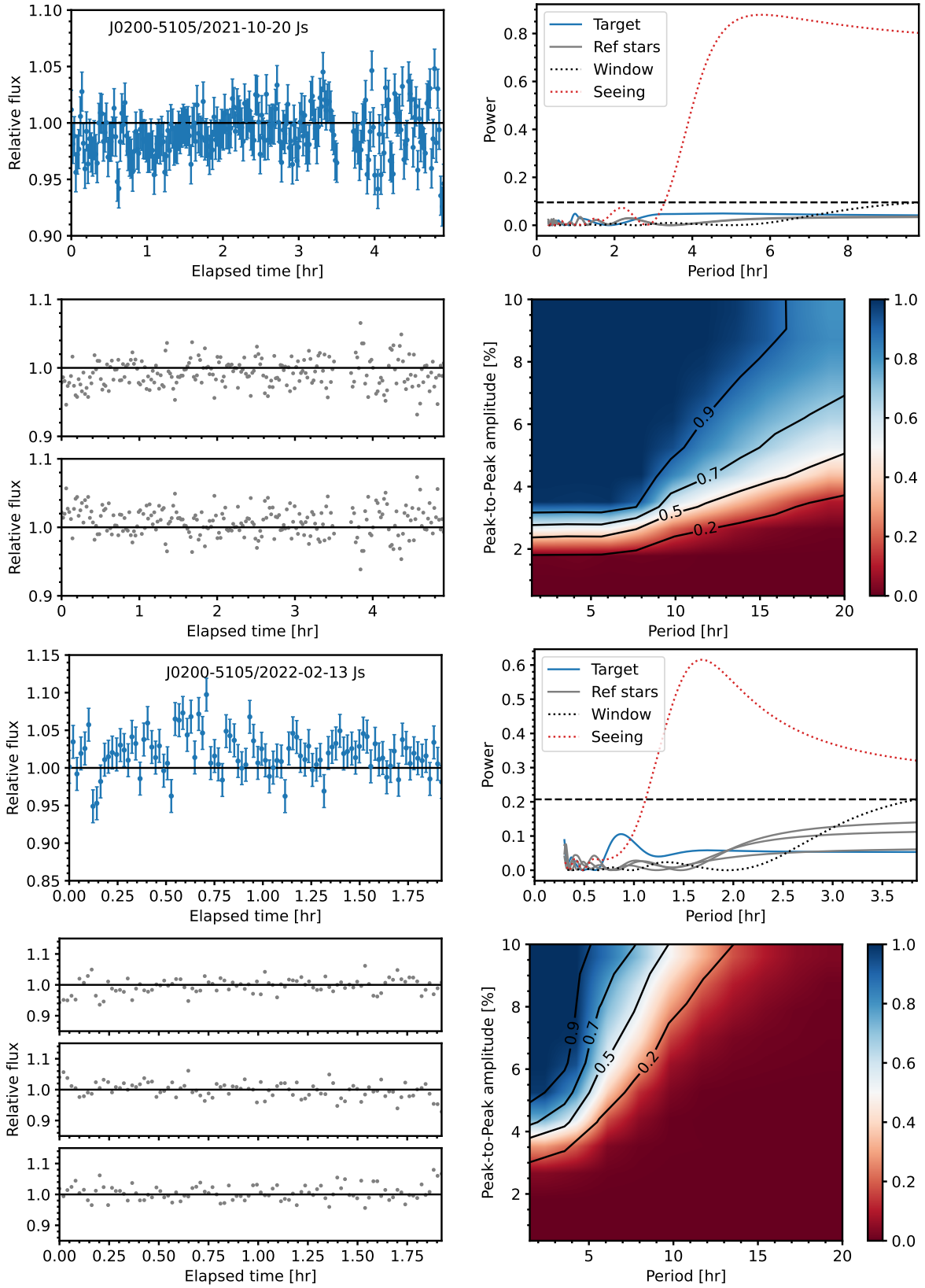


Figure C9. Light curves, periodograms, and sensitivity plots of a non-variable object J0200-5105, including detrended light curves and periodograms of its reference stars.

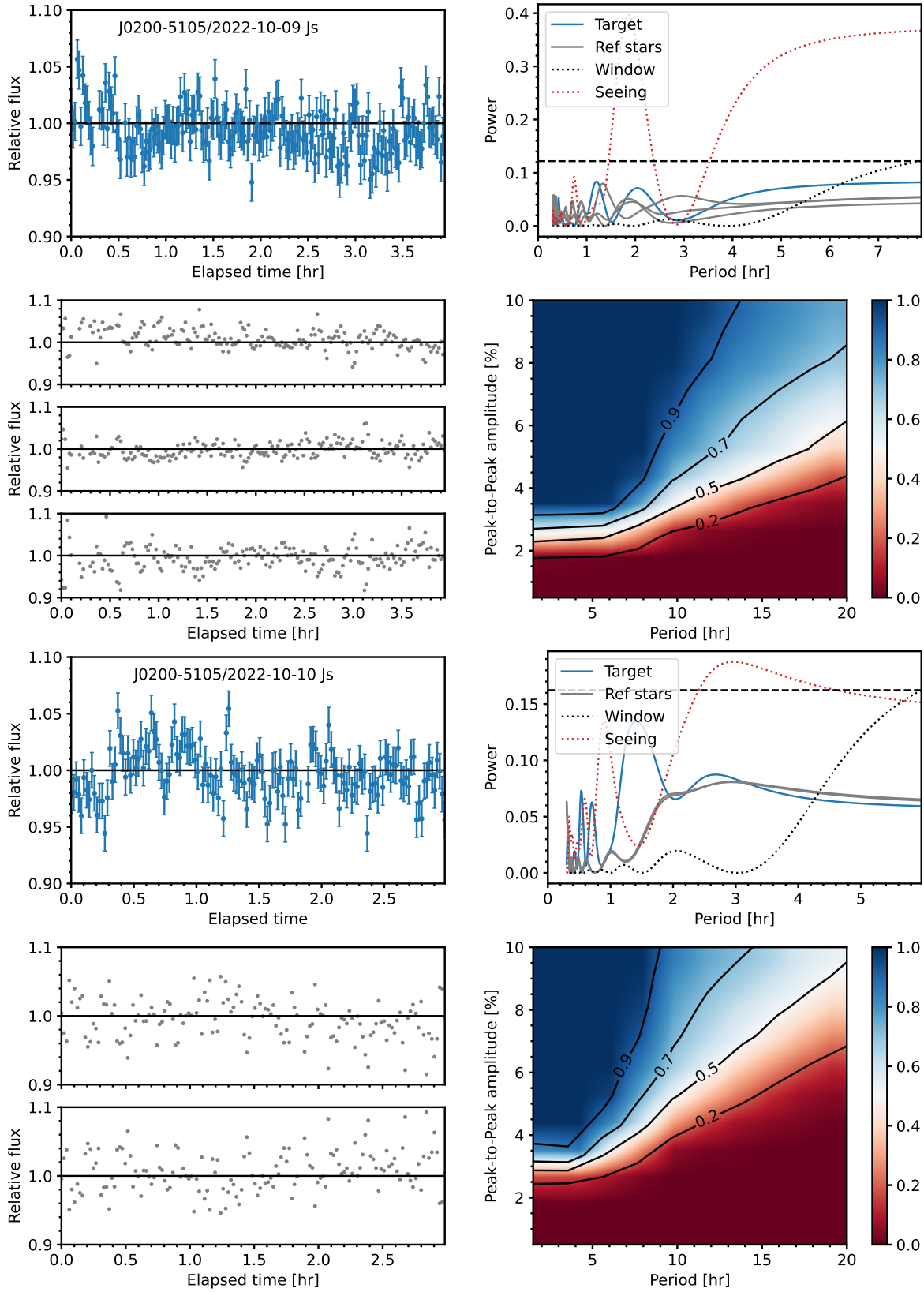


Figure C9 – *continued* Light curves, periodograms, and sensitivity plots of a non-variable object J0200-5105, including detrended light curves and periodograms of its reference stars.

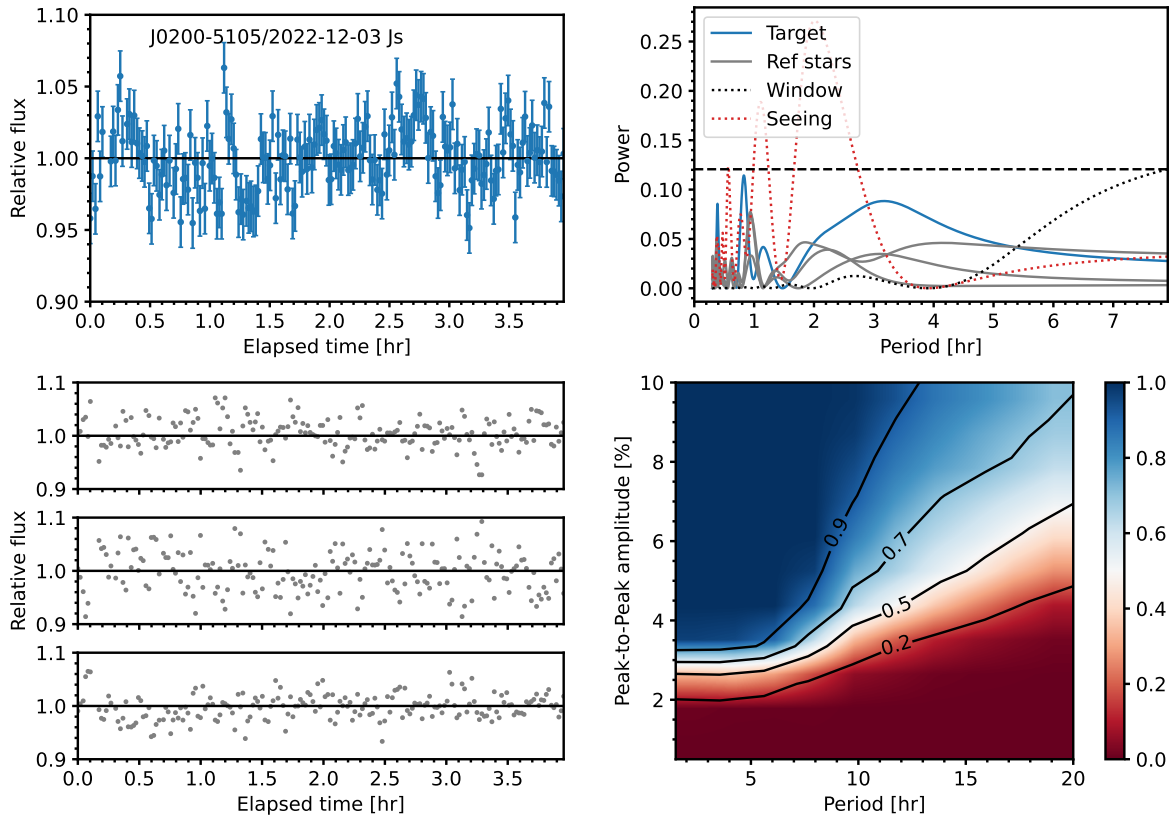


Figure C9 – *continued* Light curves, periodograms, and sensitivity plots of a non-variable object J0200-5105, including detrended light curves and periodograms of its reference stars.

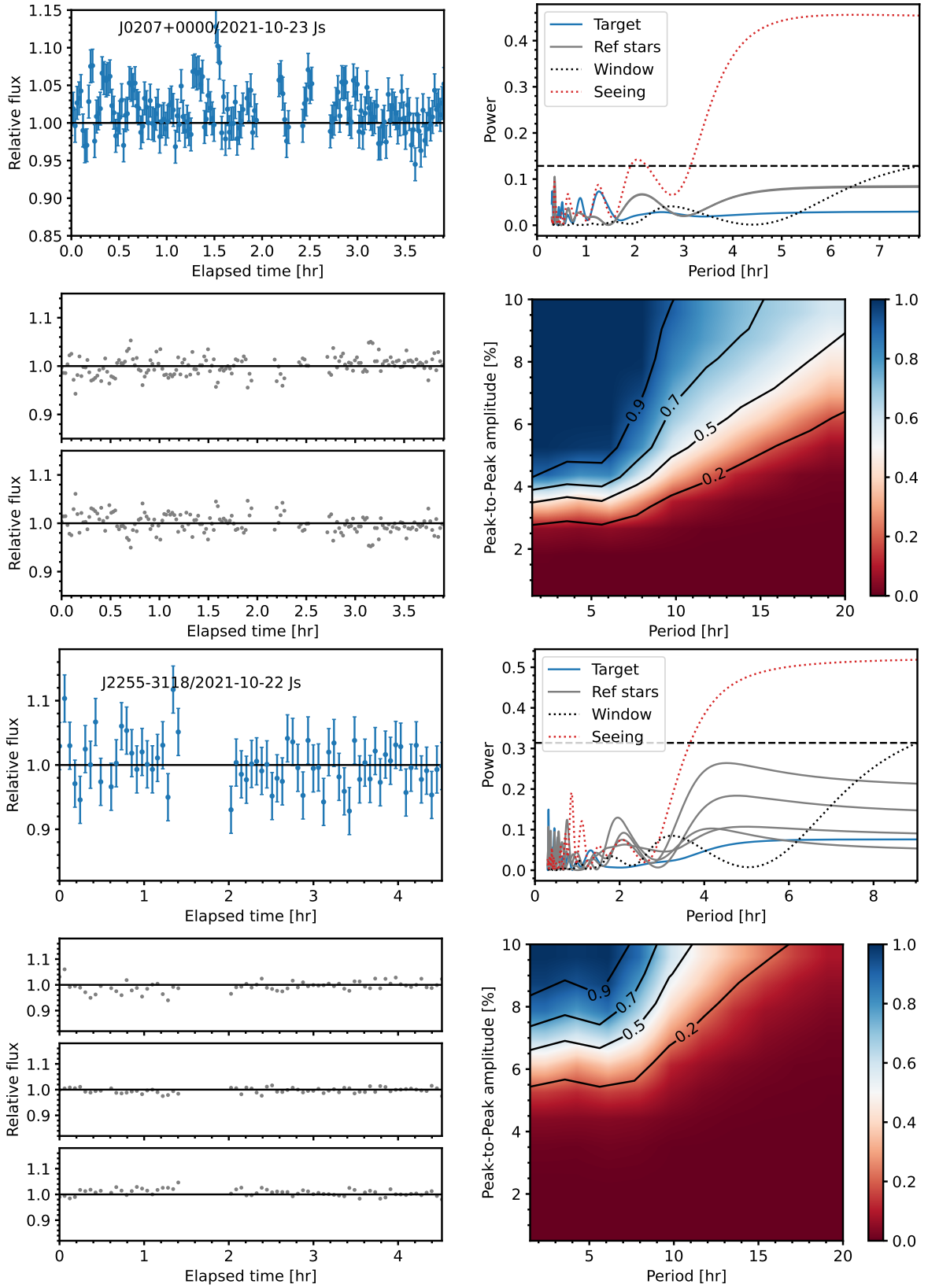


Figure C10. Light curves, periodograms, and sensitivity plots of non-variable objects J0207+0000 and J2255-3118, including detrended light curves and periodograms of their reference stars.

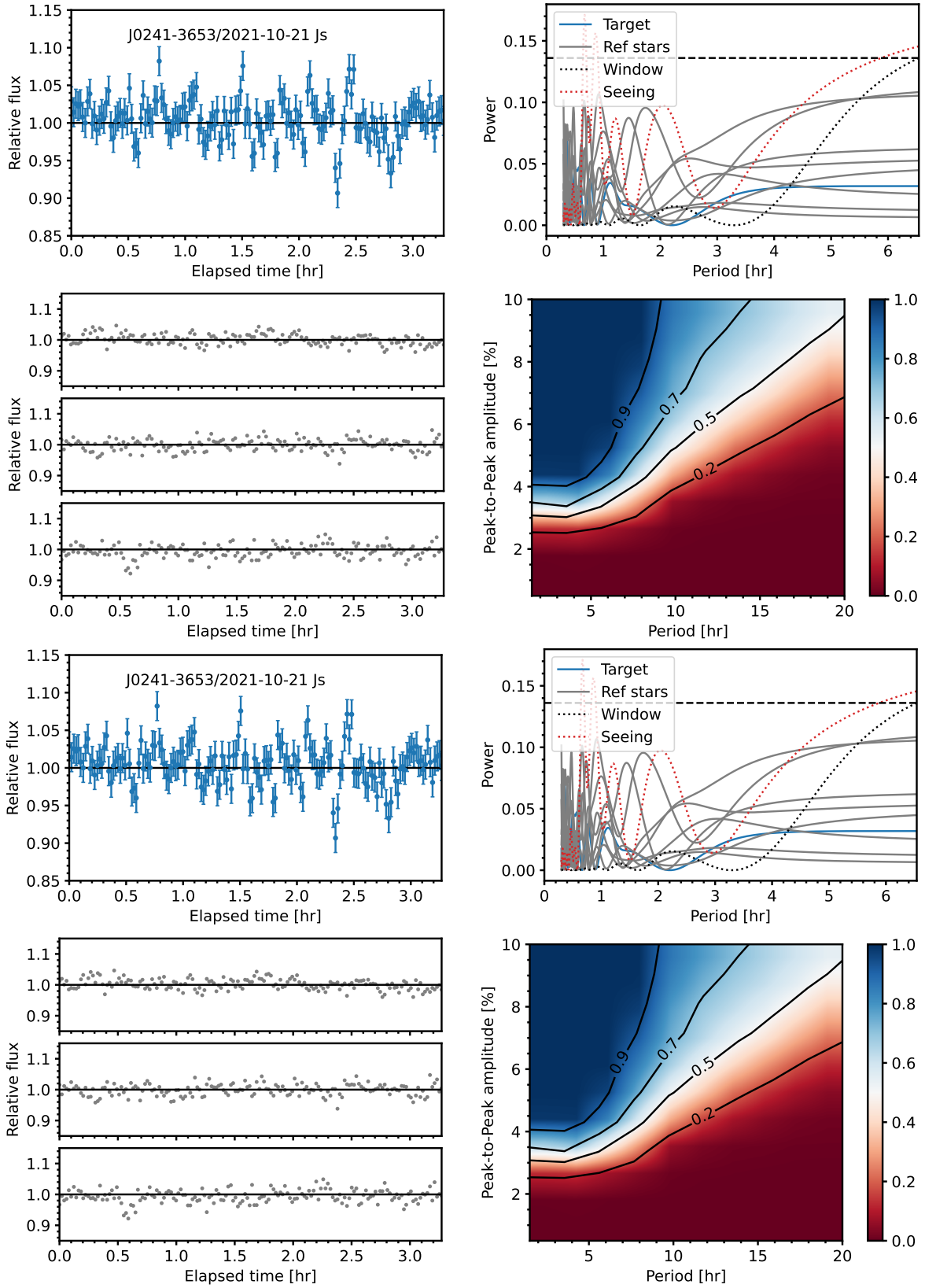


Figure C11. Light curves, periodograms, and sensitivity plots of a non-variable object J0241-3653, including detrended light curves and periodograms of its reference stars.

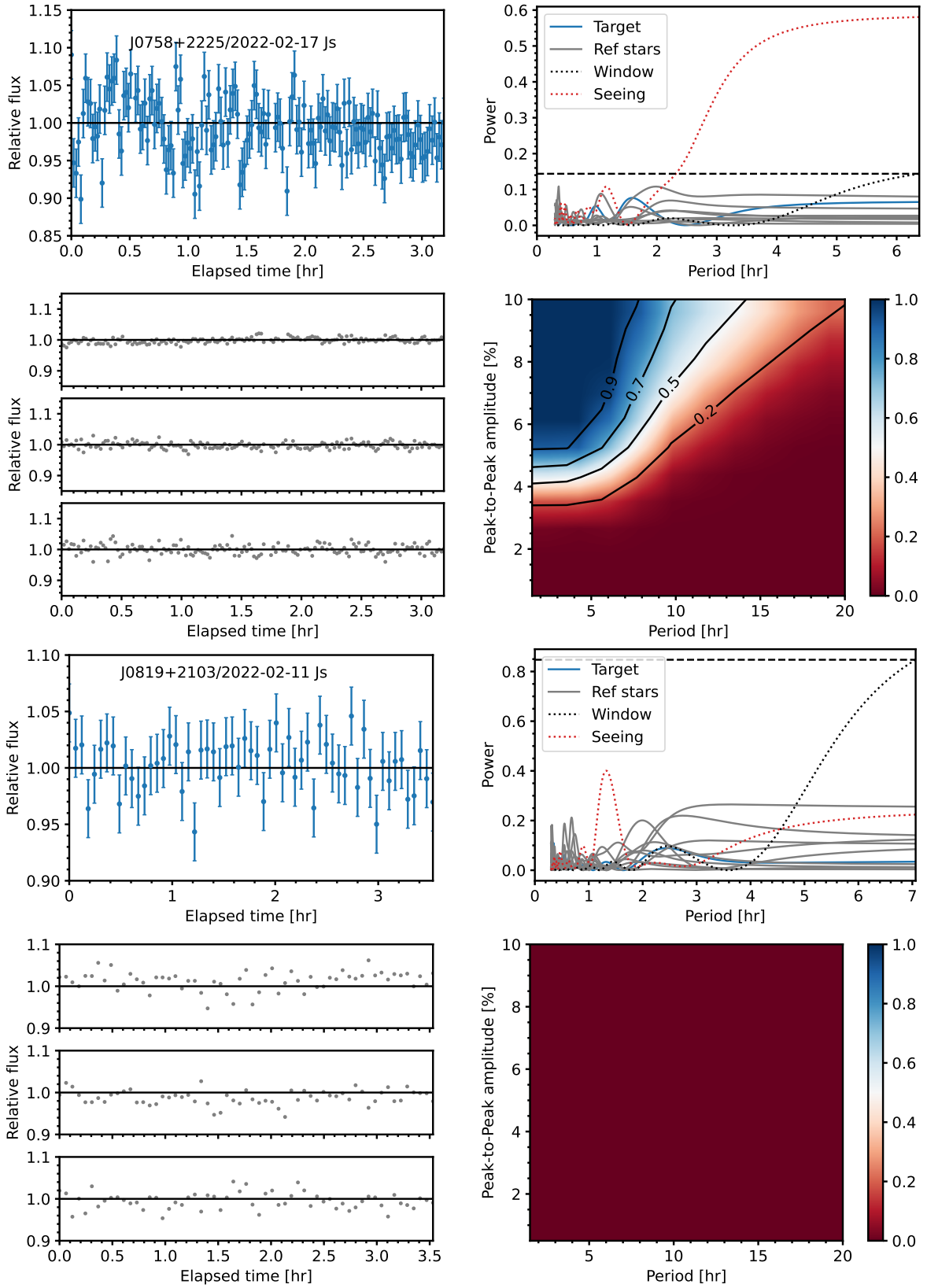


Figure C12. Light curves, periodograms, and sensitivity plots of non-variable objects J0758+2225 and J0819+2103, including detrended light curves and periodograms of their reference stars.

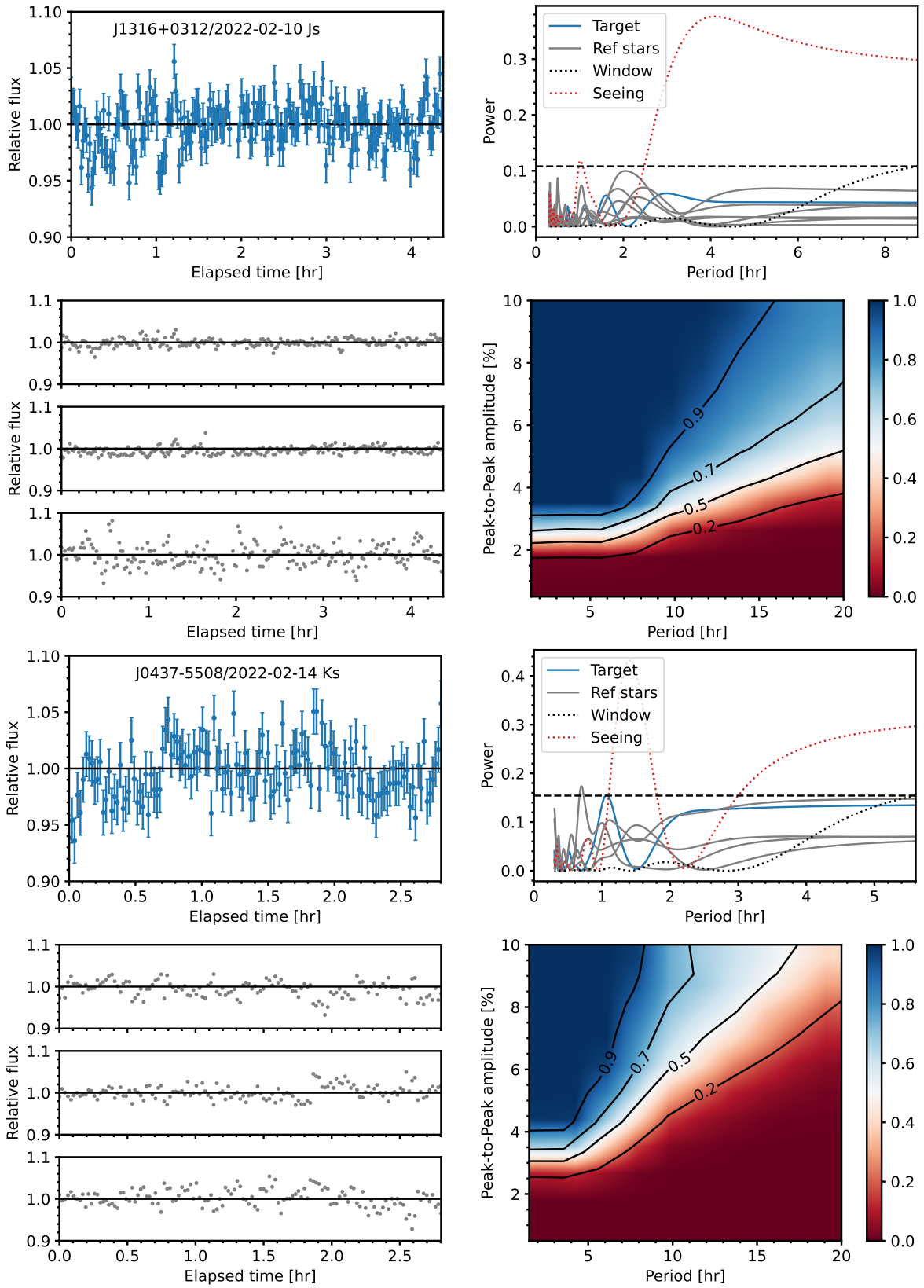


Figure C13. Light curves, periodograms, and sensitivity plots of non-variable objects J1316+0312 and J0437-5508, including detrended light curves and periodograms of their reference stars.

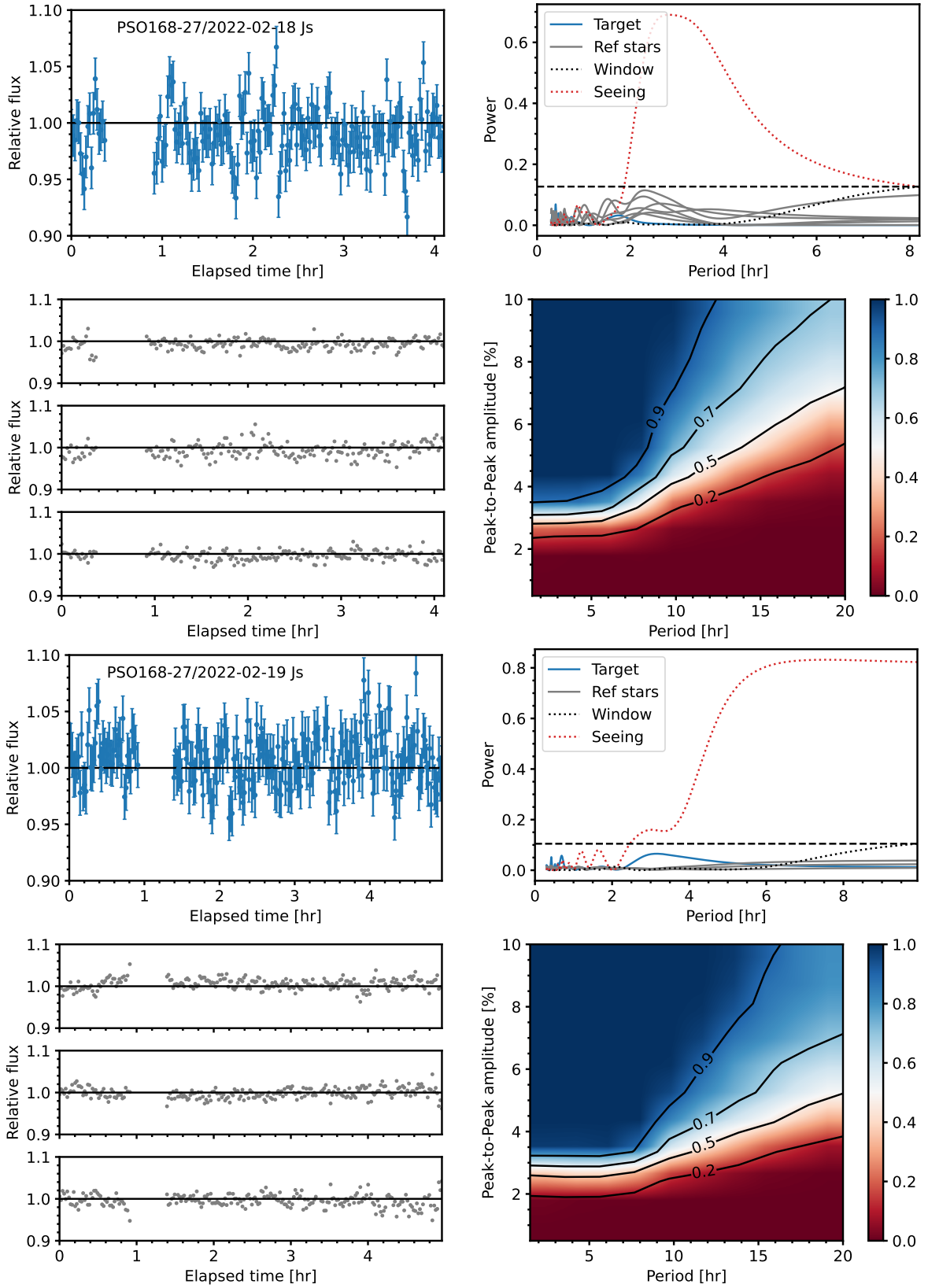


Figure C14. Light curves, periodograms, and sensitivity plots of a non-variable object PSO168-27, including detrended light curves and periodograms of its reference stars.

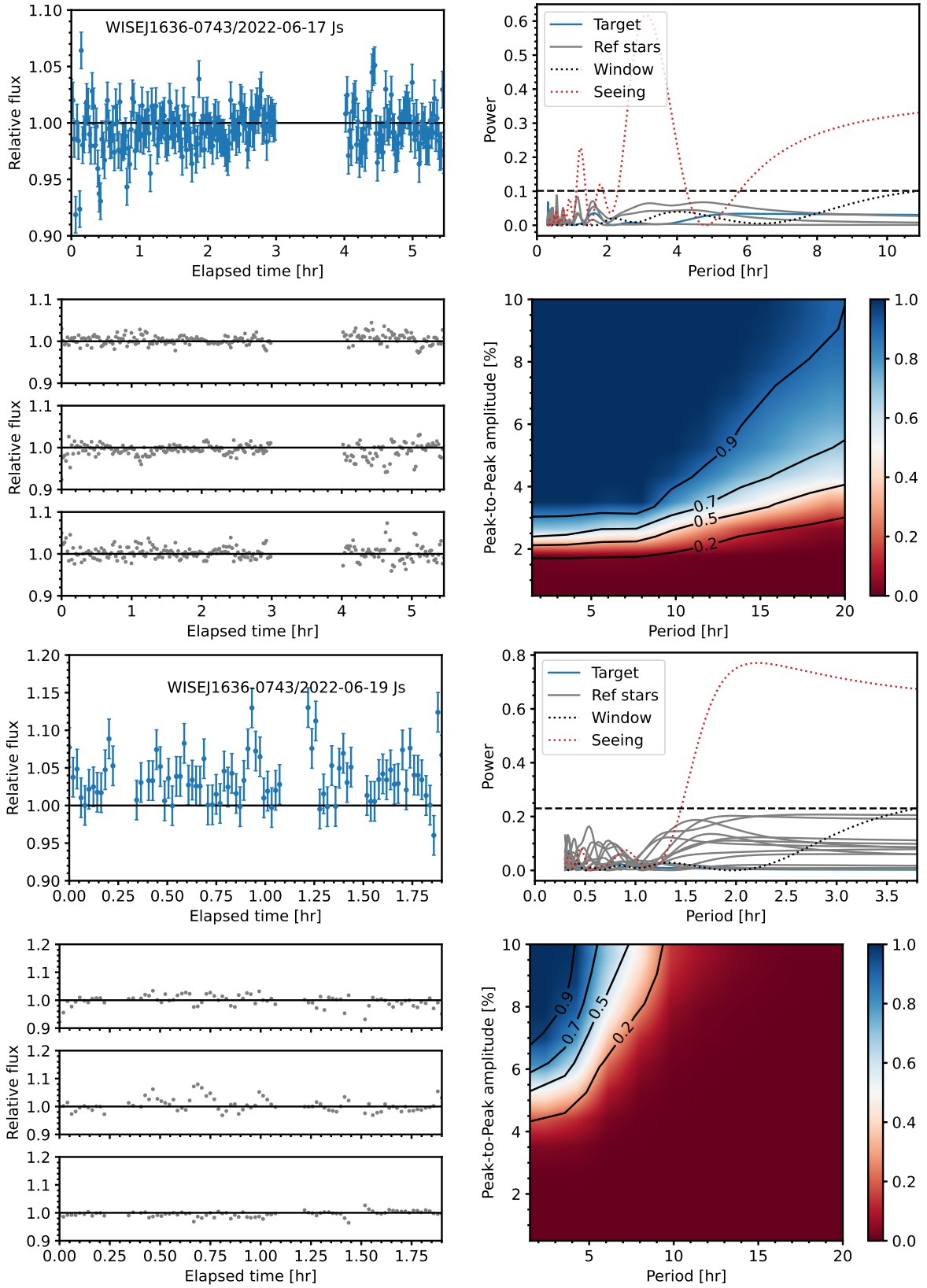


Figure C15. Light curves, periodograms, and sensitivity plots of a non-variable object WISEJ1636-0743, including detrended light curves and periodograms of its reference stars.

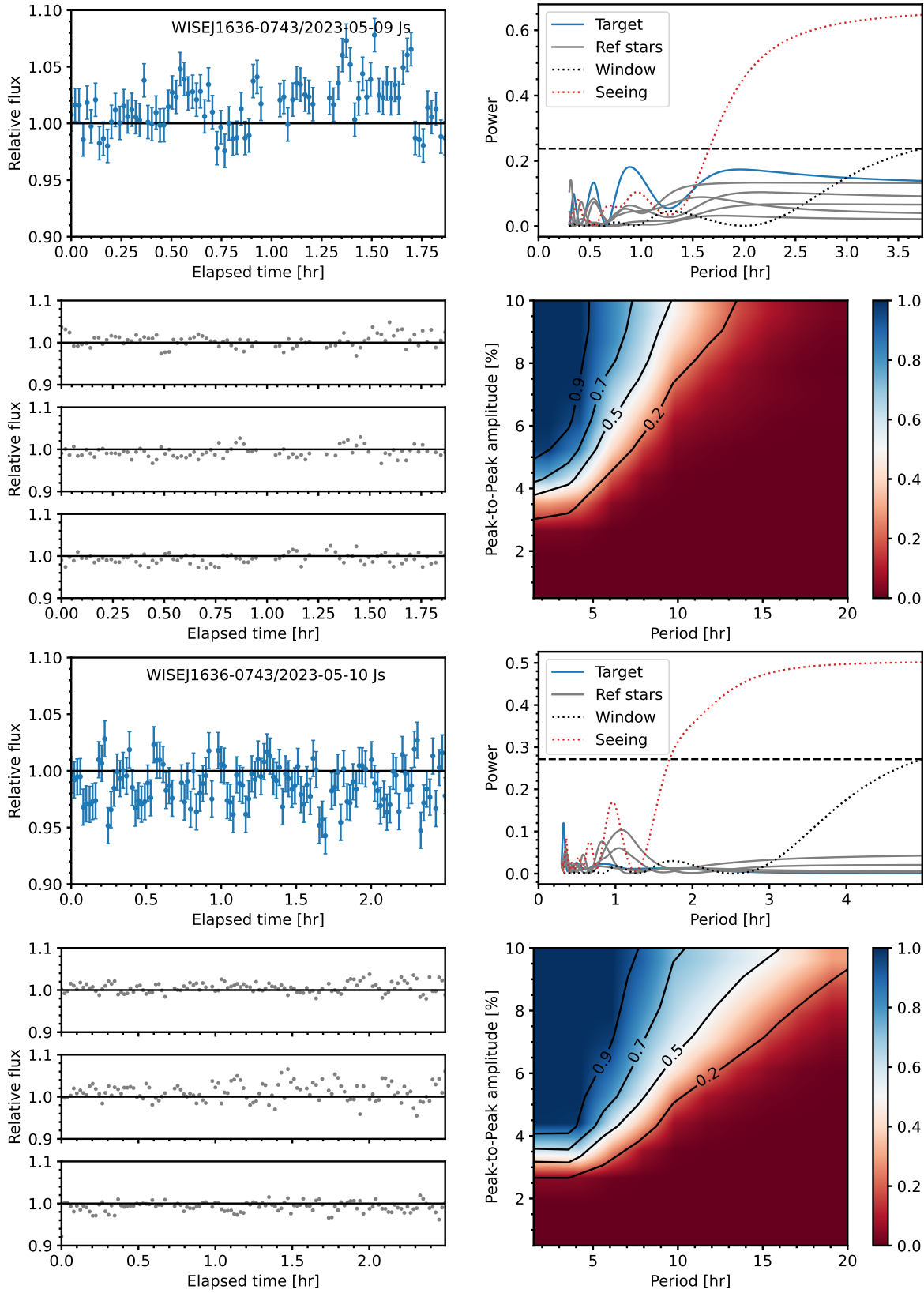


Figure C15 – *continued* Light curves, periodograms, and sensitivity plots of a non-variable object WISEJ1636-0743, including detrended light curves and periodograms of its reference stars.

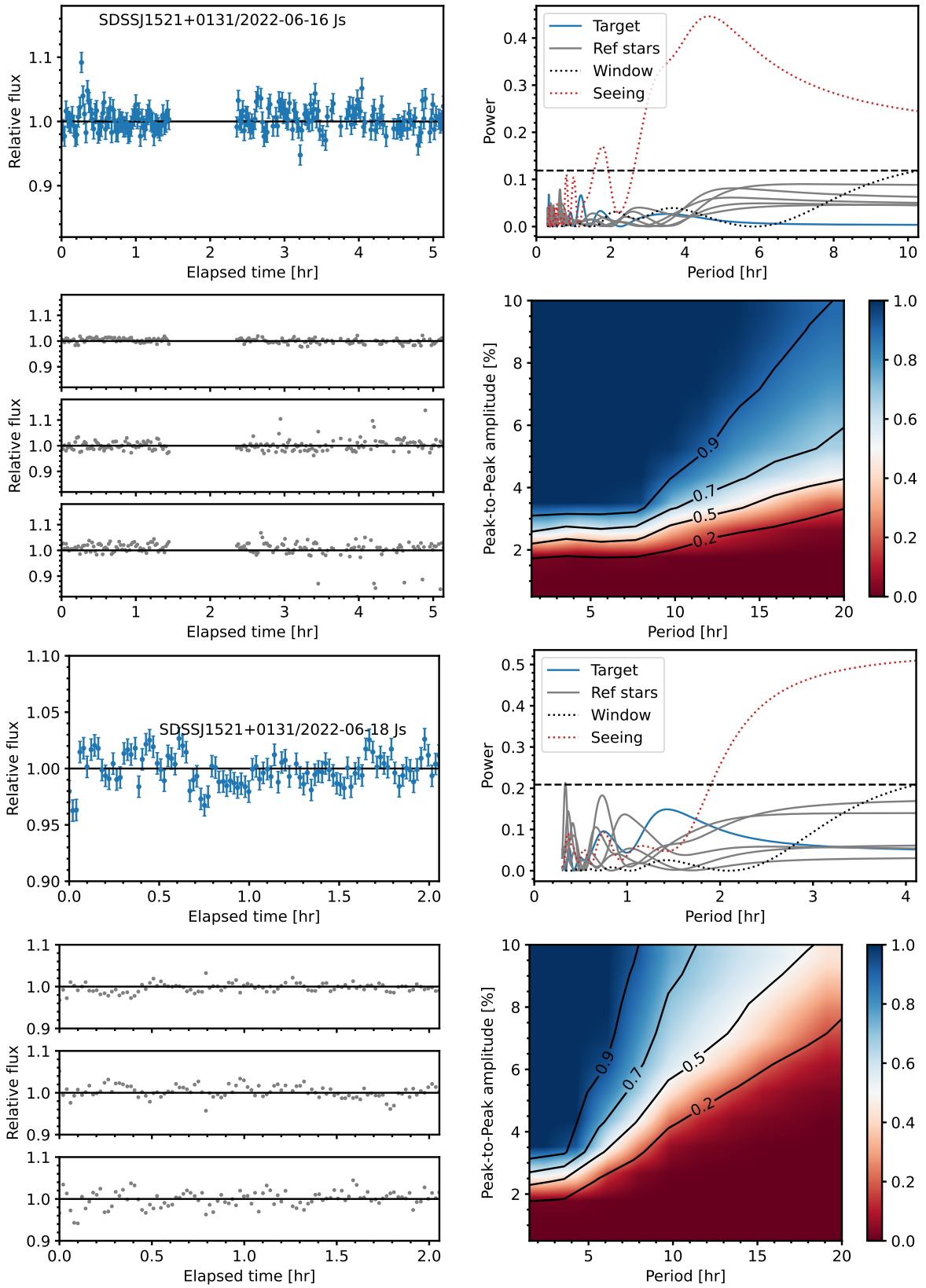


Figure C16. Light curves, periodograms, and sensitivity plots of a non-variable object SDSS1521+0131, including detrended light curves and periodograms of its reference stars.

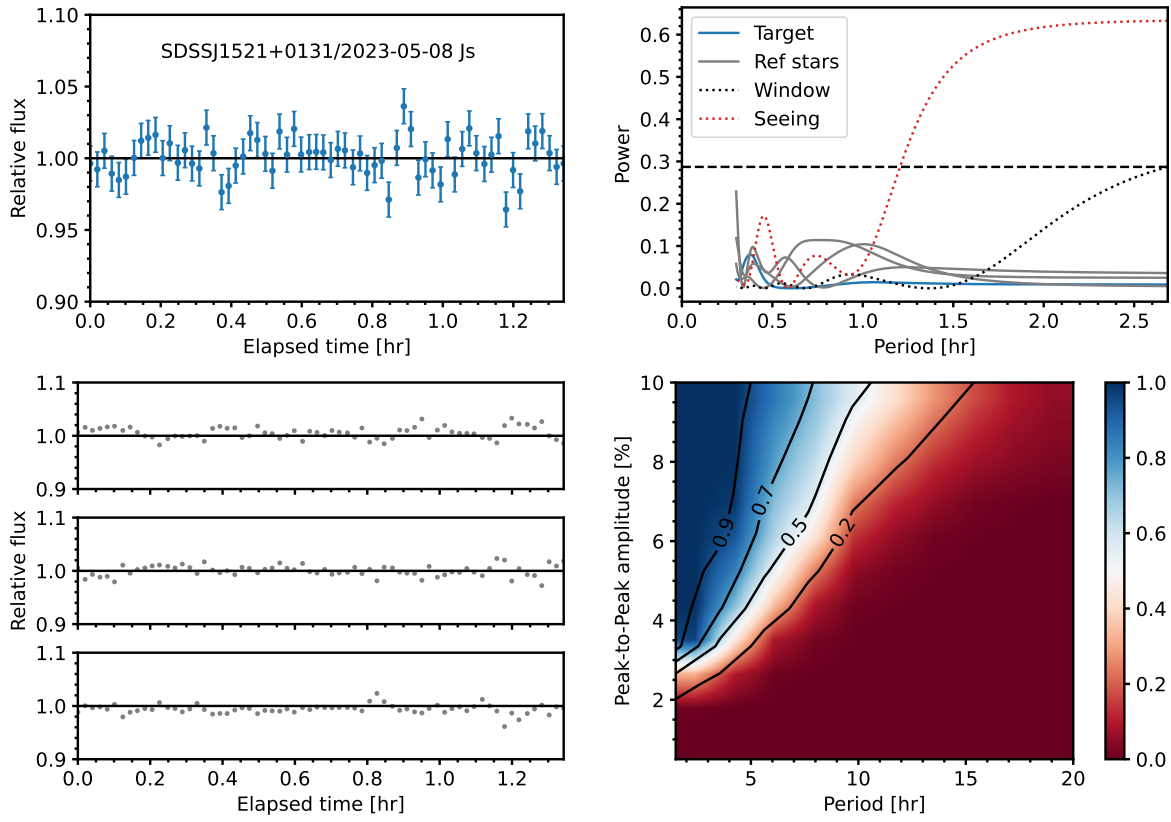


Figure C16 – *continued* Light curves, periodograms, and sensitivity plots of a non-variable object SDSS1521+0131, including detrended light curves and periodograms of its reference stars.